NTNU

Norwegian University of
Science and Technology

Comparing the Performance of Different Silicon Powders for Use in Lithium-Ion Batteries

Harald Norrud Pollen

Materials Science and Engineering (MTMT)
Submission date: June 2018
Supervisor: Ann Mari Svensson, IMA
Co-supervisor: Karina Asheim, IMA

Norwegian University of Science and Technology
Department of Materials Science and Engineering

Preface

This thesis is written as part of the course "TMT4905 - Materials Technology, Master's Thesis", and is the final course of a five year materials science and engineering Master's degree program (MTMT) at the Norwegian University of Science and Technology (NTNU). The work described in this thesis has taken place between January and June of 2018. The experimental work presented in this thesis has been conducted by the author.

This thesis is to some extent based on a project the author worked on between August and December of 2017 as part of the course "TMT4500 - Materials Technology, Specialization Project" [1]. This project studied silicon anodes for lithium-ion batteries as well, but a different aspect was studied. Nevertheless, both the project and this thesis describe similar aspects of silicon anodes for lithium-ion batteries in the theory chapter. Parts of the experimental work were similar for both the project and the thesis.

This thesis is done with the research project "Silicon anodes for Li-ion batteries, optimized binder, electrolyte and cathode" (SiBEC).

This thesis is written so that graduate students within materials science and engineering background can follow the work. Readers should have knowledge of electrochemistry.

Trondheim, 2018

Harald Norrud Pollen

Acknowledgments

I would like to express gratitude to my supervisor Professor Ann Mari Svensson and co-supervisor PhD Candidate Karina Asheim for their regular guidance, discussions and feedback. This made the work a great learning experience! PhD Candidate Karina Asheim also deserves a thanks for showing me how to prepare electrodes and teaching me how to use electrochemical characterization equipment. I would also like to thank PhD Candidate Henning Kaland, Researcher Andreas Nicolai Norberg, PhD Candidate Daniel Tevik Rogstad, Postdoctoral Fellow Nils Wagner and PhD Candidate Elise Ramleth Østli who have helped me figure out practical issues I have encountered during the experimental work. I would like to thank Senior Engineer Magnus Bentzen Følstad, Staff Engineer Pei Na Kui, Staff Engineer Mikko Erik Vedeler Saraste, PhD Candidate Anuvansh Sharma and Senior Engineer Kristin Høydalsvik Wells for giving me training in the use of equipment and answering questions related to practical laboratory work. I would also wish to thank Senior Research Scientist Halvor Dalaker at SINTEF for giving me advice on how to make silicon anodes with nanosized silicon powder.

Summary

The topic of this thesis is silicon anodes for lithium-ion batteries. The aim of this thesis is to compare three different types of silicon powders for use in lithium-ion batteries - a micron-sized powder (Silgrain® e-Si 400), a nano-sized powder (Sigma-Aldrich nano-Si) and a type of silicon kerf (99.5% Si Resitec). The silicon powders are compared based on physical characteristics, rate performance, medium-term cycling performance and electrode resistance.

The silicon powders were physically characterized by x-ray diffraction and the Brunauer-Emmett-Teller method. Silicon electrodes were prepared by tape casting and assembled into either coin cells or three-electrode cells in half-cell configurations. The silicon electrodes in coin cells were evaluated through a rate test and a 50 cycle test. The electrode resistance was evaluated by electrochemical impedance spectroscopy of the three-electrode cells.

All the silicon powders were crystalline, but had different specific surface areas. Sigma-Aldrich nano-Si powder showed considerably higher surface area than Silgrain® e-Si 400 and 99.5% Si Resitec. The performance was evaluated based on delithiation capacity. The electrodes with Silgrain® e-Si 400 and 99.5% Si Resitec performed slightly better than the electrodes with Sigma-Aldrich nano-Si through 50 cycles. The test did not show significant capacity fade after 50 cycles for none of the three silicon powders. All three silicon powders performed similarly through the rate test. No reliable conclusion was drawn from the electrochemical impedance spectroscopy tests with respect to electrode resistance.

Sammendrag

Temaet i denne masteroppgaven er silisium anoder for litium-ion batterier. Målet ved denne masteroppgaven er å sammenlikne tre ulike typer silisiumpulvere - ett mikro-størrelse pulver (Silgrain® e-Si 400), ett nanostørrelse pulver (Sigma-Aldrich nano-Si) og en type silisium kerf (99.5% Si Resitec). Silisiumpulverne sammenliknes med hensyn på fysiske karakter, ytelse gjennom en rate-test, ytelse gjennom en mellomlang syklings test og elektrodemotstand.

Silisiumpulverne ble karakterisert ved røntgen diffraksjon og Brunauer-Emmett-Teller metoden. Silisiumelektroder ble laget ved tape casting og ble satt sammen til enten knappeceller eller tre-elektrodeceller. Knappeceller med silisiumelektroder ble evaluert gjennom en rate-test og gjennom en test med 50 sykler. Elektrodemotstand ble evaluert ved hjelp av elektrokjemisk impedansspektroskopi av tre-elektrodecellene.

Alle silisiumpulverne var krystallinske, men hadde ulike spesifikke overflateareal. Sigma-Aldrich nano-Si hadde betydelig større overflateareal enn Silgrain® e-Si 400 og 99.5% Si Resitec. Ytelsen ble målt ved delitieringskapasitet. Elektrodene med Silgrain® e-Si 400 og 99.5% Si Resitec viste litt bedre ytelse enn elektrodene med Sigma-Aldrich nano-Si over 50 sykler. Ingen av elektrodene viste betydelig reduksjon i kapasitet etter 50 sykler. Alle tre silisiumpulverne viste liknede ytelse gjennom rate-testen. Ingen pålitelig konklusjon angående elektrodemotstanden kunne trekkes fra elektrokjemisk impedansspektroskopitestene.

Contents

Preface i

Acknowledgment iii

Summary v

Sammendrag vii

1 Introduction 1

2 Theory 3

2.1 Batteries in General . . . 3
2.2 Introduction to Lithium-Ion Batteries . . . 5
2.3 Battery Terminology . . . 6
2.4 Materials Used in Lithium Ion Batteries . . . 9
2.4.1 Cathode Materials . . . 9
2.4.2 Anode Materials . . . 10
2.4.3 Electrolyte and Separators . . . 10
2.5 Silicon as an Anode Material . . . 11
2.5.1 Si as an Alloying Material . . . 12
2.5.2 Lithiation and Delithiation of Crystalline Silicon . . . 12
2.5.3 Solid Electrolyte Interphase . . . 14
2.5.4 Failure Mechanisms . . . 15
2.6 Improving Silicon Anodes . . . 16
2.6.1 Nano-Sized Silicon Morphologies . . . 16
2.6.2 Silicon Kerf for Lithium-Ion Batteries . . . 18
2.7 Characterization and Evaluation Techniques . . . 19
2.7.1 X-Ray Diffraction . . . 19

2.7.2 Surface Area Measurements by the Brunauer-Emmett-Teller Method 23
2.7.3 Electrochemical Cycling 25
2.7.4 Differential Capacity Analysis 27
2.7.5 Electrochemical Impedance Spectroscopy 28

3 Experimental **31**
3.1 Overview 31
3.2 Introduction to the Silicon Powders 31
3.2.1 Silgrain® e-Si 400 32
3.2.2 Sigma-Aldrich Nano-Si 32
3.2.3 99.5% Si Resitec 34
3.2.4 Si Kerf 34
3.2.5 BEC 01 Electrodes 35
3.3 Characterization of Silicon Powders 35
3.3.1 XRD 35
3.3.2 BET 36
3.4 Preparing Silicon Electrodes 36
3.4.1 Buffer and Binder Solutions 37
3.4.2 Mixing Slurries and Tape Casting 37
3.5 Assembling Coin Cells 39
3.6 Electrochemical Testing of Coin Cells 42
3.7 Electrochemical Impedance Spectroscopy 42

4 Results **45**
4.1 Crystallinity of Silicon Powders 45
4.2 Surface Area of Silicon Powders 48
4.3 Electrochemical Testing of Coin Cells 49
4.3.1 Precycles 49
4.3.2 50 Cycles 54
4.3.3 Rate Test 64
4.4 Electrochemical Impedance Spectroscopy 72

5 Discussion **77**
5.1 Characterization of Si powders as received 77
5.2 Electrochemical Characterization of Coin Cells 78
5.2.1 Precycling 78

5.2.2 Performance over 50 Cycles 79
5.2.3 Rate Performance 83
5.3 Electrochemical Impedance Spectroscopy Analysis 85

6 Conclusion **89**

7 Further Work **91**

Appendices **99**

A Developing Procedures for Preparing Silicon Electrodes **101**
A.1 Initial Slurry Mixing Procedure 102
A.2 Silgrain® e-Si 400 102
A.3 99.5% Si Resitec 104
A.4 Experiences from the Procedure Developement 108

B XRD Results of Silicon Powders as Received **109**

C Diffraction Patterns of Silicon and Silicon Carbide **113**

D BET Plots of the Silicon Powders **115**

Chapter 1

Introduction

McKinsey Global Institute published a report on disruptive technologies in 2013 [2]. In this report, they identify twelve technology areas with the potential of having a massive impact on industry, economics, and how people live and work in the future. One of these twelve technology areas is energy storage. The technology area energy storage consists of devices or systems that are able to store energy for later use, and batteries are the most widely known energy storage technology. The report mentions several aspects of why energy storage technology is important. Energy storage is an important factor in making electric vehicles cost competitive to vehicles with internal combustion engines. Support from an energy storage system can improve electric power reliability in places with unreliable grid infrastructure. Energy storage systems can provide electric power to remote places that are not connected to an electric grid. With an energy storage system, electric energy can be produced and stored to a later time when it is needed, instead of being used at once. This can allow electric energy produced by solar cells to be utilized at night or during cloudy days. The report, however, states that performance needs to become better and costs need to be reduced in order for energy storage to reach its full potential. It should also be mentioned that the report acknowledges the fact that technology and innovation can surprise and take unforeseen turns.

Lithium-ion batteries (LIBs) are preferred in many mobile applications, from electric and hybrid vehicles to small portable electronics. This is due to a good combination of high energy and power density [3]. Sony was the first company to commercialize this type of rechargeable battery in 1991 [4]. Today there is still ongoing research on new materials in order to improve LIBs. This research focuses improving costs, performance and safety [3].

Graphite has been a common anode material in commercialized LIBs since 1991. Silicon has attracted attention as a possible anode material for a variety of reasons. It has the ability to store more charge, while also being an abundant and cheap material. On the other hand, research is needed due to silicon anodes suffering from fast performance fade when discharged and recharged repeatedly. One of many strategies for improving performance has been to scale down silicon particles from micronscale to nanoscale [5]. However, nanoscale materials can have high production costs. On another note, silicon kerf has been examined with respect to use in battery applications. Silicon kerf is a byproduct from the solar cell industry, which could be a reliable, low-cost source of high purity silicon [6].

The main goal of this work is to compare silicon anodes made from three different types of silicon powders - a commercialized micronscale powder, a nanoscale powder, and a type of silicon kerf. These silicon powders have been produced differently and have different particle sizes. In this thesis the silicon powders are physically characterized by x-ray diffraction analysis and the Brunauer, Emmett and Teller method. Si anodes are prepared and assembled into coin cells, before being evaluated by medium-term cycling performance and rate performance. The Si anode resistances are also evaluated through electrochemical impedance spectroscopy.

Chapter 2

Theory

2.1 Batteries in General

Batteries can store energy as chemical energy and supply electrical energy upon request. A battery cell consists of a cathode, anode and electrolyte. The cathode and anode are also referred to as electrodes. The two electrodes are connected into a closed circuit by an external circuit and electrolyte as illustrated in figure 2.1.

Batteries convert chemical energy into electrical energy by spontaneous reduction and oxidation reactions. Electrons are released at the anode by an oxidation reaction. The electrolyte is a poor electrical conductor, so the electrons are forced to flow through the external circuit towards the cathode. The electrons undergo a reduction reaction at the cathode. An electrical current arises from the electrons flowing through the external circuit, and can power electrical devices [4]. The electrolyte closes the circuit by allowing ions to pass between the electrodes.

There are three main categories of battery cells: primary cells, secondary cells and fuel cells. Primary cells can only be discharge, while secondary cells can also be recharged. Primary and secondary cells both have a finite amount of chemical reactants and can therefore only supply an electrical current for a limited amount time before they are fully discharged. In contrast, fuel cells have a continuous flow of chemical reactants and can produce a continuous current [4].

In secondary battery cells, the reduction and oxidation reactions can occur on both electrodes. Which of the electrodes that is the cathode or anode depends on if the battery is being

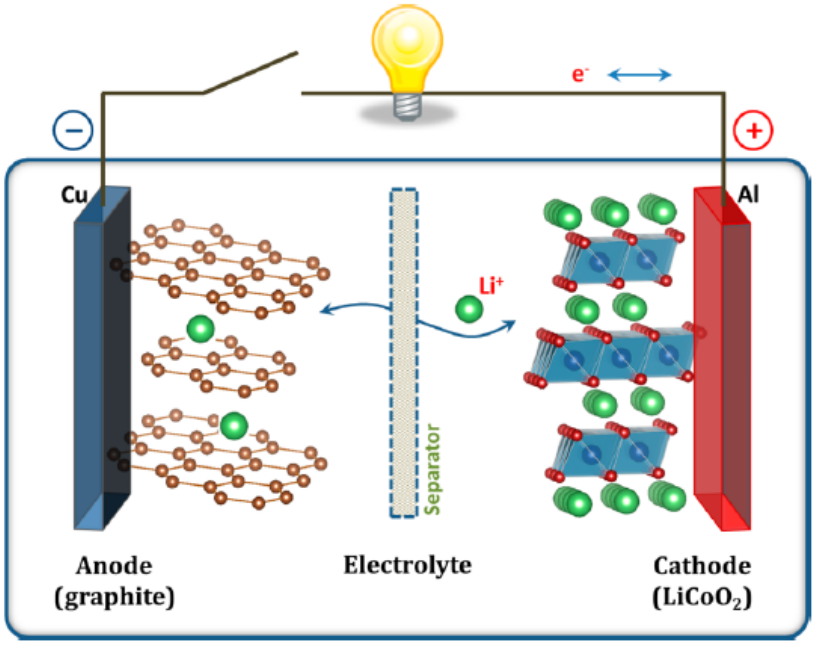

Figure 2.1: Schematic illustration of a LIB with a $LiCoO_2$ cathode (positive electrode) and a graphite anode (negative electrode). The electrodes are connected by an external circuit and separated by an electrolyte and separator. During discharging the electrons (e^-) and Li-ions (Li^+) flow from the graphite anode to the $LiCoO_2$ cathode through the external circuit and the electrolyte, respectively. The flow direction is opposite during charging. Figure from [7].

discharged or recharged. To avoid confusion, the terms positive and negative electrodes are often used instead of cathode and anode. The cathode during discharge is called the positive electrode, while the anode during discharge is called the negative electrode [8]. In this report the use of the words cathode and anode, refer to the positive electrode and negative electrode respectively.

There exist many different types of secondary battery technologies. Figure 2.2 compares the specific energy densities and volumetric energy densities of lead-acid, nickel-cadmium ($Ni-Cd$), nickel-metal-hydrid ($Ni-MH$) and lithium-ion (Li-ion) secondary batteries. From the figure lithium-ion batteries have the highest energy density both with respect to mass and volume. It should on the other hand be noted that this figure was produced in 2009, and energy density values could be outdated [9].

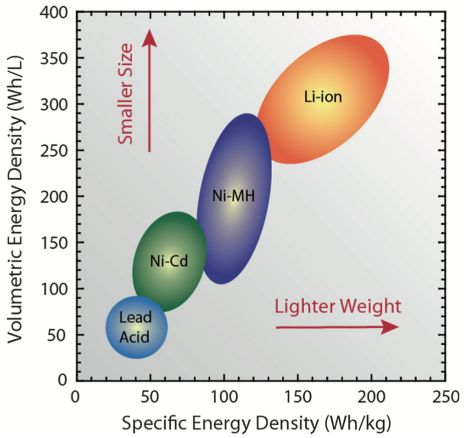

Figure 2.2: Specific and volumetric energy densities of different types of secondary battery technologies. Figure from [10].

2.2 Introduction to Lithium-Ion Batteries

This report will further only focus on lithium-ion secondary batteries (LIBs). The battery cell illustrated in figure 2.1 is also called the Sony cell, and was the first commercialized LIB in 1991. The cathode had lithium cobalt oxide ($LiCoO_2$) as active material and aluminium (Al) foil as current collector, while the anode had graphite (C) as active material and copper (Cu) foil as current collector. Both $LiCoO_2$ and graphite are intercalation materials because they can host Li-ions in between layers of their structure. $LiCoO_2$ has Li-ions in between layers of a CoO_2 structure, while graphite has the capability of hosting Li-ions in between layers of carbon hexagons [4]. The Li-ions and electrons are transported between the cathode and anode during discharging and charging. The electrochemical reactions happening in a Sony cell are [7]:

Positive electrode:

$$\mathrm{Li}_{1-x}\mathrm{CoO}_2 + \mathrm{xLi}^+ + \mathrm{xe}^- \underset{\text{Charge}}{\overset{\text{Discharge}}{\rightleftharpoons}} \mathrm{LiCoO}_2 \tag{2.1}$$

Negative electrode:

$$\mathrm{C}_6\mathrm{Li}_x \underset{\text{Charge}}{\overset{\text{Discharge}}{\rightleftharpoons}} \mathrm{C}_6 + \mathrm{xLi}^+ + \mathrm{xe}^- \tag{2.2}$$

Total reaction:

$$\mathrm{Li}_{1-x}\mathrm{CoO}_2 + \mathrm{C}_6\mathrm{Li}_x \underset{\text{Charge}}{\overset{\text{Discharge}}{\rightleftharpoons}} \mathrm{LiCoO}_2 + \mathrm{C}_6 \tag{2.3}$$

During charging Li-ions are transported from the cathode to the anode and the anode is *lithiated*. The ionic transport is in the opposite direction during discharge. Li-ions then migrate from the anode to the cathode and the anode is *delithiated*. Furthermore, LiCoO_2 and graphite have different structures depending on the degree of lithiation. This can cause degradation of the LiCoO_2 cathode. The cathode is therefore not fully delithiated during operation, but generally keeps a composition between ($\mathrm{Li}_{0.5}\mathrm{CoO}_2$) and ($\mathrm{Li}_{0.9}\mathrm{CoO}_2$) [4].

Before getting further into LIBs and silicon, it is advantageous to present some battery terminology.

2.3 Battery Terminology

The *current*, I, passing through a battery cell during discharging or charging is the rate at which charge is transferred [8]:

$$I = \frac{dq}{dt} \tag{2.4}$$

q is charge and t is time.

The amount of charge transferred through a battery is dependent on the current and for how long time the current passes. If a constant current, I, is transferred through a battery during discharging or charging for a time Δt, the total amount of charge transferred, $Q(I)$, is [7]:

$$Q(I) = \int_0^{\Delta t} I dt \tag{2.5}$$

The amount of charge transferred during discharging or charging, is also called *capacity*. Often capacity is given in terms of charge per weight or per volume. These are termed *specific capacity* and *charge density*, respectively. It should also be noted that the capacity of a battery is dependent on the current, because the rate at which ions are transferred in the electrolyte can become diffusion-limited at high currents [7].

The capacity of an electrode is related to the amount of active material, which is often given in terms of *loading*. The loading of an electrode is the amount of active material per unit

area. Although a higher loading would yield a higher theoretical capacity, there is a trade-off between the loading and the achieved degree of lithiation. Lower loadings typically achieve a higher degree of lithiation, as charge rates in practice have a certain finite value. In other words, an electrode with lower loading will in practice achieve a higher specific capacity than an electrode with higher loading [11]. This implies that several possible loadings can be used to achieve the same total capacity.

The *open circuit voltage* of a battery cell, V_{oc}, is as given the difference between the electrochemical potentials of the anode and cathode [7]:

$$V_{oc} = \frac{\mu_a - \mu_c}{e} \tag{2.6}$$

μ_a and μ_c are the *electrochemical potentials* of the anode and cathode, respectively. e is the *elementary charge*.

When a battery is discharged, the *output voltage* of the battery, V_{dis}, is lower than the open circuit voltage, V_{oc}, due to internal resistances in the battery. When a battery is charged, the internal resistance of the battery increases the necessary *input voltage*, V_{ch}, by an overvoltage as well. The reduction and increase of output and input, respectively, is given by η. The resulting voltages for both cases are [7]:

$$V_{dis} = V_{oc} - \eta(q, I_{dis}) \tag{2.7}$$

$$V_{ch} = V_{oc} + \eta(q, I_{ch}) \tag{2.8}$$

q denotes the *state-of-charge*, which is often referred to as degree of lithiation in context of LIBs. I_{dis} and I_{ch} are the currents at which the battery is discharged and charged, respectively.

The *power* produced by a battery cell, P, is given by the current, I_{dis}, and output voltage, V_{dis}

$$P = I_{dis} * V_{dis} \tag{2.9}$$

The *energy* supplied from a battery cell, E, is dependent of the output voltage of the battery and the charge transferred through the battery. Provided a constant current, I_{dis}, an output voltage, V_{dis}, for a time Δt, the energy supplied is given by [7]:

$$E = \int_0^{\Delta t} I_{dis} * V_{dis}(t)dt = \int_0^{Q} V(q)dq \tag{2.10}$$

The energy that can be provided by a battery cell is often given per unit weight or per volume. These parameters are termed *gravimetric energy density* and *volumetric energy density*, respectively [7].

A *cycle* consists of a discharging process followed by a charging process, or vice versa. The *coulombic efficiency*, CE, of a single cycle is the ratio between the discharge capacity, Q_{dis}, and charge capacity, Q_{ch}:

$$CE(\%) = \frac{Q_{dis}}{Q_{ch}} * 100\% \tag{2.11}$$

The *irreversible capacity loss*, ICL, and the *cumulative irreversible capacity loss*, $CICL$, are defined as [12]:

$$ICL = Q_{ch} - Q_{dis} \tag{2.12}$$

$$ICL(\%) = \frac{Q_{ch} - Q_{dis}}{Q_{ch}} * 100\% \tag{2.13}$$

$$CICL = \sum_n (Q_{ch} - Q_{dis})_i \tag{2.14}$$

n is the number of cycles the irreversible capacity loss is accumulated from.

The terms *cyclability* and *cycle stability* are often encountered in literature about secondary batteries. Both these terms refer to how well the battery performance is maintained over many cycles.

The discharging and charging capacities are, as mentioned, dependent on how large the current is. It is therefore important for battery manufacturers to state the discharging or charging rates when stating the capacity of a battery. *Rated capacity* is the amount of charge a battery can deliver when supplying a constant current down to a specific end-of-discharge voltage at an ambient temperature (20°C±5°C) [13]. Furthermore, *C-rate* is a way of stating the rate at which a battery is being charged or discharged. When a battery at its fully charged state is fully discharged in t hours, the C-rate is C/t [14]. A battery with a rated

capacity of 40 mAh discharged at 0.05C will deliver a constant current of 2 mA for 20 hours from a fully charged state.

2.4 Materials Used in Lithium Ion Batteries

There exist a range of materials used in commercialized LIBs. In addition, there is a range of materials being researched, which can potentially be used in LIBs. The research and development of materials for LIBs aims to improve both performance factors and practical issues related to battery usage. A few examples are to achieve higher energy and power densities, improve cycle life, and improve safety and lower costs [3]. This section will briefly mention a few cathode materials, anode materials, electrolytes and separators.

2.4.1 Cathode Materials

Lithium cobalt oxide ($LiCoO_2$; LCO) was as mentioned the first cathode material in commercialized, rechargeable batteries (Sony cells). Since then many new materials have been researched. Examples of other present commercialized intercalation cathode materials are lithium manganese oxide ($LiMn_2O_2$; LMO), lithium iron phosphate ($LiFePO_4$; LFP), lithium nickel cobalt aluminium oxide ($LiNi_{0.8}Co_{0.15}Al_{0.05}O_2$; NCA), lithium nickel manganese cobalt oxide ($LiNi_xMn_yCo_{1-x-y}O_2$; NMC or NCM) [3, 15]. The latter has most commonly the ratio $LiNi_{0.33}Mn_{0.33}Co_{0.33}O_2$ or $LiNi_{0.5}Mn_{0.3}Co_{0.2}O_2$ [15].

Each cathode material has different advantages, disadvantages, and is used in different applications. As an example, LCO has the advantages of having a relative high specific capacity, high energy density, low self-discharge, high discharge potential and good cycle performance. The disadvantages are safety issues due to low thermal stability, high cost due cobalt (Co) and fast capacity fade at high currents [3]. LCO is mainly used in smaller portable electronics [15]. LFP, on the other hand, has the advantages of good thermal stability and high power capability. The disadvantages are relative low average discharge potential [3]. LFP is mainly used in high power applications as power tools and energy storage [15].

The amounts of the different cathode materials used in 2015 were as following: LCO with 45 kilotons; NMC with 35 kilotons; LMO with 18 kilotons; LFP with 10 kilotons; NCA with 9 kilotons. The forecast for production following 2015 predicts that there will be a development in the popularity of the different cathode materials. The forecast predicts production of LCO

and LFP to level off, but also predicts a growth in production of NMC, LMO and NCA [15].

2.4.2 Anode Materials

Carbon materials, as graphite and hard carbon, remain popular as active anode materials. The reason for this is due to low cost, abundancy, high Li diffusivity, high electronic conductivity, low delithiation potential versus Li/Li^+ and low volume changes during a charge and discharge cycle. Lithium titanium oxide ($Li_4Ti_5O_{12}$; LTO) is another commercialized anode material used for high power applications. LTO has good thermal stability, relative high volumetric capacity and high cycle life. Two drawbacks of using LTO is higher costs due to titanium (Ti) and reduced cell voltage when compared to carbon materials. Both Silicon (Si) and Tin (Sn) have both received attention as possible anode materials [3]. Si as an anode material will be discussed in section 2.5.

2.4.3 Electrolyte and Separators

The electrolyte is the medium that transports the Li-ions between the cathode and anode. Electrolytes can be categorized as non-aqueous liquid electrolytes, gel electrolytes, solid polymer electrolytes, ionic liquid electrolytes or ceramic electrolytes. Non-aqueous liquid electrolytes are most widely used [9]. Such electrolytes consist of lithium salt in an organic liquid. A typical electrolyte is based on lithium hexafluorophosphate ($LiPF_6$) in a mixture of ethylene carbonate (EC) and diethyl carbonate (DEC) in 1:1 ratio [4]. Dimethyl carbonate (DMC) and ethylmethyl carbonate (EMC) have also been used instead of DEC [13]. Additives are also often added to the electrolyte mixtures, and can for example assist in preserving safety as a flame-retardant [13].

The separator is a porous membrane between the cathode and anode. The main task of the separator is to hinder contact between the cathode and anode, while allowing Li-ions to pass. Contact between the cathode and anode would cause a short circuit. The separator does not take part in the cell reactions, but is important for the cell performance and safety. A separator needs to exemplify several properties in order to accommodate for good ionic conductivity, cycle life and safety. These properties include mechanical, chemical and thermal stability, in addition to porosity [13] and electronic insulation [16]. Polyolefin membranes, such as polyethylene (PE) and polypropylene (PP), are widely used as separators in LIBs [13, 16].

2.5 Silicon as an Anode Material

An ideal anode material for LIBs should be stable over many cycles, as it is expected from a consumer point of view that secondary batteries can be discharged and charged many times. Julien et al. (2016) presented several other properties that an ideal active anode material should have as well [17]:

1. Accommodate large amounts of lithium and still be lightweight
2. Have a low potential with respect to Li/Li^+ at any lithium concentration
3. Have a good electronic and ionic conductivity
4. Not be soluble in electrolyte solvents or reactive with lithium salts
5. Be safe
6. Be cheap and environmentally friendly

Accommodating a large amount of lithium with respect to weight is important for obtaining a high gravimetric capacity. A low potential with respect to Li/Li^+ is important for obtaining a high cell voltage, and furthermore a high energy density by equation 2.10. Good electric and ionic conductivities allow fast transport of electrons and Li-ions, which results in a higher power density. Being safe is needless to say important, but this is especially important for usage within electric vehicles and airplanes.

Si as an anode material fulfills point one because it is an alloying materials, which can hold a lot of lithium. Si also fulfills point two because it has a low potential with respect to Li/Li^+. The third point is fulfilled in spite of Si being a semiconductor. The fourth point is also fulfilled [17]. Si is also considered abundant and cheap, not to be toxic, environmentally friendly, and to be safe [5].

Si has many attractive properties, but unfortunately, has poor cycling stability. This issue is related to large changes in volume during cycling. The next sections in this report will describe the lithiation and delithiation of Si and failure mechanisms. Lastly, a few strategies for improving Si anodes for LIBS will be presented.

2.5.1 Si as an Alloying Material

As mentioned earlier, Si is an alloying anode material. In contrast to intercalation materials, as graphite (C), where Li take a position within a host structure, alloying materials form phases with Li [3]. Alloying materials can in general store more Li than intercalation materials. This is clear when comparing Si and graphite. Graphite can store up to 0.17 Li atoms per C atom (LiC_6), and has a theoretical specific capacity of 372 mAh/g [5] and a charge density of 719 Ah/L [18]. Si can store up to 3.75 Li atoms per Si atom ($Li_{15}Si_4$ or $Li_{3.75}Si$), and has a specific capacity of 3579 mAh/g and a charge density of 2194 Ah/L [18].

It should be noted that some places in literature state that the fully lithiated form of Si has 4.4 Li atoms per Si atom ($Li_{22}Si_5$ or $Li_{4.4}Si$), and has a specific capacity of 4199 mAh/g. This is believed because $Li_{22}Si_5$ is the phase with most Li relative to Si in the Li-Si phase diagram. On the other hand, at room temperatures, the observation of this extra capacity might be attributed to lithiation of surface oxides or formation of a surface layer, the so called SEI, which is further explained in section 2.5.3. X-ray diffraction and transmission electron microscopy results have shown that the fully lithiated state of bulk Si, Si thin films and nano-Si to be $Li_{15}Si_4$ [18].

2.5.2 Lithiation and Delithiation of Crystalline Silicon

Several studies have investigated the lithiation of silicon by techniques such as *in-situ* nuclear magnetic resonance (NMR), *in-situ* x-ray diffraction (XRD) and *in-situ* transmission electron microscopy (TEM). The studies show that crystalline Si (c-Si) is lithiated and converted to an amorphous phase, denoted a-Li_xSi, which is further converted into a heavily lithiated and crystalline phase, denoted c-$Li_{3.75}Si$ or c-$Li_{15}Si_4$ [19]. Some have also mentioned the possibly overlithiated phases such as c-$Li_{3.75+\delta}Si$ or $Li_{4.2}Si$ and $Li_{4.4}Si$.

Ogata et al. (2014) studied the kinetics of lithitiation and delithiation of Si [19]. In their work, they employed *in-situ* NMR studies, systematic electrochemical characterization, *ex situ* XRD, *ex-situ* magic angle spinning (MAS) NMR spectroscopy and density-functional theory (DFT). The study focuses on lithiation and delithiation from the second cycle and further. They studied Si nanowires on carbon supports against a Li metal counter electrode, also referred to as half-cell configuration. Their conclusions are summarized in table 2.1. The potentials stated further in this section are versus Li/Li^+.

The first discharge is different from the following discharges. This is due to crystalline

Table 2.1: Lithiation and delithiation of Si based on the study of Si nanowires in [19]. $\delta = 0.2 - 0.3$ and $x \sim 3.5$.

First lithiation of crystalline Si	
c-Si $\longrightarrow$ a-Li_xSi $\longrightarrow$ c-$Li_{3.75}Si$ $\longrightarrow$ c-$Li_{3.75+\delta}Si$	0.10 V
Subsequent lithiation of amorphous Si	
a-Si $\longrightarrow$ a-$Li_{2.0}Si$	0.30-0.25 V
a-$Li_{2.0}Si$ $\longrightarrow$ a-$Li_{3.5}Si$	0.10 V
a-$Li_{3.75}Si$ $\longrightarrow$ c-$Li_{3.75}Si$	0.05 V
c-$Li_{3.75}Si$ $\longrightarrow$ c-$Li_{3.75+\delta}Si$	0.03V
Delithiation of Si	
c-$Li_{3.75+\delta}Si$ $\longrightarrow$ c-$Li_{3.75}Si$ + c-$Li_{3.75-\delta}Si$	0.05-0.15 V
a-$Li_{3.5}Si$ $\longrightarrow$ a-$Li_{2.0}Si$	0.27-0.30 V
c-$Li_{3.75}Si$ $\longrightarrow$ a-$Li_{1.1}Si$	0.43 V
a-$Li_{2.0}Si$ $\longrightarrow$ a-Si	0.5 V

Si becoming amorphous upon lithiation and it does not return to the original crystalline structure when delithiated. Rather it delithiates to amorphous Si. During the first discharge, crystalline Si is converted to a-Li_xSi at 100 mV and further into c-$Li_{3.75}Si$ if lithiated enough.

During the subsequent discharges, the lithiation processes are different. These discharges start with amorphous Si lithiated into a-$Li_{\sim 2.0}Si$ at ∼300-250 mV. This phase contains extended Si networks and large Si-Si clusters. a-$Li_{\sim 2.0}Si$ is then lithiated to a-$Li_{\sim 3.5}Si$ at 100 mV [20]. Here the Si-to-Si bonds are further broken to create smaller Si clusters. Eventually, all Si anions are isolated. The amorphous lithiated Si phase is transformed into the crystalline phase c-$Li_{3.75}Si$ at 50 mV. Upon further lithiation, the over-lithiated phase c-$Li_{3.75+\delta}Si$ is formed at 30 mV. Here δ has the value 0.2-0.3.

Obrovac and Chevrier (2014) describe the lithiation and delithiation process of Si in a review of alloy negative electrodes for LIBs as well [18]. Lithiation and delithiation reactions can happen in two-phase or single-phase reactions. When plotting voltage versus specific capacity, such reactions will appear as a voltage plateaus or sloping voltage curves, respectively. Both the lithiation of c-Si to an amorphous phase and the delithiation of c-$Li_{3.75}Si$ happens through two-phase reactions, causing voltage plateaus.

2.5.3 Solid Electrolyte Interphase

A layer of decomposed electrolyte forms on silicon particles during cycling of silicon anodes. This layer is referred to as the solid electrolyte interphase (SEI). In a LIB with the combination of a Si anode and a conventional EC-based electrolyte with $LiPF_6$ salt, the SEI layer typically contains LiF, lithium alkoxides, polyethylene oxides and carbonates, lithium alkyl carbonates and polycarbonates and nonconductive polymers [17, 9].

A SEI layer is formed on an anode due to reduction of electrolyte. The electrolyte is reduced at the anode because the lowest unoccupied molecular orbital (LUMO) of the electrolyte is below the electrochemical potential of the anode (μ_A). Similarly, the electrolyte is oxidized at the cathode if the highest occupied molecular orbital (HOMO) of the electrolyte is above the electrochemical potential of the cathode (μ_C) [7] . If the electrochemical potentials of the anode and cathode are between the LUMO and HOMO, as in figure 2.3, then these reactions will not occur. However, no conventional electrolyte has a LUMO above the electrochemical potentials of graphite or Si.

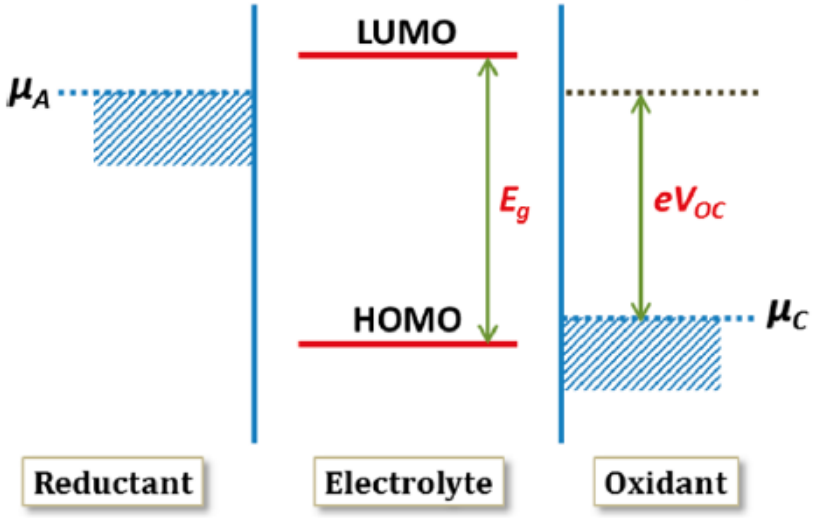

Figure 2.3: Schematic energy diagram of a battery with liquid electrolyte. The electrolyte will not be reduced at the anode because the electrochemical potential of the anode (μ_A) is below LUMO of the electrolyte. The electrolyte will not be oxidized at the cathode because the electrochemical potential of the cathode (μ_C) is above the HOMO of the electrolyte. E_g is the energy difference between LUMO and HOMO. V_{oc} is the open-circuit voltage, as defined in equation 2.6. e is the elementary charge. Figure from [7].

There are both positive and negative aspects of having a SEI layer. It is beneficial for the

cyclability of a LIB to have a passivizing and stable SEI layer on the anode because it can prevent further electrolyte decomposition. An ideal SEI layer is electrically insulating in order to prevent electrons from passing through the SEI layer and reduce more of the electrolyte. An ideal SEI layer is also ionically conducting with respect to Li-ions to enable lithiation and delithiation of the anode. It should also be uniform and flexible with respect to volume changes [9]. One of the major issues with using Si as an anode material is a continuous SEI formation due to expansion and exposure to fresh Si surface. This is called unstable SEI formation and will be further described in section 2.5.4.

2.5.4 Failure Mechanisms

Si anodes in LIBs suffer from poor cyclability and rapid capacity fade. The failure mechanisms causing this are related to the large volume changes that Si can experience through cycling. A review of Si anodes done by Ma et al. (2014) considers $Li_{22}Si_5$ as the fully lithiated state and the volume change to be as high as 400% [5]. In another review of alloying anode materials by Obrovac and Chevrier (2014), $Li_{15}Si_4$ is considered as the fully lithiated state and the volume change to be up to 280% [18].

The large volume changes during cycling cause high internal stress on the Si. This causes Si particles to pulverize during cycling, as illustrated in figure 2.4. The volume changes and pulverization can lead to Si particles losing contact with neighboring particles and the current collector, and results in isolated inactive Si particles [21]. The pathways for electrons through the anode are disrupted [5], causing a loss of electrical conductivity [21].

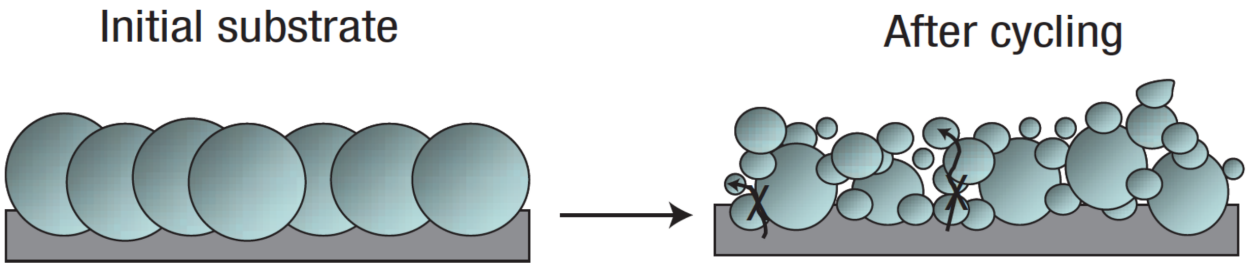

Figure 2.4: Illustration of the pulverization of Si particles. The volume changes experienced during cycle causes the Si particles to pulverize and lose contact with neighboring particles and current collector. Figure edited from [22].

The large volume changes during also contribute to formation and growth of an unstable SEI layer, as illustrated in figure 2.5. During lithiation, the Si particles expand and a SEI

layer forms on the surface of the particles. Upon delithiation the Si particles contract and the SEI layer fractures into pieces, which exposes new Si surface to the electrolyte. New SEI can form on the exposed Si surface upon further cycling. A thick SEI layer can build up around the Si particles after many cycles [5]. A thick SEI layer is an electric insulator that can deactivate Si particles and increase the polarization of the Si anode [5, 21]. In addition, Li-ions and electrolyte are consumed during this continuous SEI growth [21].

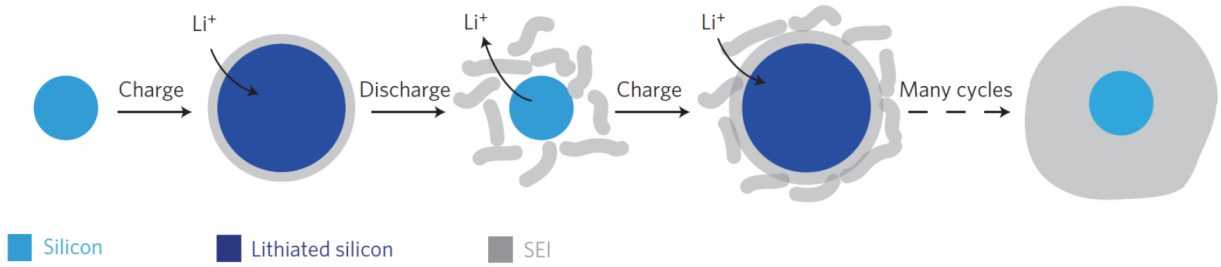

Figure 2.5: Illustration of SEI growth and cracking during cycling. The Si particle lithiates and expands during charging while a SEI layer forms on the Si particle surface. The Si particle delithiates and contracts during discharging, and the SEI layer cracks. The cracking of the SEI layer exposes the surface of the Si particle where new SEI can form upon further cycling. The SEI layer becomes thick after many cycles. Figure edited from [23].

2.6 Improving Silicon Anodes

Several strategies have been employed in trying improve the performance of Si anodes. Electrolyte additives have been studied to create a more stable SEI layer. Different types Si morphologies have been studied to accommodate volume changes, create shorter Li diffusion paths or provide a continuous electron pathway in the anode [5]. Also, combining Si with a conductive additive, such as carbon (C), has helped battery performance. Conductive additives improve the electrical conductivity of the Si anode, but also help accommodate for volume change [21].

2.6.1 Nano-Sized Silicon Morphologies

One strategy used to improve Si anodes has been to downsize Si from bulk to nano-sized morphologies with high surface-to-volume ratios [5, 21, 24]. Surface atoms are less stabilized

than bulk atoms because they have lower coordination numbers and more unsatisfied bonds. Nano-sized structures, therefore, have high average binding energy per atom [25], which helps to accommodate the large volume changes of Si. This helps to prevent pulverization [21]. The large specific surface area allows efficient transfer of Li-ions from the electrolyte to the nano-sized Si structures as well, yielding a high rate capability. Also, nano-sized Si morphologies provide short Li-ion diffusion distances in the anode. However, there is a trade-off for nano-structured Si anodes. The large area is exposed to the electrolyte, causes a high irreversible capacity loss due to SEI formation on a larger surface [24].

Several different nano-sized morphologies have been tested. A few of these include Si nanoparticles (0D), Si nanowires (1D) and Si thin films (2D) [21]. A study has shown 150 nm to be the critical size for nanoparticles. Particles below this size do not fracture during cycling [26]. Si nanoparticles often have simple particle syntheses and are relative easy to scale up. However, after repeatedly being expanded and contracted, Si anodes with nanoparticles still delaminate from the current collector and experience loss of electrical conductivity due to the disruption of electron pathways. There is an irreversible capacity loss due to SEI formation that increases with decreasing particle sizes as well [24]. Si nanowires can be grown directly on a current collector accommodate volume changes well, as seen in figure 2.6. Such a configuration forms a direct electron pathway and eliminates the need for binding materials and conducting additives [22].

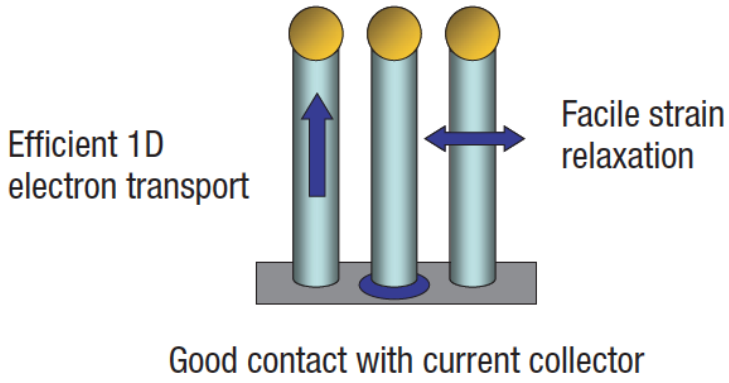

Figure 2.6: Si nanowire grown directly onto a current collector. The figure illustrates the the 1D current pathway, the good connection to the current collector and the possibility to accommodate volume expansions. Figure from [22].

2.6.2 Silicon Kerf for Lithium-Ion Batteries

Si kerf is a byproduct from the Si solar cell industry. More specifically, Si kerf is the sawdust produced when Si blocks are sawed into thin Si wafers. A large amount of Si kerf is produced during the sawing process. For instance, Huang et al. reported in 2016 there was a nearly 40% Si loss to Si kerf in slurry-based sawing processes [6]. Si kerf has, on the other hand, attracted attention for use in Si anodes for LIBs due it being a low-cost and reliable source of high purity Si.

There are different methods employed to sawing Si block into Si wafers. Two methods used are sawing by blades or sawing using a slurry. A slurry-based sawing process involves abrasive particles suspended in a carrier fluid - slurry. The slurry is held by a network of moving wires and the Si blocks are pushed through the wires, sawing the blocks into wafers. Silicon carbide particles (SiC) are commonly used as abrasive particles, while polyethylene glycol (PEG) is commonly used as carrier fluid [27]. The slurry-based sawing process is illustrated in figure 2.7.

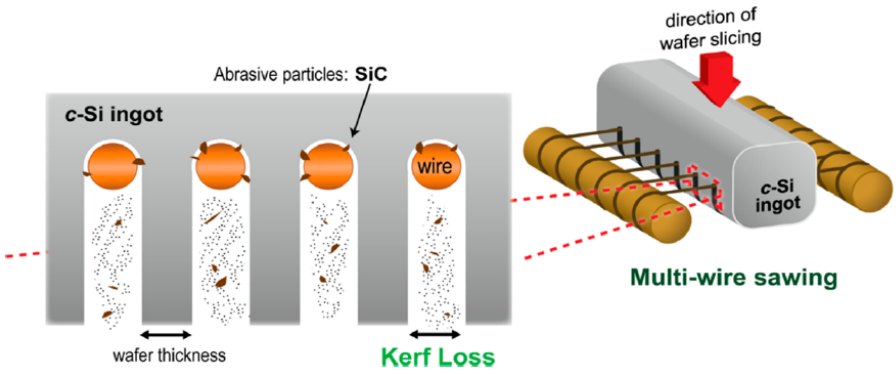

Figure 2.7: Slurry-based sawing process of a Si block into Si wafers. SiC particles used as abrasive particles. Figure from [6].

SiC is an electric insulator and inactive in reacting with Li-ions [28]. The presence of SiC has been seen as a problem, and extraction techniques have been developed to remove SiC from the kerf. There have also been done studies without removing SiC, but rather use the abrasive particles to aid the milling process and act as pillars to enhance the mechanical integrity of the anode. Huang et al. studied a composite powder of milled SiC containing Si kerf in a composite with nickel (Ni) as conducting additive [6]. The study showed cycle stability over 100 cycles.

2.7 Characterization and Evaluation Techniques

There are a number of ways to evaluate electrode materials. In this section both physical and electrochemical characterization techniques will be presented. X-ray diffraction and Brunauer, Emmett and Teller method will be described, half-cell configuration will be introduced, electrochemical cycling and differential capacity analysis will be presented, and lastly electrochemical impedance spectroscopy will be presented.

2.7.1 X-Ray Diffraction

X-ray diffraction (XRD) is an important physical technique used to determine structures of solid materials. X-rays are used because they have wavelengths (0.1 Å to 10 Å [29]) comparable to the spacing between atoms in a crystal (typically ∼2 Å [30]). The XRD technique is commonly used to identify solid materials. Many XRD results from known samples have been gathered in databases. These results are called diffraction patterns and act as fingerprints. An unknown sample can be identified by comparing the diffraction pattern for the sample to diffraction patterns in the database [31].

Parallel, monochromatic and coherent x-rays are irradiated onto a test sample during an XRD analysis. The x-rays are scattered and detected by a detector. The test sample is irradiated over a range of angles during the course of an analysis. At some angles, the x-rays are scattered and constructively interfere with each other [32]. If the test sample is a crystalline material, it will have a periodic array of atoms and can produce a large number of scattered waves that can constructively interfere. This will be detected as a strong signal by the detector [33] and is referred to as a diffracted beam [34]. At other angles, the x-rays are scattered and destructively interfere. This will be detected as a weak signal by the detector. The result of an XRD analysis is given in a diffraction pattern, which is obtained by plotting the intensity of the signal against the *diffraction angle*. The diffraction angle, 2θ, can be seen as the angle between x-rays irradiated by the source and the x-rays intercepted by the detector, see figure 2.8.

Diffraction of x-rays is illustrated in figure 2.8. Two parallel, monochromatic and coherent x-rays are irradiated onto a crystalline test sample at an incident angle θ. The x-rays are elastically scattered by two parallel planes in the crystalline sample. Consider the x-rays scattered with an exit angle θ. The lower x-ray has a longer path length than the upper x-ray. The path difference between the upper and lower x-rays is $2d_{hkl}\sin\theta$ - the sum of the

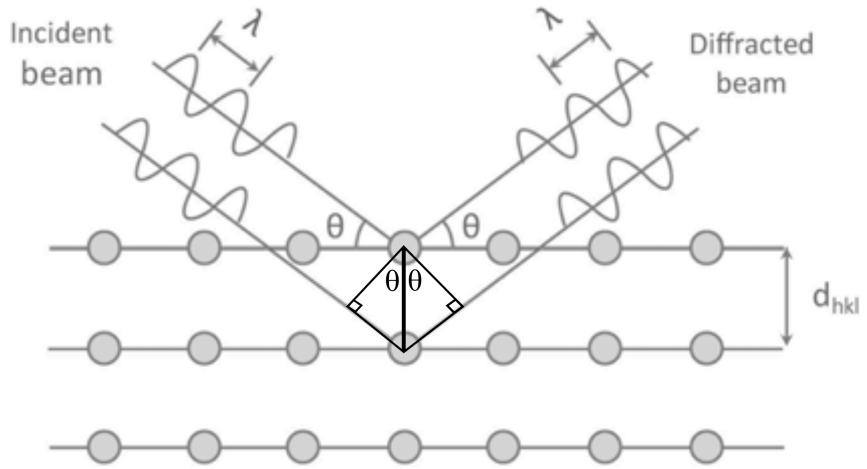

Figure 2.8: Illustration of scattering of a diffraction beam in a crystalline material. Two parallel, monochromatic and coherent x-rays irradiate a sample at an angle θ and are elastically scattered at an angle θ. Figure edited from [35].

lengths of the two cathetuses opposite of θ in the drawn triangles. Constructive interference will occur if the path difference between the two is equal to an integer multiplied by the wavelength of the x-rays, $n\lambda$. A large number of such events will result in a diffracted beam. This condition for diffraction is given by Bragg's law [34, 33]:

$$n\lambda = 2d_{hkl} \sin\theta \tag{2.15}$$

n is *order* of reflection and denotes an integer (smallest value is 1). θ is the incident angle of the x-rays compared to the planes. d_{hkl} is the distance between two parallel, adjacent planes with *Miller indices* h, k and l in the crystalline sample. For cubic structures d_{hkl} can calculated by [34]:

$$d_{hkl} = \frac{a}{\sqrt{h^2 + k^2 + l^2}} \tag{2.16}$$

a is the lattice parameter.

There are only a few angles that satisfy Bragg's law. At most angles the scattered x-rays are out of phase and will cancel out each other [33]. Furthermore, it should be mentioned that Bragg's law does not give information about the intensity values [36]. In addition, there are scattering events that fulfill Bragg's law, which do not appear as intensity peaks in a diffraction pattern. Bragg's law is sufficient to find intensity peaks for crystalline materials

with atoms in the unit cell corner positions. Many crystalline materials have atoms in other positions that can scatter out of phase x-rays [34]. The result is that the intensity values of the diffracted beams can vary. Several factors affect the intensity of the diffracted beams. One factor is the *structure factor*, F, and the intensity is proportional to $|F|^2$. The structure factor is calculated by [33]:

$$F_{hkl} = \sum_j f_j \exp[2\pi i(hx_j + ky_j + lz_j)] \tag{2.17}$$

f_j is the *atomic factor* for atom j in a unit cell. h, k and l are the Miller indices of the peak. x_j, y_j and z_j are *fractional coordinates* of the atoms in the unit cell.

To illustrate the effect of the structure factor, it is possible to use Si as an example. Pure Si has a diamond structure at room temperature. The diamond structure can be described as a face-centered cubic lattice (FCC) with a two-atomic basis. The FCC lattice has fractional coordinates of (0 0 0), (1/2 1/2 0), (1/2 0 1/2) and (0 1/2 1/2) relative to a cubic cell. The atoms in the two-atomic basis have coordinates (0 0 0) and (1/4 1/4 1/4). All atoms in the diamond structure are identical [33, 36]. The structure factor of Si can be shown to be:

$$F_{hkl} = f_{Si}[1 + (-1)^{h+k} + (-1)^{h+l} + (-1)^{k+l}][1 + \exp(\frac{\pi}{2} i(h + k + l))] \tag{2.18}$$

Different combinations of h, k and l give different values for F^2 [33]:

$${F_{hkl}}^2 = \begin{cases} 0, & \text{h, k, l are mix of odd and even numbers} \\ 32{f_{Si}}^2, & h + k + l = \text{odd number} \\ 64{f_{Si}}^2, & h + k + l = 2 * \text{even number} \\ 0, & h + k + l = 2 * \text{odd number} \end{cases} \tag{2.19}$$

hkl combinations where ${F_{hkl}}^2$ is equal to zero do not show as intensity peaks in the diffraction pattern of Si.

In addition to identifying crystalline materials, XRD analysis can also be used to estimate average crystallite sizes. Small crystallites cause broadening of the intensity peaks, as illustrated in figure 2.9. The reason for this is that small crystallites lack planes to completely cancel out scattered the x-rays at angles close to those that fulfill Bragg's law [33]. The average crystal size can be calculated by Scherrer's formula [37]:

$$t = \frac{K\lambda}{\beta \cos \theta_B} \tag{2.20}$$

t is the average size of the crystals. K is *Scherrer's constant* and has usually the value 0.89. β is the *full-width at half maximum* (FWHM) of the peak assessed. θ_B is the angle of the peak being assessed.

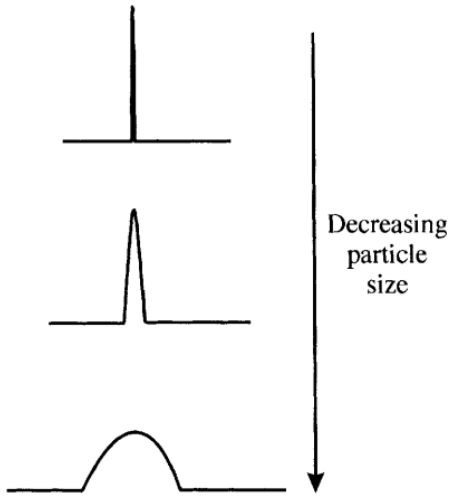

Figure 2.9: Simple illustration of how crystallite size affects the intensity peaks in a diffraction pattern. Small crystallite sizes give broader intensity peaks. Figure from [38].

The focus in this section has been on crystalline materials. They have a periodic structure and will have diffraction patterns with narrow and sharp intensity peaks. Amorphous materials, on the other hand, lack a periodic structure, and will not have distinct intensity peaks [32]. Such materials will rather have one or two broad intensity maxima [33]. Figure 2.10 shows the difference between the diffraction patterns of a crystalline and an amorphous material.

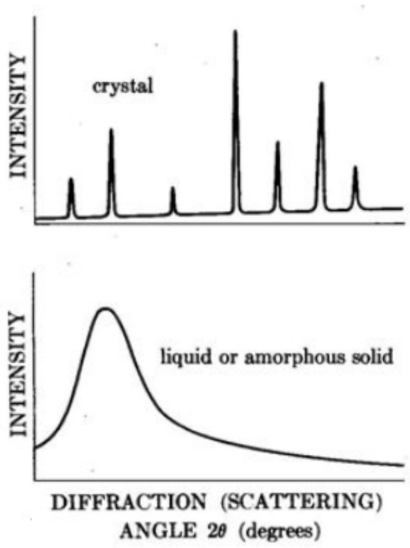

Figure 2.10: Simple illustration of the difference between the diffraction patterns of a crystalline and an amorphous material. Crystalline materials have distinct intensity peaks, while amorphous materials do not. Figure edited from [33].

2.7.2 Surface Area Measurements by the Brunauer-Emmett-Teller Method

Surface area measurements can be done by determining the amount of adsorbed gas species needed to cover a surface with a monolayer. Difficulties in doing this arise from the fact that gas species may adsorb and form multilayers or condense in small pores. Brunauer, Emmett and Teller proposed an adsorption theory as an extension of the Langmuir theory [39] that can be used to determine the surface area in cases with multilayer coverage. The theory is referred to as BET theory [40].

A BET analysis typically uses nitrogen (N_2) as adsorbate gas. The sample powder is cooled to cryogenic temperature (-195°C) by liquid N_2. At this temperature each N_2 molecule occupies an area of $0.162\,\mathrm{nm}^2$. A known amount of N_2 gas is released into the sample cell, and the pressure is controlled by creating partial vacuum. When the saturation pressure is reached, no more adsorption occurs. The sample is then removed from the N_2 atmosphere and the temperature is raised. The adsorbed gas is released and measured.

The BET theory yields the following equation:

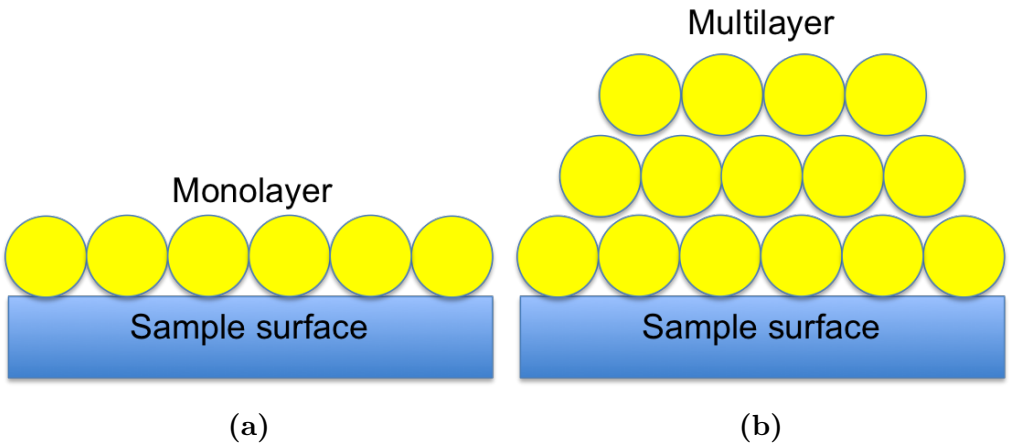

Figure 2.11: Illustration of gas species adsorbed in (a) a monolayer and (b) a multilayer. Figure based on [39].

$$\frac{P}{V_a(P_0 - P)} = \frac{1}{\chi V_0} + \frac{(\chi - 1)}{\chi V_0}\frac{P}{P_0} \tag{2.21}$$

P is the *partial pressure* of adsorbate gas at equilibrium with the surface temperature of liquid N_2. P_0 is the *saturated pressure* of the adsorbate gas. V_a is the volume of adsorbed species. V_0 is the volume of gas adsorbed to create a monolayer at standard temperature and pressure (0°C and 1 atm) [39]. χ is a dimensionless constant and is the ratio between the desorption rates of the second and first layer. P/P_0 is often referred to as relative pressure.

From equation 2.21, it can be seen that $P/[V_a(P_0 - P)]$ as a function of P/P_0 is linear. The slope of the function is $(\chi-1)/[\chi V_a]$ and the intersection point with the $P/[V_a(P_0-P)]$ -axis is at $1/[\chi V_0]$. A such representation is called a BET plot and is illustrated in figure 2.12. During BET analysis data about P/P_0 and V_a is collected and used to create a linear regression. The linear regression can then be used to find the volume of the monolayer, V_0. Furthermore, the number of gas molecules can be calculated by the ideal gas law, $N_0 = PV_0/RT$. Lastly, the surface area can be calculated since the area contribution of each adsorbed species is known, $A = N_0 A_0$ [40].

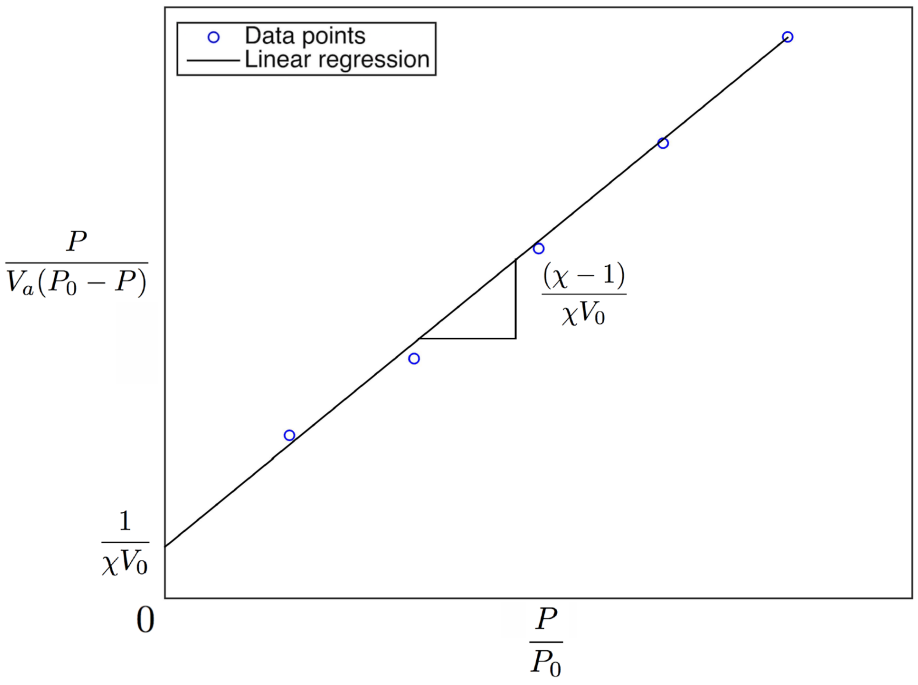

Figure 2.12: Illustration of a BET plot where $P/[V_a(P_0 - P)]$ is plotted as a function of P/P_0.

Although the BET theory can be employed on multilayer coverage, the theory has several assumptions. There is a dynamic equilibrium in which the rate of adsorption and desorption are equal in any layer. Gas species adsorb on equivalent adsorption sites in the first layer. There are no interactions between the gas species that are being adsorbed. The conditions for adsorption and desorption are the same for all the layers above the first layer. The adsorption energy for in all the layers above the first layer equals the condensation energy. Lastly, the thickness of the multilayer grows to infinite at the saturation pressure [40].

2.7.3 Electrochemical Cycling

Electrochemical cycling involves discharging and charging a battery repeatedly. This can be done in different ways. Galvanostatic cycling involves cycling a battery using a constant current, while measuring the potential. Potentiostatic cycling involves keeping a battery at a constant potential, while the current decreases [41]. How deep the battery is discharged or how much the battery is charged, can be determined by either setting potential or capacity limits [18]. Figure 2.13 shows a potential versus specific capacity curve for the same Si anodes

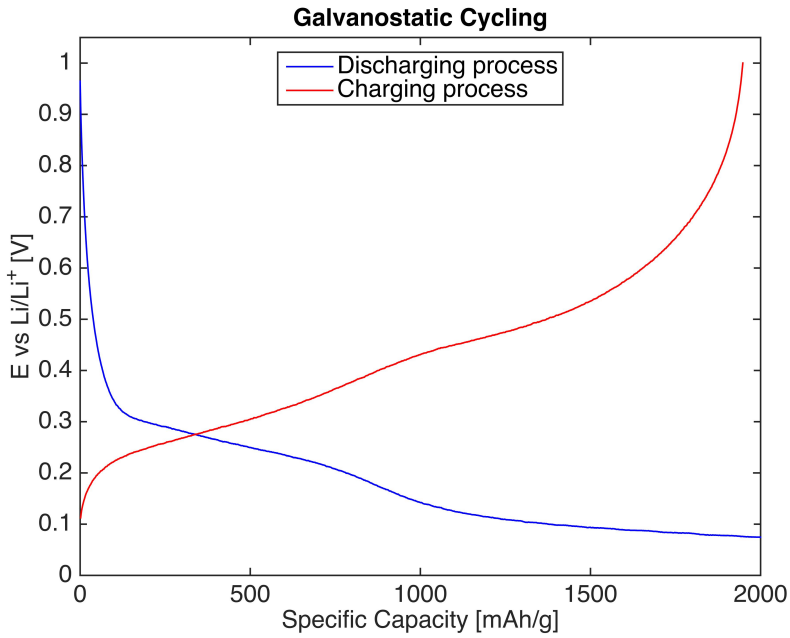

Figure 2.13: One cycle from a galvanostatic cycling test. The discharging process was capacity limited to 2000 mAh/g. The charging process was voltage limited to 1.0 V. Figure replotted from [1].

as used in this work [1]. The figure shows a cycle from a galvanostatic cycling test. The discharging process was capacity limited to 2000 mAh/g, while the charging process was voltage limited to 1.0 V.

Half-cells are frequently used in early testing stages when evaluating potential electrode materials for LIBs [18]. This is because half-cell configuration allows one to focus on a single electrode, in contrast to a full-cell configuration, where the combination of both electrodes is studied. In half-cells for LIBs, the electrode material under evaluation is the working electrode, while Li metal is the counter electrode. Using Li metal as a counter electrode provides an excess source of Li compared to full-cells. Often half-cells have excess electrolyte compared to full-cells as well. The Li and electrolyte is therefore usually not the limiting factors, and changes such as capacity fade can be linked to the electrode being evaluated. It should be noted that half-cell tests could show longer cycle life than full-cell test due to the surplus of Li and electrolyte [18]. Full-cell testing should therefore also be used to evaluate the performance of a potential electrode material without a surplus of Li or electrolyte [13].

In full-cell configuration Si electrodes act as the anode (negative electrode). Similar to the case of the Sony cell with $LiCoO_2$ and graphite explained in section 2.2, Si anodes lithiate

upon charging and delithiate upon discharging in full-cell configuration. This is opposite to half-cell configuration, where Si electrodes act as the cathode (positive electrode). This is due to the Li metal having a lower potential than Si. This means that the Si electrodes lithiate upon discharging and delithiate upon charging. To avoid confusion, the term Si electrode will be used instead of Si anode further on in this report.

For half-cell configuration the formulas for coulombic efficiency and irreversible capacity loss have to be redefined. The coulombic efficiency of a single cycle of a half-cell is the ratio between the charge and discharge capacity, or the ratio between the delithiation and lithiation capacity:

$$CE_{half-cell}(\%) = \frac{Q_{ch}}{Q_{dis}} * 100\% = \frac{Q_{del}}{Q_{lit}} * 100\% \tag{2.22}$$

Q_{ch} is the charge capacity and Q_{dis} is the discharge capacity. Q_{del} is the delithiation capacity and Q_{lit} is the lithiation capacity. Furthermore, the irreversible capacity loss and cumulative irreversible capacity loss for a half-cell [12]:

$$ICL_{half-cell} = Q_{dis} - Q_{ch} = Q_{lit} - Q_{del} \tag{2.23}$$

$$CICL_{half-cell} = \sum_{n} (Q_{dis} - Q_{ch})_i = \sum_{n} (Q_{lit} - Q_{del})_i \tag{2.24}$$

2.7.4 Differential Capacity Analysis

As mentioned, lithiation of Si happens in both two-phase and one-phase reactions. In voltage versus time or capacity plots, such reactions will appear as voltage plateaus and sloping voltage curves, respectively. Differential capacity plots show dQ/dE versus E and help identify the voltage where the reactions occur. A differential capacity curve for one cycle is shown in figure 2.14. The discharging process has $dQ/dE < 0$ because $dE < 0$, while the charging process has $dQ/dE > 0$ because $dE > 0$.

The voltage plateaus can be identified as peaks in the differential capacity plot. The flatness of the voltage plateau is indicated by the height of the peak. Flat plateaus give a low dE/dQ value and a high $dQ/dE = (dE/dQ)^{-1}$ value. The area between the dQ/dE curve and $E = 0$ is a measure of the capacity of the plateau [18].

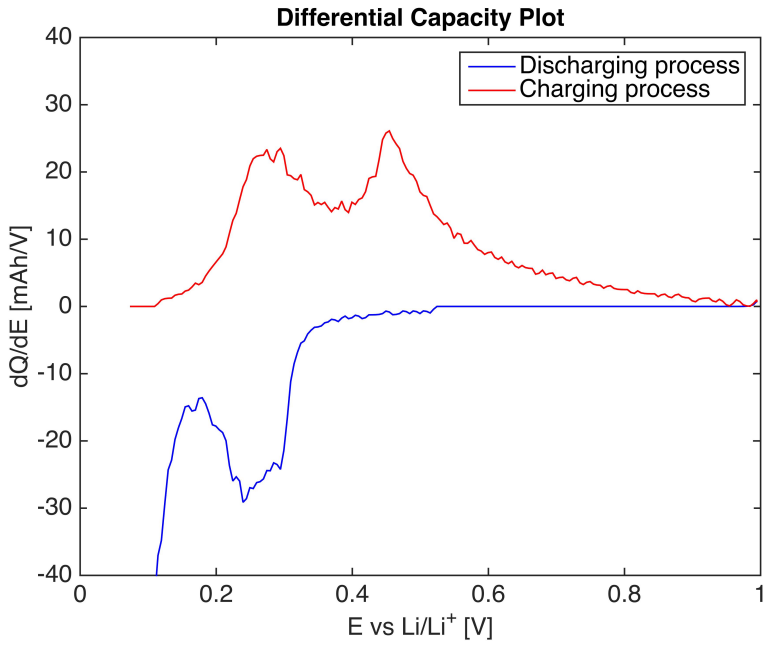

Figure 2.14: Differential capacity plot for the cycle in figure 2.13. The part of the curve where $dQ/dE < 0$ is the discharging process, while $dQ/dE > 0$ is the charging process part of the curve.

2.7.5 Electrochemical Impedance Spectroscopy

Electrochemical impedance spectroscopy (EIS) is a technique in which a system is subject to a small sinusoidal perturbation by either oscillating the current or potential over a range of frequencies, while the corresponding potential or current response is measured. The frequencies used are between 100 kHz and 1 mHz, and the oscillation amplitude is small. In galvanostatic EIS (GEIS) measurements, a direct current oscillates and the potential response is measured. In potentiostatic EIS (PEIS) measurements, the potential oscillates about 10 mV and the current response is measured. If the perturbation is small, the potential-current relationship will be linear and the other parameter will have a sinusoidal response at the same frequency but with a phase shift [42]. For a PEIS experiment, the potential and current response are given by:

$$E(t) = E_0 sin(\omega t) \tag{2.25}$$

$$I(t) = I_0 sin(\omega t + \varphi) \tag{2.26}$$

E_0 and I_0 are the amplitudes of the oscillating potential and current, respectively. t is time.

ω is the angular frequency and defined as $\omega = 2\pi f$, where f is frequency. φ is the phase shift.

The impedance, Z, is defined as [43]:

$$Z = \frac{\tilde{E}(j\omega)}{\tilde{I}(j\omega)} \tag{2.27}$$

$\tilde{E}$ and $\tilde{I}$ are the Laplace transform of the potential and current, respectively. The impedance can be represented as a complex number with a real part, Z_{Re}, and an imaginary part, Z_{Im}:

$$Z = Z_{Re} + jZ_{Im} \tag{2.28}$$

The results from an EIS experiment are often represented through a Nyquist plot and Bode plot. Nyquist plots show $-Z_{Im}$ versus Z_{Re}, while Bode plots show $-Z_{Im}$ versus $log(f)$ [42].

This technique is useful to evaluate mass transport and charge transfer processes in batteries [44]. Some processes respond faster to perturbations than others. Processes can be studied by applying perturbations over a range of frequencies. Electrolyte resistances are often determined at high frequencies of 1 MHz to 100 kHz. Film resistance for Li-ion migration through the SEI layer and impedance of substrate-electrode interface are often determined at frequencies 1 kHz to 10 Hz. Charge transfer resistance at phase boundaries are often determined at frequencies 10 Hz to 0.1 Hz. Lastly, solid state diffusion is often determined below 40 mHz [44].

Chapter 3

Experimental

3.1 Overview

Four Si powders from different suppliers were characterized by XRD and BET. Three of these Si powders were used to make Si electrodes. The Si electrodes were assembled into coin cells or PAT-cells and electrochemically tested. Prefabricated Si-graphite composite electrodes were used as a reference point for the electrochemical tests in this project. The experimental work can be divided into these five parts:

1. Characterizing Si powders by XRD and BET
2. Preparing Si electrodes by tape casting
3. Assembling Si electrodes into coin cells in half-cell configuration
4. Electrochemical testing of coin cells
5. Electrochemical impedance spectroscopy of PAT-cells in half-cell configuration

3.2 Introduction to the Silicon Powders

The four different types of Si powders and the prefabricated Si-graphite electrodes will be presented before describing the experimental work done in this project. The available information for the different Si powders varies. Therefore, the information provided in this section will vary between the different Si powders.

3.2.1 Silgrain® e-Si 400

The first Si powder used in this project was Silgrain® e-Si 400 produced by Elkem. Silgrain® e-Si is a collection of commercialized Si powders made for Si-based anodes in rechargeable batteries. Elkem states that they deliver different qualities of the Silgrain® e-Si powders to fit different processes and technologies [45].

Earlier work done by Kaland (2017) [12] has indicated that the Silgrain® e-Si 400 has a fairly monodisperse particle size distribution centered at 3.4 µm and a median particle size of 2.81 µm by laser diffraction. The supplier of this powder has informed about the purity, and this information is summarized in table 3.1.

Table 3.1: Typical weight percentages of the elements present in Silgrain® e-Si 400 [46].

Elements	Si [wt%]	Fe [wt%]	Al [wt%]	Ca [wt%]	Ti [wt%]	P [ppmw]	B [ppmw]
	99.8	0.04	0.09	0.013	0.001	25	30

3.2.2 Sigma-Aldrich Nano-Si

The second Si powder used in this project was Si nanopowder produced by Sigma-Aldrich (product number 795585). The particle size of this Si powder has been estimated, by Sigma-Aldrich, to be less than 100 nm by using the BET method. The Si powder also has less than 3% oxygen passivation, meaning that less than 3% of the surface is terminated by oxygen [47]. The supplier of this powder has informed about the purity of the Si powder is 99% based on trace metals analysis, and is summarized in table 3.2. The purity of the Si powder seems to be approximately 99.5% Si because all the impurities in table 3.2 add up to approximately 0.5%.

Table 3.2: Impurities in Sigma-Aldrich nano-Si. The analysis was done based on trace metals analysis [48].

Elements	**Amount** [%]
Al	0.074
As	0.00058
B	0.00058
Ba	0.00008
Ca	0.006
Co	0.00029
Cr	0.0032
Cu	0.00074
Fe	0.395
K	0.0037
Li	0.00012
Mg	0.0022
Mn	0.0075
Na	0.0033
Ni	0.0045
Sr	0.00014
W	0.0003
Zr	0.00072

3.2.3 99.5% Si Resitec

The third Si powder used in this project was 99.5% Si Resitec. 99.5% Si Resitec is kerf produced from the solar grade Si blocks being sawed by blades.

The supplier of this powder has informed about the purity and the particle size distribution [49]. The purity of the Si powder was measured by x-ray fluorescence (XRF), and is summarized in table 3.3. The particle size distribution was measured by laser diffraction, and is summarized in table 3.4. 10% of the particles have a particle size below D10, 50% of the particles have a particle size below D50 and 90% of the particles have a particle size below D90.

Table 3.3: Weight percentages of the elements present in 99.5% Si Resitec. The analysis was done by x-ray fluorescence (XRF) at Degerfors Laboratorium AB [49].

Elements	**Weight percentage [%]**
Si	>99.7
Fe	0.04
Al	0.08
Ca	0.006
Cr	<0.001
Cu	<0.01
Ti	<0.003

Table 3.4: Particle size distribution of 99.5% Si Resitec. The analysis was done by laser diffraction at Resitec [49].

	Particle Size [µm]
D10	1.0
D50	4.5
D90	15

3.2.4 Si Kerf

The fourth Si powder used in this project was a Si kerf from a slurry-based sawing process. The details of the processing of this Si kerf have not been provided. The supplier has informed that this Si kerf has been purified to remove the SiC fraction with particle size above ∼4.5 µm.

The particle size of the Si kerf is between ∼0.25 µm to ∼4.5 µm with the largest fraction being ∼1 µm [49].

3.2.5 BEC 01 Electrodes

The prefabricated Si electrodes used in this project were made by Institute for Energy Technology (IFE). These will further be referred to as BEC 01 electrodes. These electrodes were made of Silgrain® e-Si 400, graphite (K56L), carbon black (C 65), binder (carboxymethyl cellulose; CMC), buffer with citric acid ($C_6H_8O_7$) and potassium hydroxide (KOH). The weight percentage of each component is given in table 3.5. The Silgrain® e-Si 400 powder was ball milled for five minutes. The components were mixed into a slurry by a planetary centrifugal mixer (Thinky mixer). The slurry was screen printed onto dendritic copper foil (Cu).

Table 3.5: Weight percentages of the materials used in BEC 01 electrodes.

Material	**Weight Percentage** [%]
Silicon	52.20
Graphite	8.70
Carbon black	13.06
Carboxymethyl cellulose	13.05
Citric acid, potassium hydroxide and more	12.99

3.3 Characterization of Silicon Powders

The Si powders were characterized by XRD and Brunauer Emmett Teller (BET) as received from the suppliers. These tests were done to determine the crystallinity and surface area of the different Si powders.

3.3.1 XRD

A Bruker D8 Advance Da Vinci X-Ray Diffractometer was used for the XRD analysis. The machine has Bragg-Brentano geometry and uses Cu K_α radiation. The samples were analyzed at Bragg angles 10-75° with a 0.2° fixed slit opening and a 0.0134° step size. Data analysis

was done using software DIFFRAC.EVA V4.2.1. The only refinement used was stripping of $K_{\alpha 2}$.

3.3.2 BET

The Si powders were degassed at 80°C overnight and flushed with nitrogen gas (N_2) before the BET analysis. The degassing and flushing was done using a VacPrep 061 Sample Degas System. The BET analysis was done using a Tristar 3000 Surface Area and Porosity Analyzer and Tristar 3000 V6.05 software.

3.4 Preparing Silicon Electrodes

The Si electrodes were made by tape casting slurry onto a current collector, as illustrated in figure 3.1. Silgrain® e-Si 400, Sigma-Aldrich nano-Si and 99.5% Si Resitec were used to make Si electrodes. Preparing the Si electrodes consisted of four steps: Making the buffer solution; making the binder solution; mixing the slurry; tape casting the slurry.

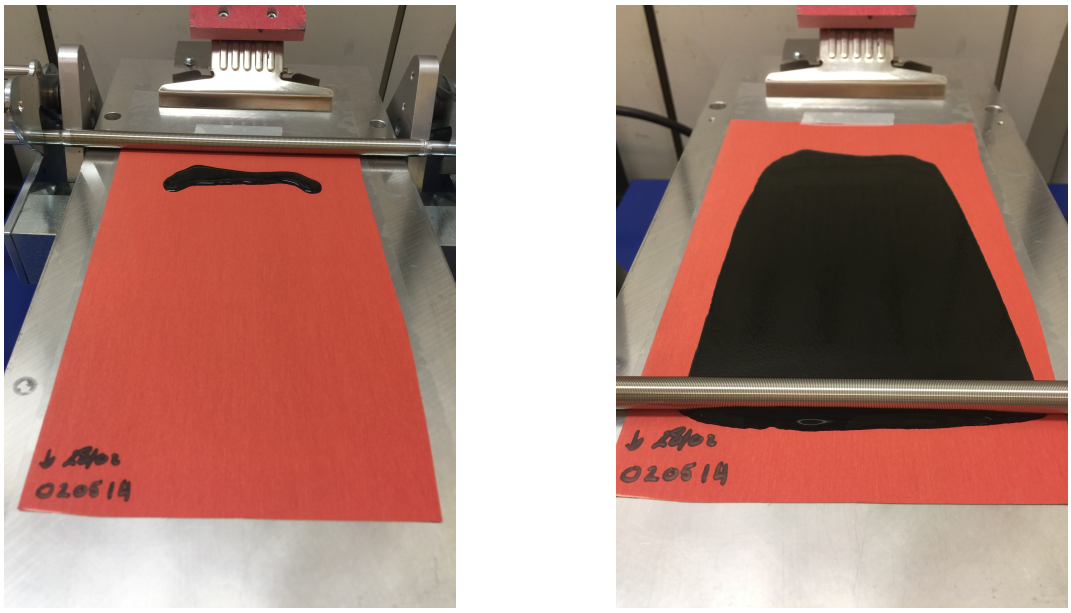

(a) **(b)**

Figure 3.1: Photographs illustrates tape casting. (a) shows slurry distributed onto the current collector (dendritic Cu foil) prior to tape casting. (b) shows the slurry directly after tape casting.

The slurries consisted of an active material, a conductive additive and a binder material in a buffer solution. Si powder was used as active material. Carbon black (CB; Imerys, C-nergy Super C65 conductive carbon black) was used as conductive additive. Sodium carboxymethyl cellulose (Na−CMC; Sigma-Aldrich, average MW∼90,000) was used as binder material. The buffer solution consisted of deionized water, citric acid ($C_6H_8O_7$; Sigma-Aldrich, 99%) and potassium hydroxide (KOH; Sigma-Aldrich, reagent grade, 90% flakes). Dendritic copper foil (Cu; Schlenk Metallfolien, ETP Copper LTA-Quality, Cu-Treatment on one side 0.018 x 300 mm) was used as current collector. The electrodes were composed of 60 wt% active material, 25 wt% conductive additive and 15 wt% binder material. The desired Si loading of the electrodes was 0.4-0.5 mg/cm^2.

3.4.1 Buffer and Binder Solutions

The buffer solution was made by adding 4.544 g citric acid and 0.519 g KOH to 250 mL deionized water. The solution was stirred until it became a homogeneous mixture by visible inspection.

Na-CMC and buffer solution were further mixed into a binder solution. The weight ratio of Na-CMC to buffer solution was 1:23. The binder solution was magnetically stirred at 500 rpm and 70°C for 3 hours until it became a homogeneous mixture by visible inspection.

3.4.2 Mixing Slurries and Tape Casting

The procedures for mixing slurries and tape casting the Si electrodes were developed using a trial-and-error strategy. The procedures were different for each of the three Si powders in order to achieve homogeneous slurries and desired Si loading. The processes of developing the procedures for Silgrain® e-Si 400 and 99.5% Si Resitec are described in appendix A.

The slurries were made by mixing Si powder, CB, binder solution and buffer solution. A scale with a resolution of 0.1 mg was used to weigh the the slurry components. A shaker mill (Retsch MM 400) and a dispersing instrument (IKA Ultra-Turrax T 25 digital) were used to mix the slurries. The slurries were distributed and tape casted onto wrinkle free Cu foil using a tape caster (RK K Control Coater) with a meterbars (RK Print Coat Instruments U.K.; K bar). Meterbars with tread depths "2", "3" and "4" were used, where "2" was the finest tread depth. The tape casts were dried at least overnight at 70°C in an oven (Termaks), followed by at least five hours at 120 °C in a vacuum oven (Binder, VD 23). After the casts

had dried, three Si electrode discs were cut out from each cast and weighed. The following sections describe the mixing and tape casting procedures used for each of the three Si powders in more details.

Silgrain® e-Si 400

The slurry mixing for Silgrain® e-Si 400 was done by the following procedure: 0.300 g of Si powder and 0.125 g of CB were added to a steel jar and mixed in a shaker mill for 5 minutes at 25 Hz. Binder solution equivalent to 0.075 g Na-CMC, 1.725 g binder solution, and 0.525 g buffer solution was added before being further mixed in a shaker mill for 60 minutes at 25 Hz. The total weight ratio between Na-CMC and buffer solution was 1:30. The slurry was tape casted onto Cu foil using a meterbar with tread depth "4" and with the tape casting speed set to "1".

Sigma-Aldrich Nano-Si

The slurry mixing for Sigma-Aldrich nano-Si was done by the following procedure: 0.900 g of Si powder and 1.275 g buffer solution was added to a glass jar. The glass jar was shaken in order to wet the Si powder. 0.375 g of CB and binder solution equivalent of 0.225 g Na-CMC were added to the glass jar before being further mixed in a shaker mill set to 17 Hz for 60 minutes. The content of the glass jar was afterwards mixed by a dispersing instrument for 3 minutes at 12000 rpm followed by 3 minutes at 9000 rpm. The total weight ratio between Na-CMC and buffer solution was 1:40. The slurry was tape casted onto Cu foil using a meterbar with tread depth "4" and with tape casting speed set to just below "2".

99.5% Si Resitec

The slurry mixing for 99.5% Si Resitec was done by the following procedure: 0.300 g of Si powder and 0.125 g of CB were added to a steel jar and mixed in a shaker mill for 5 minutes at 25 Hz. Binder solution equivalent to 0.075 g Na-CMC, 1.725 g binder solution, and 0.675 g buffer solution was added before being further mixed in a shaker mill for 75 minutes at 25 Hz. The total weight ratio between Na-CMC and buffer solution was 1:32. The slurry was tape casted onto Cu foil using a meterbar with tread depth "3" and with tape casting speed set to "1".

The compositions of the Si electrodes used for further electrochemical testing are stated in table 3.6 with the Si loadings of the three Si electrode discs. The buffer components, $C_6H_8O_7$ and KOH, do not evaporate during drying [50].

3.5 Assembling Coin Cells

Si electrodes were assembled into coin cells with half-cell configuration. The tape casted electrodes were cut into Si electrode discs with a 16.0 mm diameter. The Si electrodes were weighed with a 0.01 mg resolution and the weight of the current collector was subtracted.

The coin cells were assembled in a glove box with argon (Ar) atmosphere (M Braun Labmaster SP, <0.1 ppm H_2O and <0.1 ppm O_2). The Si electrode discs were transferred to the glove box via an antechamber, which was evacuated for 3x10 minutes with refilling of Ar atmosphere from inside the glove box between each evacuation.

The parts of the coin cell were stacked in the following order from bottom to top, as illustrated in figure 3.2: Coin cell bottom cap; Si electrode; 20 µL electrolyte; separator; 20 µL electrolyte; coin cell gasket; Li metal disc; spacer; coin cell top cap. The parts were centered and the coin cells were punched together using a crimping machine (Hohsen Corporation). The coin cells were held at rest for at least 24 hours before being electrochemically tested.

The coins cell cases were 2016 cases (Hohsen Corporation). The spacers used were either 0.3 mm or 0.5 mm thick depending on the thickness of the Si electrode. Selection of appropriate spacer thickness was done to ensure the best connection between the coin cell electrodes and case, and to prevent coin cell parts from moving after assembly. The separators used were 25 µm thick (17.0 mm diameter; Celgard Li-ion separator, 2325). The Li metal discs had a 14.0 mm diameter. The electrolyte used was 1.0 M lithium hexafluorophosphate in equal volume parts of ethylene carbonate and diethyl carbonate (Sigma-Aldrich, 1.0 M $LiPF_6$ in EC/DEC=50/50 (v/v)).

Table 3.6: Composition of the casts that were used for electrochemical testing.

Type of Si powder	**Si [wt%]**	**CB [wt%]**	**Na-CMC [wt%]**	**$C_6H_8O_7$ and KOH [wt%]**	**Si loading [mg/cm^2]**
Silgrain® e-Si 400	55.1	23.1	13.8	8.0	0.52 ± 0.01
Sigma-Aldrich nano-Si	53.7	22.4	13.5	10.4	0.41 ± 0.01
99.5% Si Resitec	54.7	22.9	13.9	8.6	0.35 ± 0.01

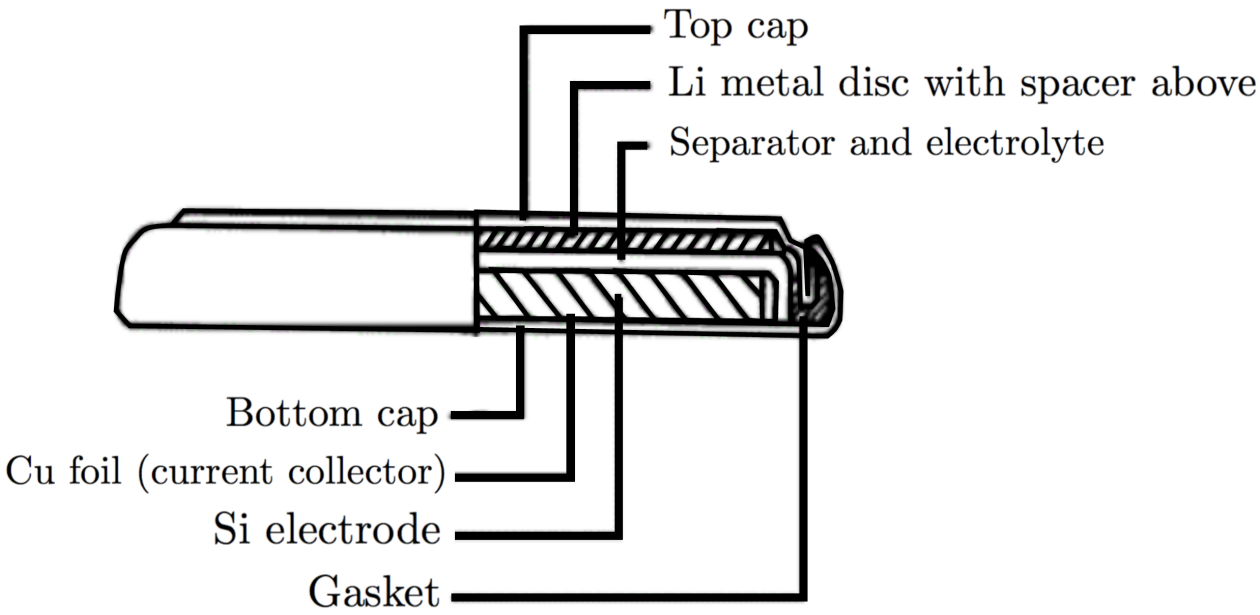

Figure 3.2: Illustration of the layering order inside of the coin cells. Figure edited from [51].

3.6 Electrochemical Testing of Coin Cells

The coin cells were galvanostatic cycled with a Lanhe CT2001A-Battery Testing System with software LAND Battery Testing System - Data Processing Software V5.9K. All the coin cells that were electrochemical tested, went first through a precycling program described in table 3.7. The coin cells were then either tested through a rate test program or a 50 cycle test program. The rate test is described in table 3.8. In the 50 cycle test program, the coin cells were lithiated to 0.05 V and delithiated to 1.0 V at 0.5C. No potential steps were taken for neither test program. The C-rates used in all the tests were based on Si having a theoretical capacity of 3600 mAh/g.

Table 3.7: Precycling program done prior to either the rate test or the 50 cycle test.

Cycle	Action
1	Lithiated to 500 mAh/g(Si) and delithiated to 1.0 V at 0.05C
2	Lithiated to 1000 mAh/g(Si) and delithiated to 1.0 V at 0.05C
3	Lithiated to 1500 mAh/g(Si) and delithiated to 1.0 V at 0.05C
4	Lithiated to 2000 mAh/g(Si) and delithiated to 1.0 V at 0.05C

Table 3.8: Rate test program.

Step	Number of cycles	Action
1	5	Lithiated to 0.05 V and delithiated to 1.0 V at 0.1C
2	5	Lithiated to 0.05 V and delithiated to 1.0 V at 0.2C
3	5	Lithiated to 0.05 V and delithiated to 1.0 V at 0.5C
4	5	Lithiated to 0.05 V and delithiated to 1.0 V at 1.0C
5	5	Lithiated to 0.05 V and delithiated to 1.0 V at 0.1C

3.7 Electrochemical Impedance Spectroscopy

Si electrodes were assembled into PAT-cells (EL-CELL®) with half-cell configuration and electrochemically tested. Figure 3.3 provides a schematic illustration of the parts in a PAT-cell. The PAT-cells had an insulation sleeve with a Li-reference electrode ring and 0.26 mm thick glass fiber separator (EL-CELL®) (figure 3.4), allowing for three-electrode tests. A Si electrode disk (16.0 mm diameter) was used as working electrode, while a Li metal disc

(14.0 mm diameter) was used as counter electrode. 1.0 M $LiPF_6$ in EC/DEC=50/50 (Sigma-Aldrich) was used as electrolyte. Stainless steel upper and lower plungers were used.

The PAT-cells were assembled in a glove box. The Si electrode was placed in the lower electrode position with the active layer facing the glass fiber separator. The lower plunger was inserted and the insulation sleeve was placed in the cell base. 80 µL electrolyte was dispensed evenly on top of the separator. The Li metal disc was placed in the upper electrode position and the upper plunger was inserted. The screw cap with sealing ring was attached and tightened. The PAT-cells were held at rest for at least 24 hours before being electrochemically tested.

The PAT-cells were tested in a BioLogic VMP-300 with EC-Lab V11.12 software. The PAT-cells were cycled in accordance with the precycling program and 50 cycle test program described in section 3.6, but with a few modifications due to the impedance measurements. Impedance measurements were conducted at the end of the discharging processes for each precycle step and cycles 10, 30 and 50 of the 50 cycle test program.

The test program used for impedance measurements had a combination of galvanostatic and potentiostatic cycling. The PAT-cells were galvanostatically discharged (lithiated). Before the impedance measurements, the PAT-cells were kept at the end potential until the current was reduced to 10% of the initial current value and held at rest for 10 seconds. In the cycles without impedance measurements, the end potential was kept until the current was reduced to 50% of the initial current value. The PAT-cells were galvanostatically charged (delithiated), and held at the end potential until the current was reduced to 50% of the initial current value. The capacity limits, potential limits and C-rates were the same as described in section 3.6.

The impedance measurements used the frequency range 200 kHz to 100 mHz and an amplitude of 5.0 mV.

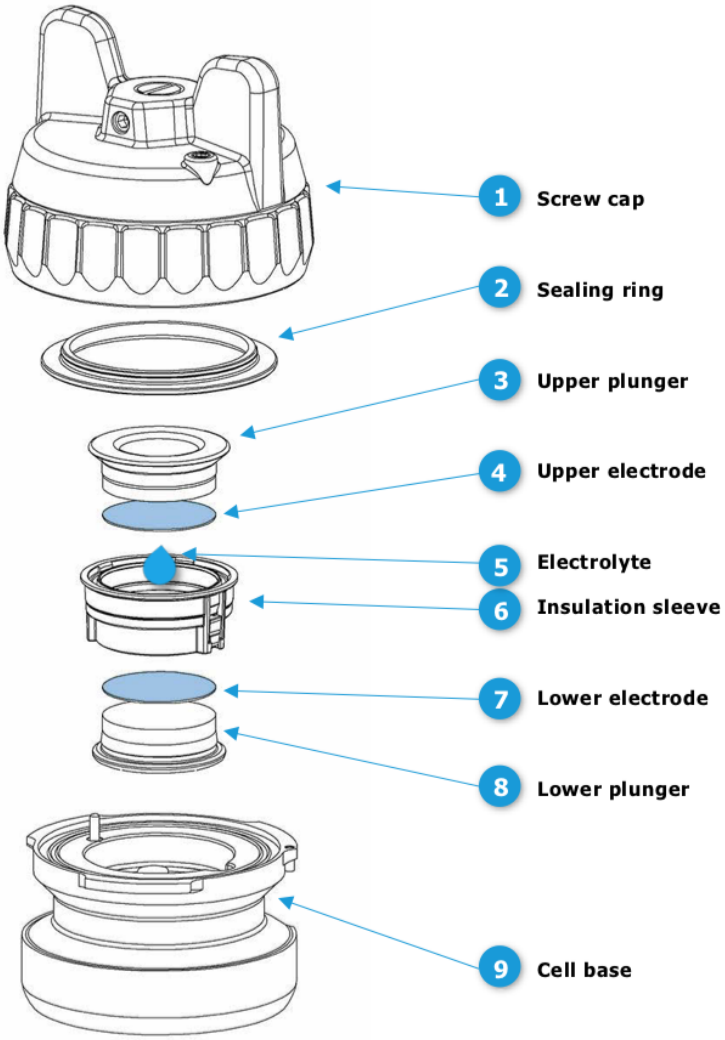

Figure 3.3: Schematic illustration of the build up of a PAT-cell used for EIS. Figure from [52].

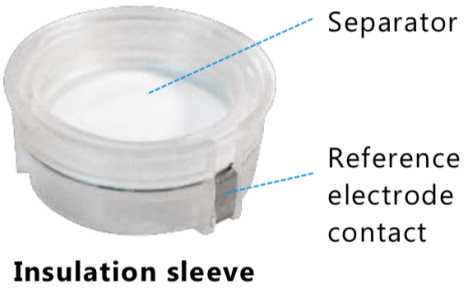

Figure 3.4: Insulation sleeve with Li-reference electrode ring and separator used in the PAT-cells. Figure from [53].

Chapter 4

Results

4.1 Crystallinity of Silicon Powders

Figures 4.1 to 4.4 shows the diffraction patterns of the four different Si powders used in this project. The diffraction patterns for Silgrain® e-Si 400 (figure 4.1), Sigma-Aldrich nano-Si (figure 4.2) and 99.5% Si Resitec (figure 4.3) show four distinct intensity peaks at approximately 28.4°, 47.3°, 56.1° and 69.1°. The intensity peaks are reduced towards higher diffraction angles. The exact intensity peak positions with intensity values are given in appendix B tables B.1, B.2 and B.3. The positions of the intensity peaks in these diffraction patterns correspond well to those of Si from the International Centre for Diffraction Data (ICDD) database. See appendix C table C.1 for the database positions for Si peaks.

The diffraction pattern of Si kerf (figure 4.4) shows 11 distinct intensity peaks. Four of the intensity peaks are at approximately the same positions as the three other Si powders. Seven more intensity peaks are at approximately 34.1°, 35.6°, 38.2°, 41.4°, 60.0°, 65.6° and 71.8°. The exact intensity peak positions with intensity values are given in appendix B in table B.4. The positions of the intensity peaks in this diffraction pattern correspond well to those of Si and SiC from the International Centre for Diffraction Data (ICDD) database. See appendix C table C.2 for the database positions for SiC peaks.

The crystallite sizes for the Si powders were calculated by using Scherrer's formula (equation 2.20). Scherrer's formula was applied to the intensity peaks at 28.4°, 47.3°, 56.1° and 69.1° in the diffraction patterns, and averages were calculated. The average crystallite sizes and standard deviations for all four Si powders are given in table 4.1. It should be noted that the

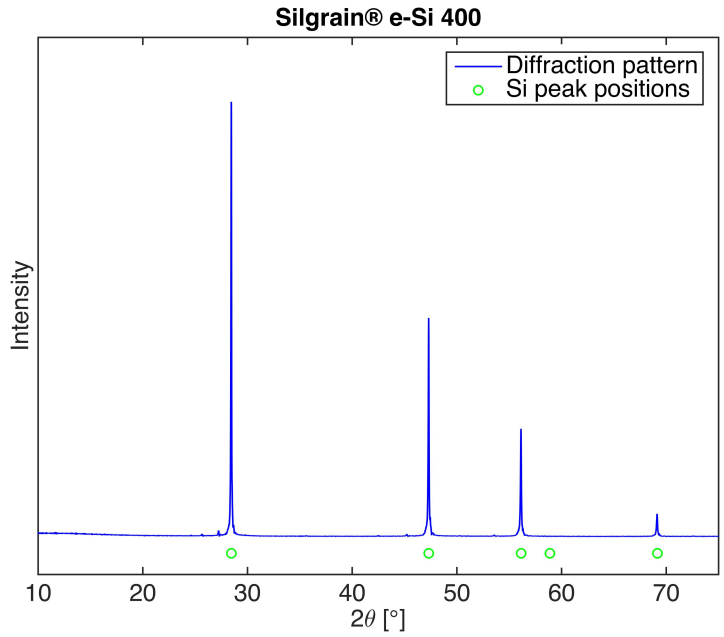

Figure 4.1: Diffraction pattern of Silgrain® e-Si 400 as received. The diffraction pattern has been stripped of $K_{\alpha 2}$, but background has not been subtracted. The Si peak positions from the ICDD database are marked [54].

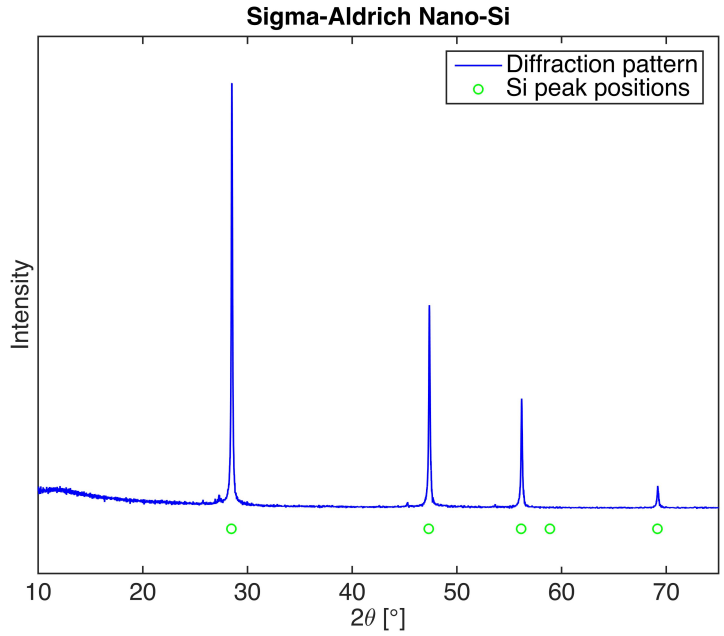

Figure 4.2: Diffraction pattern of Sigma-Aldrich nano-Si as received. The diffraction pattern has been stripped of $K_{\alpha 2}$, but background has not been subtracted. The Si peak positions from the ICDD database are marked [54].

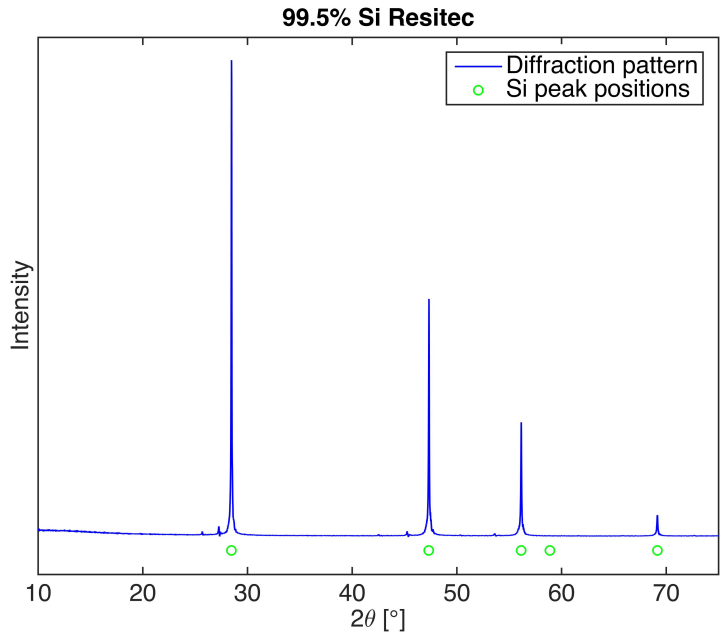

Figure 4.3: Diffraction pattern of 99.5% Si Resitec as received. The diffraction pattern has been stripped of $K_{\alpha 2}$, but background has not been subtracted. The Si peak positions from the ICDD database are marked [54].

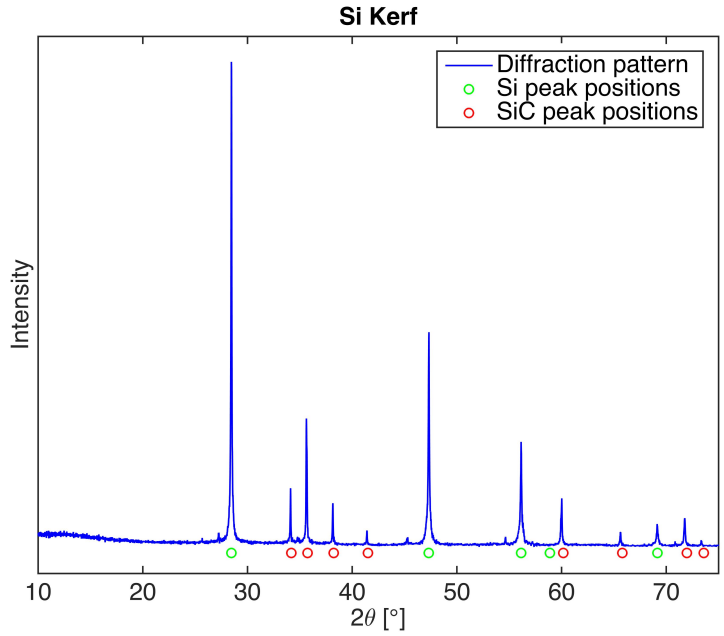

Figure 4.4: Diffraction pattern of Si kerf as received. The diffraction pattern has been stripped of $K_{\alpha 2}$, but background has not been subtracted. The Si and SiC peak positions from the ICDD database are marked [54].

crystallite size calculations for Si kerf are only based on the intensity peaks at 28.4°, 47.3°, 56.1° and 69.1°, even though its diffraction pattern showed eleven intensity peaks.

The four Si powders show different average crystallite sizes. 99.5% Si Resitec has about twice as large average crystallite sizes compared to Sigma-Aldrich nano-Si. All of the Si powders have relative high standard deviations. The lowest standard deviation being approximately 17% for both 99.5% Si Resitec and Si kerf.

Only Silgrain® e-Si 400, Sigma-Aldrich nano-Si and 99.5% Si Resitec were further processed into Si electrodes since the Si kerf contained significant amounts of SiC, which is inactive to reactions with Li-ions.

Table 4.1: The average crystallite sizes of the Si powders obtained by applying Scherrer's formula to the diffraction patterns in figures 4.1 to 4.4.

Si powder	**Crystallite size [Å]**	**Particle sizes [μm]**
Silgrain® e-Si 400	1616 ± 534	~ 2.81
Sigma-Aldrich nano-Si	908 ± 208	< 0.1
99.5% Si Resitec	1876 ± 320	~ 4.5
Si kerf	1409 ± 243	~ 1

4.2 Surface Area of Silicon Powders

The results of the BET surface area measurements are summarized in table 4.2. There were clear differences between the four Si powders. Silgrain® e-Si 400 had the lowest surface area with $4.2\,m^2/g$. 99.5% Si Resitec had about twice the surface area at $8.1\,m^2/g$. Sigma-Aldrich nano-Si and Si kerf had considerably higher surface areas with $28.6\,m^2/g$ and $28.8\,m^2/g$, respectively. The BET plots can be found in appendix D.

Table 4.2: Summary of the results from the BET surface area analysis of the four Si powders used in this project.

Type of Si powder	**BET surface area [m^2/g]**
Silgrain® e-Si 400	4.19 ± 0.08
Sigma-Aldrich nano-Si	28.63 ± 0.42
99.5% Si Resitec	8.13 ± 0.19
Si kerf	28.80 ± 0.16

4.3 Electrochemical Testing of Coin Cells

The 50 cycle test results and rate test results will be presented in this section. The results from each of the three Si powders and the prefabricated electrodes will be presented individually, and the comparison will take place in the discussion chapter. The results presented in this section are the average values of three coin cells together with standard deviation (as error bars) if not otherwise stated. Half-cell configuration has been used in the experimental work. To avoid confusion, the following terminology will be used:

- The term loading refers to the Si loading.
- The terms lithiation and delithiation will be used instead of discharge and charge, respectively.
- The reported capacities are the delithiation capacities if not otherwise stated. Furthermore, the delithiation capacities are presented per weight Si on the electrodes. However the differential capacity plots are presented with absolute capacities.
- All potentials reported are versus Li/Li^+.
- The half-cell configuration definitions of coulombic efficiency (equation 2.22), irreversible capacity loss (equation 2.23) and cumulative irreversible capacity loss (equation 2.24) will be used.

4.3.1 Precycles

Silgrain® e-Si 400

Table 4.3 summarizes the coulombic efficiencies and irreversible capacity losses for each step of the precycling program for coin cells with Silgrain® e-Si 400. These are average values obtained from six coin cells with Si loading 0.52 ± 0.01 mg/cm^2. The coulombic efficiency increases for each step of the precycling program, and irreversible capacity loss decreases.

Table 4.3: Coulombic efficiencies (CE) and irrreversible capacity losses (ICL) for six coin cells with Silgrain® e-Si 400 during the precycling program. The Si loading was 0.52 ± 0.01 mg/cm^2.

Precycling step	CE [%]	ICL [mAh/g]
500 mAh/g	60.54 ± 2.45	197.4 ± 12.6
1000 mAh/g	91.02 ± 0.77	89.8 ± 7.7
1500 mAh/g	95.89 ± 0.22	61.7 ± 3.4
2000 mAh/g	97.18 ± 0.16	56.3 ± 3.1

Figure 4.5 is the differential capacity plot for each step of the precycling program for one coin cell with Silgrain® e-Si 400. The first step (500 mAh/g) shows a peak at 0.07 V during the lithiation process. The following delithiation process shows two peaks at 0.32 V and 0.49 V. The second step (1000 mAh/g) shows two peaks during the lithiation process at 0.22 V and 0.08 V. The following delithiation process shows two peaks at 0.30 V and 0.48 V. The third and fourth steps (1500 mAh/g and 2000 mAh/g) show two peaks during the lithiation process at 0.24 V and 0.09 V. There is also a small notch to the right of the 0.09 V peak. The delithiation process of the third step shows two peaks at 0.29 V and 0.47 V. In the delithiation process of the fourth step, the peaks are at 0.27 V and 0.47 V.

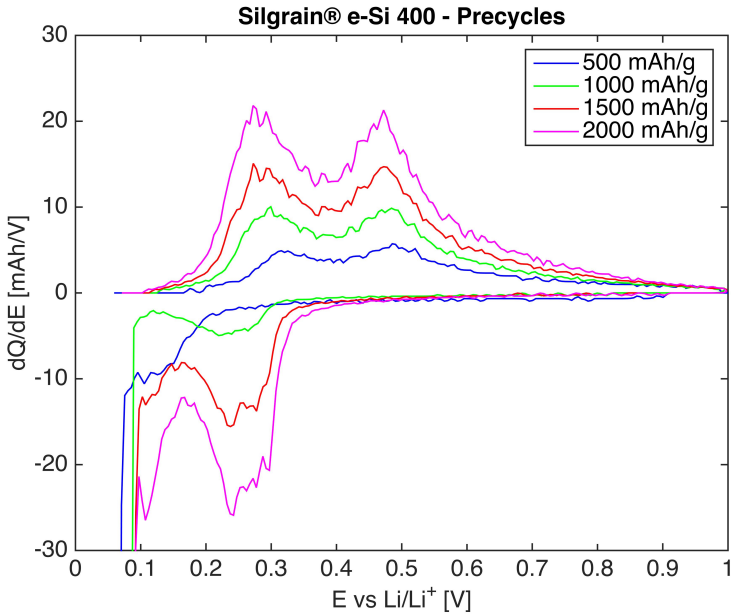

Figure 4.5: Differential capacity plot of the precycles for a selected coin cell with Silgrain® e-Si 400. The Si loading was 0.51 mg/cm^2.

Sigma-Aldrich Nano-Si

Table 4.4 summarizes the coulombic efficiencies and irreversible capacity losses for each step of the precycling program for coin cells with Sigma-Aldrich nano-Si. These are average values obtained from six coin cells with Si loading 0.40 ± 0.01 mg/cm^2. The coulombic efficiency increases for each step of the precycling program, and irreversible capacity loss decreases.

Table 4.4: Coulombic efficiencies (CE) and irrreversible capacity losses (ICL) for six coin cells with Sigma-Aldrich nano-Si during the precycling program. The Si loading was 0.40 ± 0.01 mg/cm^2.

Precycling step	CE [%]	ICL [mAh/g]
500 mAh/g	39.37 ± 4.63	303.2 ± 23.3
1000 mAh/g	86.69 ± 0.67	133.0 ± 6.7
1500 mAh/g	95.65 ± 0.39	65.1 ± 5.9
2000 mAh/g	96.85 ± 0.18	63.0 ± 3.5

Figure 4.6 is the differential capacity plot for each step of the precycling program for one coin cell with Sigma-Aldrich nano-Si. The first step (500 mAh/g) shows a peak at 0.06 V during the lithiation process. The following delithiation process shows either one broad peak or two peaks at 0.30 V and 0.48 V. The second step (1000 mAh/g) shows two peaks during the lithiation process at 0.22 V and 0.08 V. The following delithiation process shows two peaks at 0.29 V and 0.48 V. The third and fourth steps (1500 mAh/g and 2000 mAh/g) show two peaks during the lithiation process at 0.23 V and 0.09 V. There is also a small notch to the right of the 0.09 V peak. The delithiation process of the step third shows two peaks at 0.29 V and 0.48 V. In the delithiation process of the fourth step, the peaks are at 0.28 V and 0.49 V.

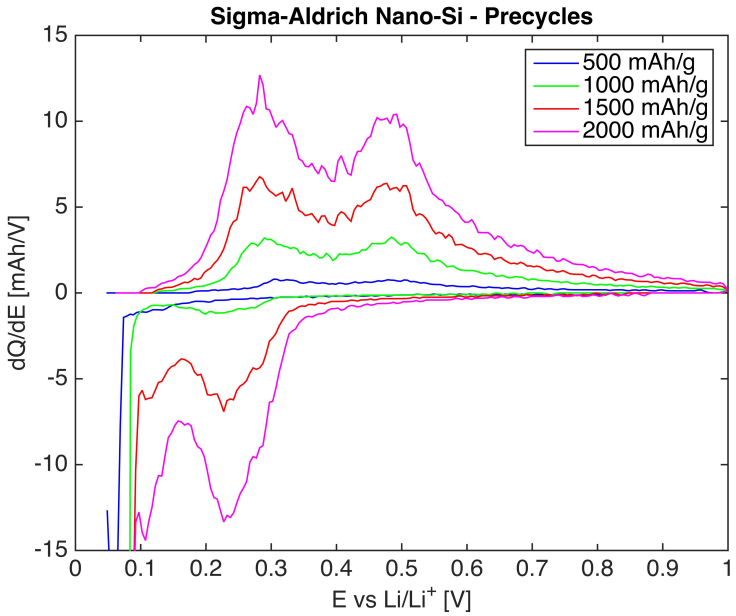

Figure 4.6: Differential capacity plot of the precycles for a selected coin cell with Sigma-Aldrich nano-Si. The Si loading was 0.40 mg/cm^2.

99.5% Si Resitec

Table 4.5 summarizes the coulombic efficiencies and irreversible capacity losses for each step of the precycling program for coin cells with 99.5% Si Resitec. These are average values obtained from six coin cells with Si loading 0.36 ± 0.02 mg/cm^2. The coulombic efficiency increases for each step of the precycling program, and irreversible capacity loss decreases.

Table 4.5: Coulombic efficiencies (CE) and irreversible capacity losses (ICL) for six coin cells with 99.5% Si Resitec during the precycling program. The Si loading was 0.36 ± 0.02 mg/cm^2.

Precycling step	CE [%]	ICL [mAh/g]
500 mAh/g	44.56 ± 4.85	277.1 ± 24.0
1000 mAh/g	88.15 ± 1.01	118.5 ± 10.1
1500 mAh/g	95.81 ± 0.21	63.0 ± 3.2
2000 mAh/g	97.22 ± 0.35	55.7 ± 7.3

Figure 4.7 is the differential capacity plot for each step of the precycling program for one coin cell with 99.5% Si Resitec. The first step (500 mAh/g) shows a peak at 0.08 V during the

lithiation process. The following delithiation process shows two peaks at 0.33 V and 0.49 V. The second step (1000 mAh/g) shows two peaks during the lithiation process at 0.21 V and 0.09 V. The following delithiation process shows two peaks at 0.29 V and 0.47 V. The third step (1500 mAh/g) shows two peaks during the lithiation process at 0.24 V and 0.09 V. The following delithiation process shows two peaks at 0.29 V and 0.48 V. The fourth step (2000 mAh/g) shows two peaks during the lithiation process at 0.24 V and 0.10 V. The following delithiation process shows two peaks at 0.27 V and 0.47 V.

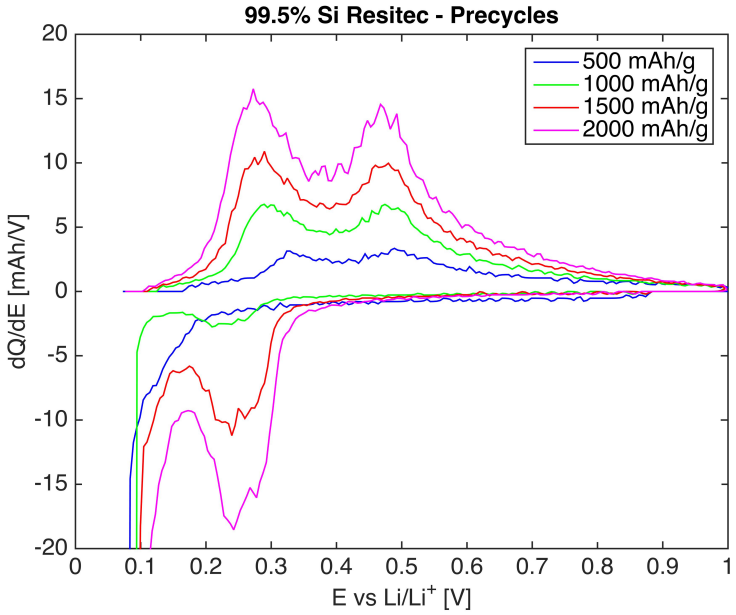

Figure 4.7: Differential capacity plot of the precycles for a selected coin cell with 99.5% Si Resitec. The Si loading was 0.36 mg/cm^2.

4.3.2 50 Cycles

Silgrain® e-Si 400

Three coin cells with electrodes made with Silgrain® e-Si 400 were tested through the 50 cycle test program. The loading of these coin cells were 0.52 ± 0.01 mg/cm^2. Figure 4.8 shows the average delithiation capacity and the average coulombic efficiencies versus cycle number obtained through this test.

The delithiation capacity (figure 4.8a) starts at 1319 mAh/g and is reduced during the first seven cycles. The minimum delithiation capacity is 878 mAh/g in cycle seven. Afterward, the delithiation capacity increases towards cycle 23, where it becomes stable. The delithiation capacities for cycles 23 to 50 are 1136 ± 11 mAh/g. The average delithiation capacity for all 50 cycles is 1099 mAh/g. The largest deviations between the three coin cells are during the earlier cycles and become smaller towards the later cycles. The voltage curves for selected cycles are shown in figure 4.9.

The coulombic efficiency (figure 4.8b) of the first cycle is considerably lower than the rest of the cycles. After the first cycle, the coulombic efficiency increases to about 99.8%. The coulombic efficiency is slowly reduced to about 99.4% in cycle 39. Upon further cycling, the coulombic efficiency increases, but the deviations between the three coin cells increase as well.

All of the three coin cells tested have a minimum in the delithiation capacity in cycle seven. The delithiation capacities for the coin cells increase and stabilize at about cycle 21 or 22. One of the three coin cells showed several cycles with a coulombic efficiencies of 100%. This coin cell showed coulombic efficiencies above 100% in cycles 42, 43, 44, 45, 47 and 50.

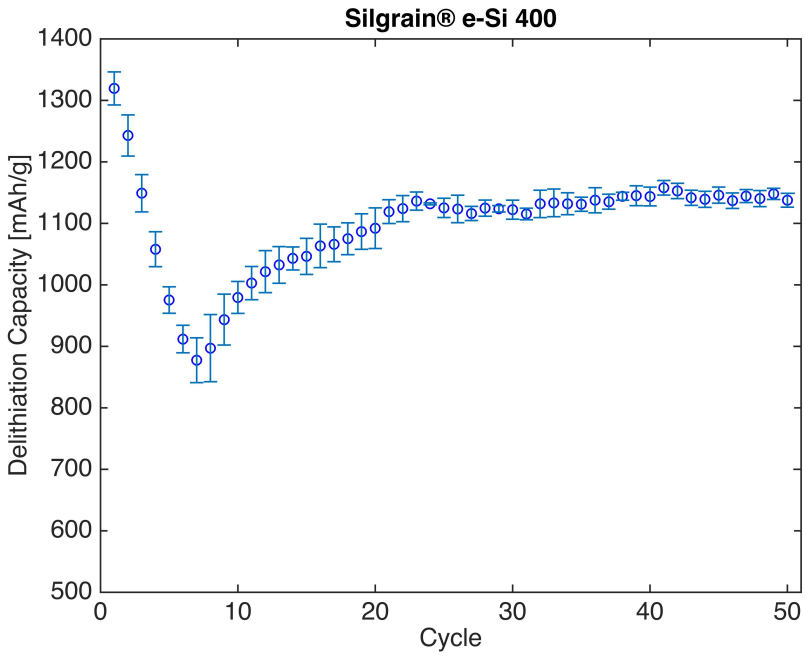

(a)

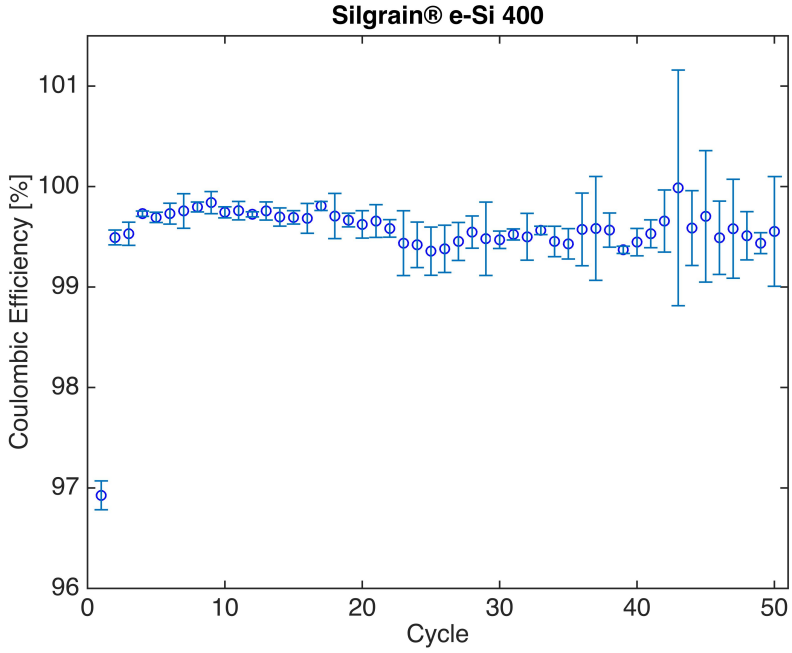

(b)

Figure 4.8: (a) Delithiation capacity versus cycle number for Silgrain® e-Si 400. (b) Coulombic efficiency versus cycle number. The Si loading was 0.52 ± 0.01 mg/cm^2.

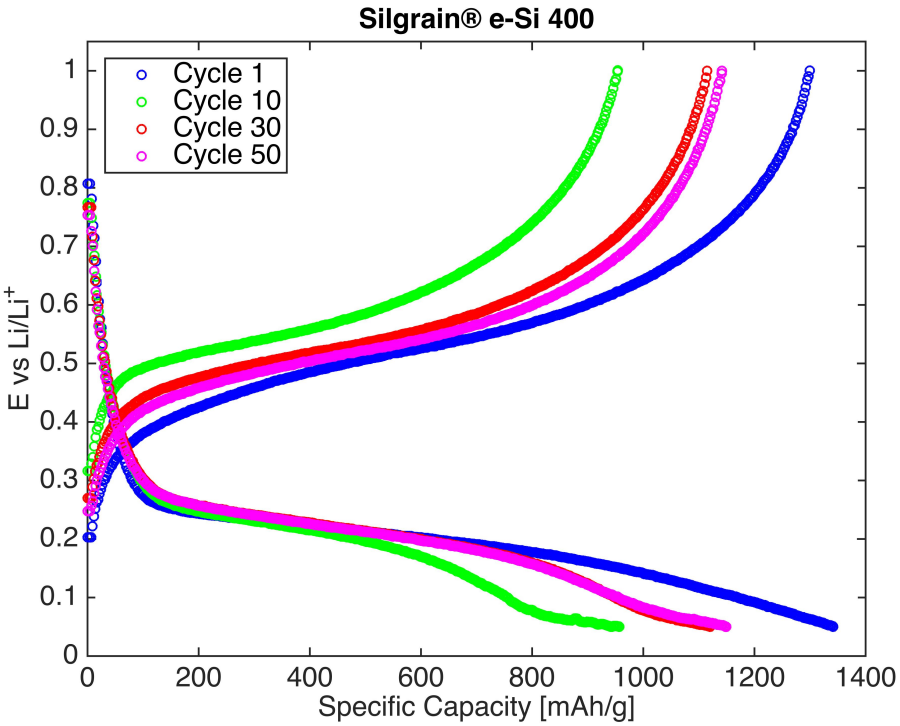

Figure 4.9: Voltage curves for selected cycles of the 50 cycle test program from a coin cell with Silgrain® e-Si 400. The Si loading of this coin cell was 0.51 mg/cm^2.

Sigma-Aldrich Nano-Si

Three coin cells with electrodes made with Sigma-Aldrich nano-Si were tested through the 50 cycle test program. The loading of these coin cells were 0.40 ± 0.01 mg/cm^2. Figure 4.10 shows the delithiation capacity and coulombic efficiency versus cycle number obtained through this test.

In the data series containing the results for all three coin cells, the average delithiation capacity starts at 1222 mAh/g for the first cycle and is reduced to a minimum of 782 mAh/g in cycle seven. Afterward, the delithiation capacity increases towards cycle 15, where it flattens out. The delithiation capacities for cycles 15 to 50 are 1003 ± 17 mAh/g.

The average delithiation capacities for the 50 cycles for the individual coin cells were 856 mAh/g, 1003 mAh/g and 1084 mAh/g. The coin cell with the lowest average delithiation capacity showed a considerably lower value than the two other coin cells. The data series with only two coin cell, therefore, excludes the results from this coin cell. The loading of these two coin cells were 0.40 ± 0.01 mg/cm^2.

In the data series containing the results for only two coin cells, the delithiation capacity starts at 1255 mAh/g for the first cycle and is reduced to a minimum of 856 mAh/g in cycle six. Afterward, the delithiation capacity increases towards cycle 15, where it flattens out. The delithiation capacities for cycles 15 to 50 are 1063 ± 12 mAh/g. The deviations between the two coin cells become larger in the last few cycles. The voltage curves for selected cycles are shown in figure 4.11.

In the data series containing the results for only two coin cells, the coulombic efficiency of the first cycle is also considerably lower than the rest of the cycles. The coulombic efficiency increases to 99.5% before it slowly decreases to 98.6% in cycle 37. After cycle 37, the coulombic efficiency increases again, but the deviations between the coin cells become larger as well.

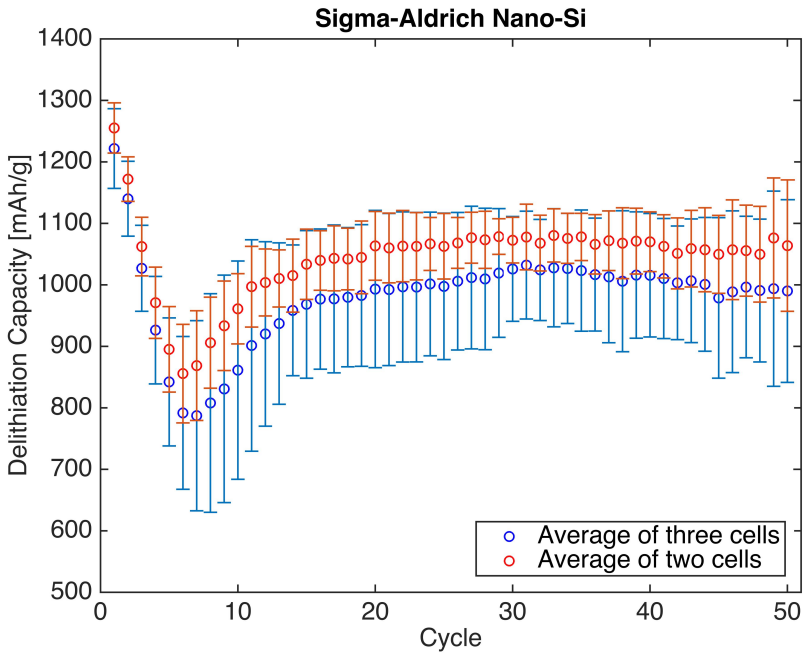

(a)

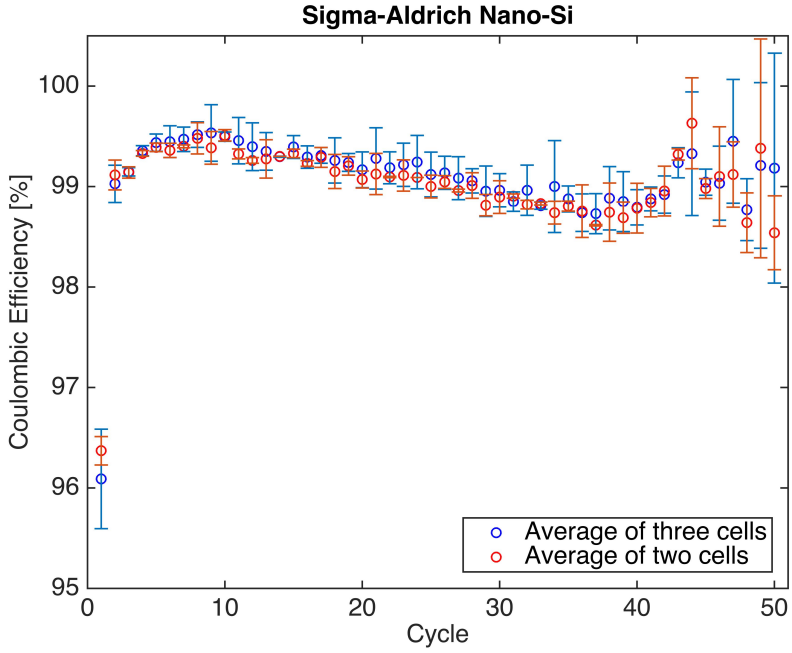

(b)

Figure 4.10: (a) Delithiation capacity versus cycle number for Sigma-Aldrich nano-Si. (b) Coulombic efficiency versus cycle number for Sigma-Aldrich nano-Si. Both "Average of three cells" and "Average of two cells" series had Si loading 0.40 ± 0.01 mg/cm^2.

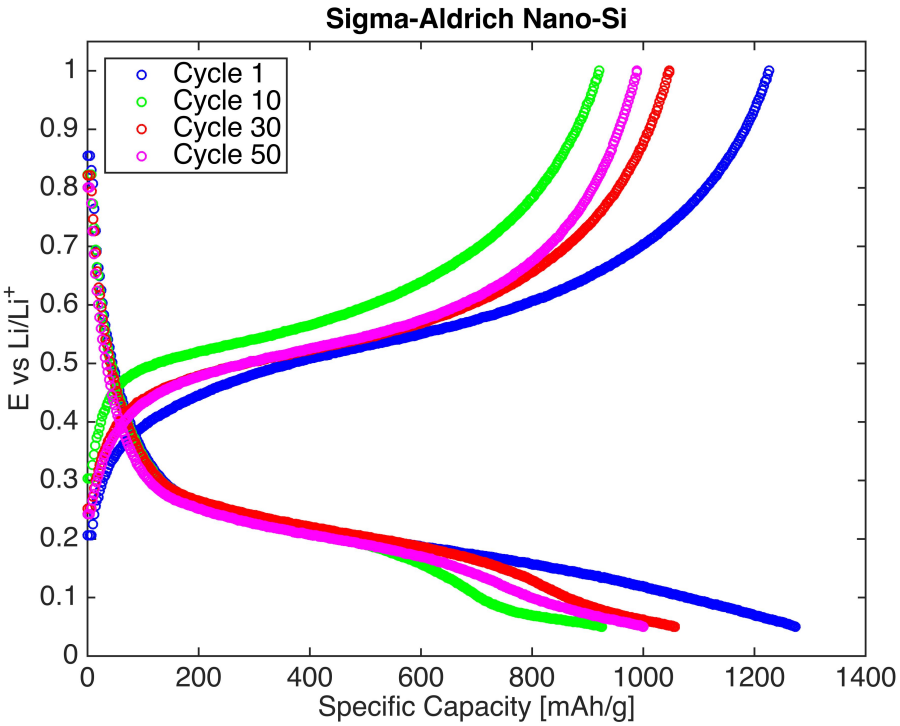

Figure 4.11: Voltage curves for selected cycles of the 50 cycle test program from a coin cell with Sigma-Aldrich nano-Si. The Si loading of this coin cell was 0.40 mg/cm^2.

99.5% Si Resitec

Three coin cells with electrodes made with 99.5% Si Resitec were tested through the 50 cycle test program. The loading of these coin cells were 0.38 ± 0.02 mg/cm^2. Figure 4.12 shows the delithiation capacity and coulombic efficiency versus cycle number obtained through this test.

The delithiation capacity (figure 4.12a) starts at 1326 mAh/g and is reduced during the first seven cycles. The minimum delithiation capacity is 1005 mAh/g in cycle seven. Afterward, the delithiation capacity increases towards cycle 30, where it becomes stable. The delithiation capacities for cycles 30 to 50 are 1251 ± 11 mAh/g. The average delithiation capacity for all 50 cycles is 1188 mAh/g. There are deviations between the three coin cells. The coin cell with the lowest average delithiation capacity through the 50 cycles, has an average of 1133 mAh/g. The coin cell with the highest average delithiation capacity through the 50 cycles, has an average of 1219 mAh/g. The last coin cell has an average delithiation capacity of 1212 mAh/g.

The coulombic efficiency (figure 4.12b) of the first cycle is considerably lower than the rest of the cycles. After the first cycle, the coulombic efficiency increases to about 99.8% in cycle seven. The coulombic efficiency is slowly reduced to about 99.1% towards cycle 50. The deviations between the three coin cells are small.

The three coin cells tested have a minimum in the delithiation capacity in either cycle six or seven. The delithiation capacities for the coin cells increase and stabilize at different cycles. They stabilize at cycle 25, cycle 28 and cycle 36. None of the coin cell showed coulombic efficiencies above 100%.

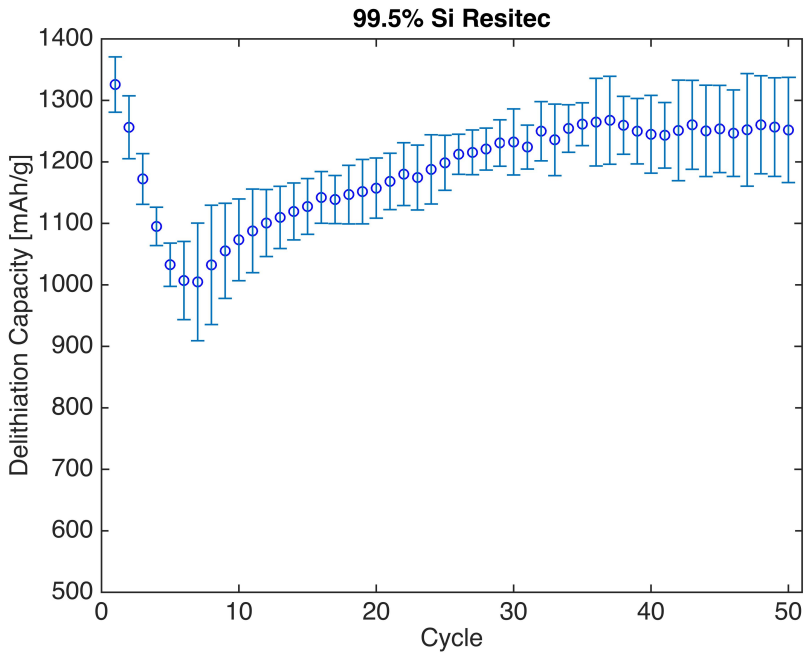

(a)

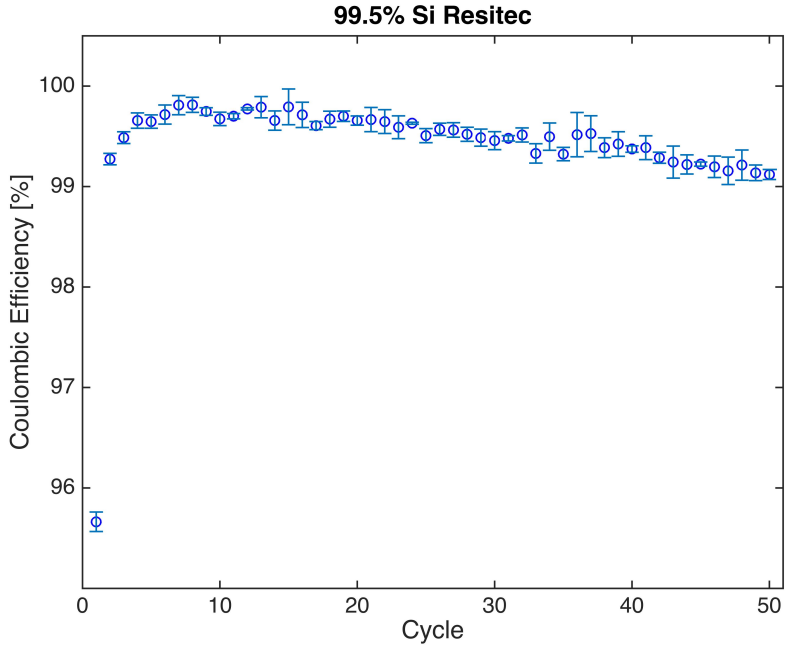

(b)

Figure 4.12: (a) Delithiation capacity versus cycle number for 99.5% Si Resitec. (b) Coulombic efficiency versus cycle number for 99.5% Si Resitec. The Si loading was 0.38 ± 0.02 mg/cm^2.

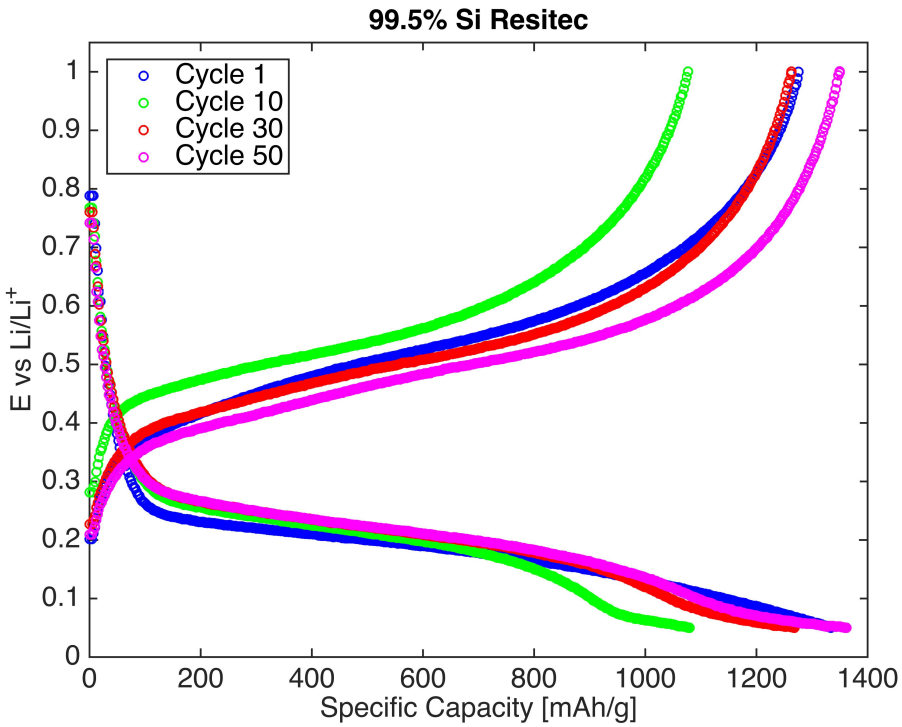

Figure 4.13: Voltage curves for selected cycles of the 50 cycle test program from a coin cell with 99.5% Si Resitec. The Si loading of this coin cell was 0.36 mg/cm^2.

BEC 01

Three coin cells with BEC 01 electrodes were tested through the 50 cycle test program. The loading of these coin cells were 0.18±0.01 mg/cm^2. Figure 4.14 shows the delithiation capacity and coulombic efficiency versus cycle number obtained through this test. The deviations between the delithiation capacities of the three cells are large in cycles 27 to 47, as can be seen by the broad error bars in figure 4.14a. The coulombic efficiency (figure 4.14b) of the first cycle is considerably lower than the rest of the cycles, with the value 96.8%. After the first cycle, the coulombic efficiency increases to 99.8% in cycle six. The coulombic efficiency is slowly reduced to 98.7% in cycle 50. The deviations between the three coin cells are small.

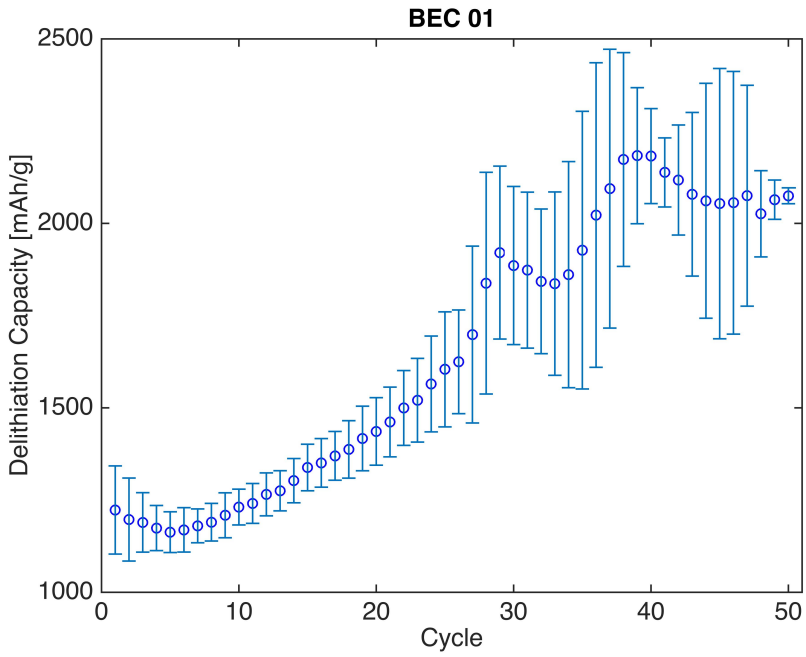

(a)

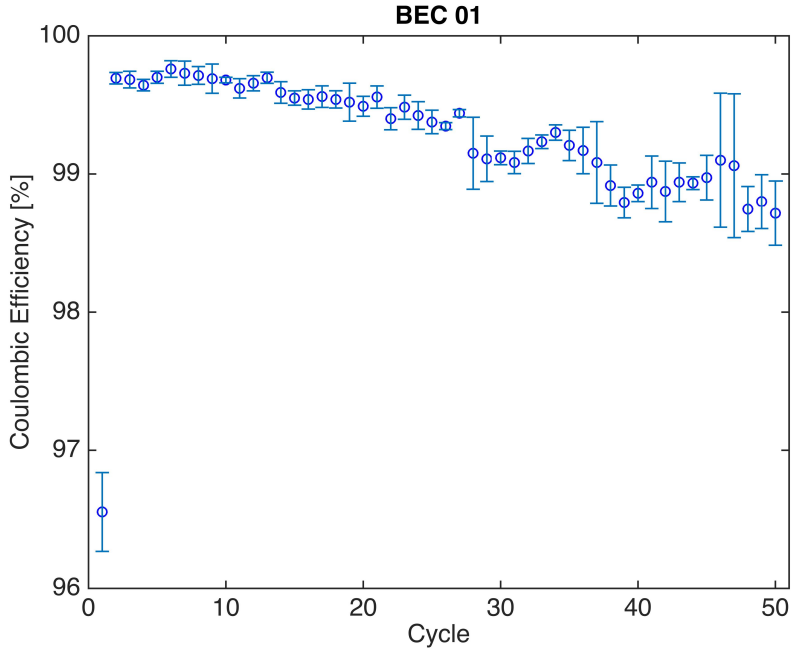

(b)

Figure 4.14: (a) Delithiation capacity versus cycle number for BEC 01 electrodes and (b) Coulombic efficiency versus cycle number for BEC 01 electrodes. The Si loading was 0.18 ± 0.01 mg/cm^2.

4.3.3 Rate Test

Silgrain® e-Si 400

Three coin cells with electrodes made with Silgrain® e-Si 400 were tested through the rate test program. The loading of these coin cells were 0.52 ± 0.01 mg/cm^2. Figure 4.15 shows the delithiation capacity and coulombic efficiency versus cycle number obtained through this test.

The rate test can be divided into five rate sections with different C-rates. Each rate section consists of five cycles. The first rate section is cycle 1 to 5, where the cells were cycled at rate 0.1C. The second rate section is cycle 6 to 10, where the cells were cycled at rate 0.2C. The third rate section is cycle 11 to 15, where the cells were cycled at rate 0.5C. The fourth rate section is cycle 16 to 20, where the cells were cycled at rate 1.0C. The fifth rate section is cycle 21 to 25, where the cells were cycled at rate 0.1C again.

As seen in figure 4.15, the rate sections have a visibly different delithiation capacities. The delithiation capacities decrease with increasing C-rate. The delithiation capacity more than fully recovers when the C-rate is decreased back to 0.1C again. The first cycle of each rate section has a different coulombic efficiency compared to the following four cycles. The coulombic efficiency of the first cycle is lower compared to the four following cycles after an C-rate increase (cycles 1, 6 11 and 16). The coulombic efficiency of the first cycle is higher compared to the four following cycles after an C-rate decrease (cycles 21). One of the coin cells deviates from the two other coin cells, as can be seen by the two data series in figure 4.15. Table 4.6 summarizes the delithiation capacities and coulombic efficiencies of the different rate sections.

Table 4.6: Summary of the rate test of electrodes with Silgrain® e-Si 400. The table reports the delithiation capacities of all five cycles in each rate section ($\overline{Q_{del}}$) and the coulombic efficiencies of the four last cycles in each rate section (CE (FLC)). The values are from the "Average of two cells" series in figure 4.15. The Si loading was 0.51 ± 0.01 mg/cm^2.

Rate section	$\overline{Q_{del}}$ [mAh/g]	CE (FLC) [%]
0.1C (1)	2394 ± 135	98.8 ± 0.1
0.2C	1992 ± 97	99.4 ± 0.1
0.5C	1384 ± 120	99.7 ± 0.1
1.0C	678 ± 203	99.0 ± 0.2
0.1C (2)	2596 ± 56	98.2 ± 0.3

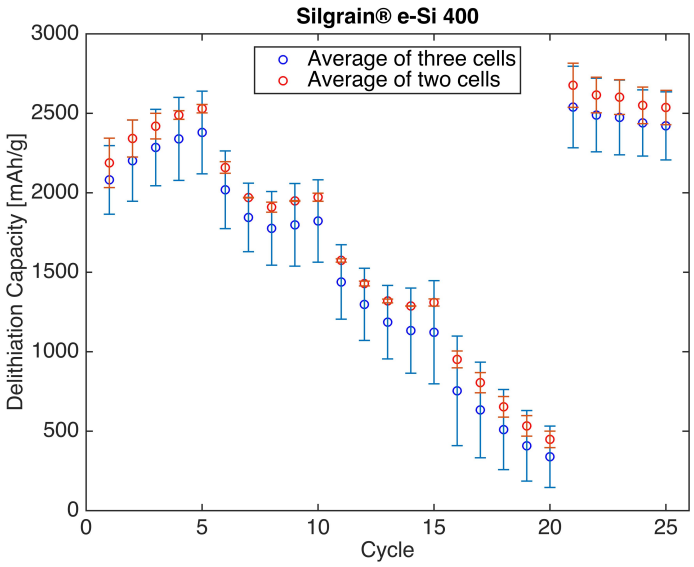

(a)

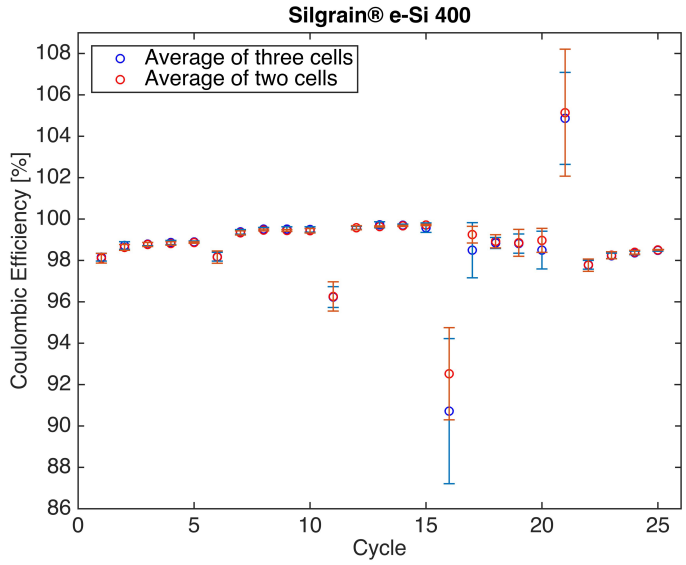

(b)

Figure 4.15: (a) Delithiation capacity versus cycle number Silgrain® e-Si 400. (b) Coulombic efficiency versus cycle number for Silgrain® e-Si 400. "Average of three cells" had a Si loading of 0.52 ± 0.01 mg/cm^2. "Average of two cells" had a Si loading of 0.51 ± 0.01 mg/cm^2. Cycles 1 to 5 were cycled at 0.1C, cycles 6 to 10 at 0.2C, cycles 11 to 15 at 0.5C, cycles 16 to 20 at 1.0C and cycles 21 to 25 at 0.1C.

Sigma-Aldrich Nano-Si

Three coin cells with electrodes made with Sigma-Aldrich nano-Si were tested through the rate test program. The loading of these coin cells were 0.41 ± 0.01 mg/cm^2. Figure 4.16 shows the delithiation capacity and coulombic efficiency versus cycle number obtained through this test.

As seen in figure 4.16, the rate sections have a visibly different delithiation capacities. The delithiation capacities decrease with increasing C-rate. The delithiation capacity more than fully recovers when the C-rate is decreased back to 0.1C again. The first cycle of each rate section has a different coulombic efficiency compared to the following four cycles. The coulombic efficiency of the first cycle is lower compared to the four following cycles after an C-rate increase (cycles 1, 6 11 and 16). The coulombic efficiency of the first cycle is higher compared to the four following cycles after an C-rate decrease (cycles 21). Table 4.7 summarizes the delithiation capacities and coulombic efficiencies of the different rate sections.

Table 4.7: Summary of the rate test of electrodes with Sigma-Aldrich nano-Si. The table reports the delithiation capacities of all five cycles in each rate section ($\overline{Q_{del}}$) and the coulombic efficiencies of the four last cycles in each rate section (CE (FLC)). The coin cells had a Si loading of 0.41 ± 0.01 mg/cm^2.

Rate section	$\overline{Q_{del}}$ [mAh/g]	CE (FLC) [%]
0.1C (1)	2232 ± 91	98.1 ± 0.1
0.2C	1863 ± 50	98.8 ± 0.1
0.5C	1337 ± 80	99.2 ± 0.1
1.0C	857 ± 76	99.5 ± 0.2
0.1C (2)	2334 ± 44	97.4 ± 0.3

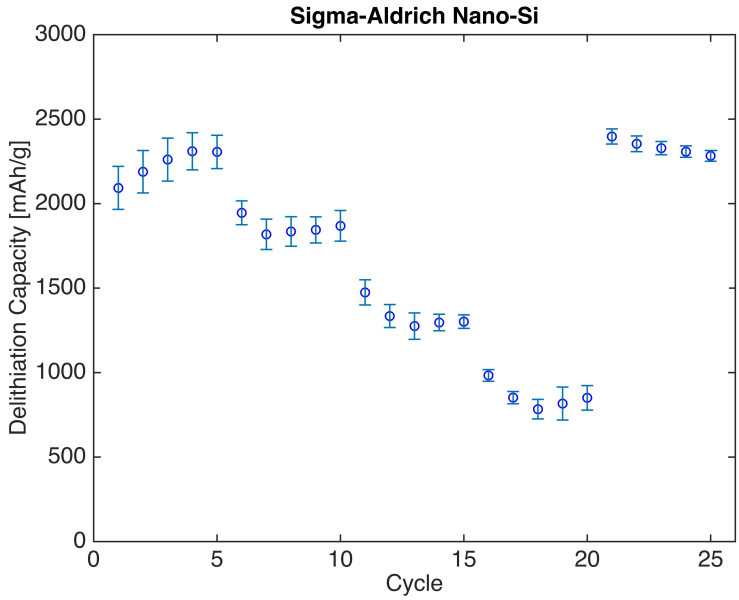

(a)

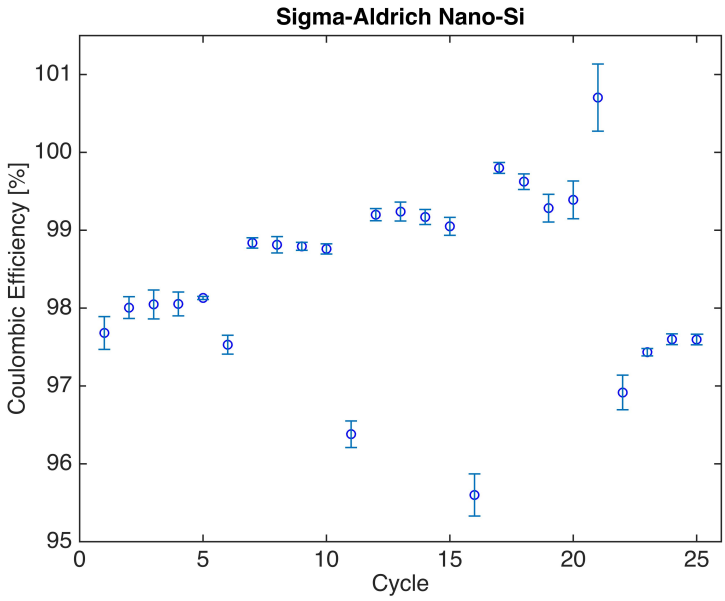

(b)

Figure 4.16: (a) Delithiation capacity versus cycle number for Sigma-Aldrich nano-Si (b) Coulombic efficiency versus cycle number for Sigma-Aldrich nano-Si. The Si loading was 0.41 ± 0.01 mg/cm^2. Cycles 1 to 5 were cycled at 0.1C, cycles 6 to 10 at 0.2C, cycles 11 to 15 at 0.5C, cycles 16 to 20 at 1.0C and cycles 21 to 25 at 0.1C.

99.5% Si Resitec

Three coin cells with electrodes made with 99.5% Si Resitec were tested through the rate test program. The loading of these coin cells were 0.35 ± 0.01 mg/cm^2. Figure 4.17 shows the delithiation capacity and coulombic efficiency versus cycle number obtained through this test.

As seen in figure 4.17, the rate sections have a visibly different delithiation capacities. The delithiation capacities decrease with increasing C-rate. The delithiation capacity more than fully recovers when the C-rate is decreased back to 0.1C again. The first cycle of each rate section has a different coulombic efficiency compared to the following four cycles. The coulombic efficiency of the first cycle is lower compared to the four following cycles after an C-rate increase (cycles 1, 6 11 and 16). The coulombic efficiency of the first cycle is higher compared to the four following cycles after an C-rate decrease (cycles 21). Table 4.8 summarizes the delithiation capacities and coulombic efficiencies of the different rate sections.

Table 4.8: Summary of the rate test of electrodes with 99.5% Si Resitec. The table reports the delithiation capacities of all five cycles in each rate section ($\overline{Q_{del}}$) and the coulombic efficiencies of the four last cycles in each rate section (CE (FLC)). The coin cells had a Si loading of 0.35 ± 0.01 mg/cm^2.

Rate section	$\overline{Q_{del}}$ [mAh/g]	CE (FLC) [%]
0.1C (1)	2403 ± 138	98.4 ± 0.1
0.2C	1987 ± 107	99.2 ± 0.1
0.5C	1335 ± 135	99.6 ± 0.1
1.0C	692 ± 134	100.2 ± 0.2
0.1C (2)	2719 ± 41	98.1 ± 0.3

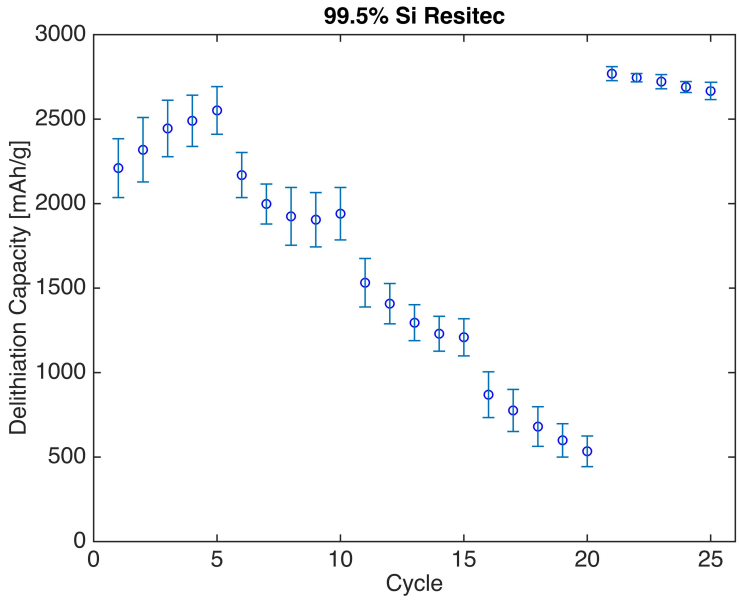

(a)

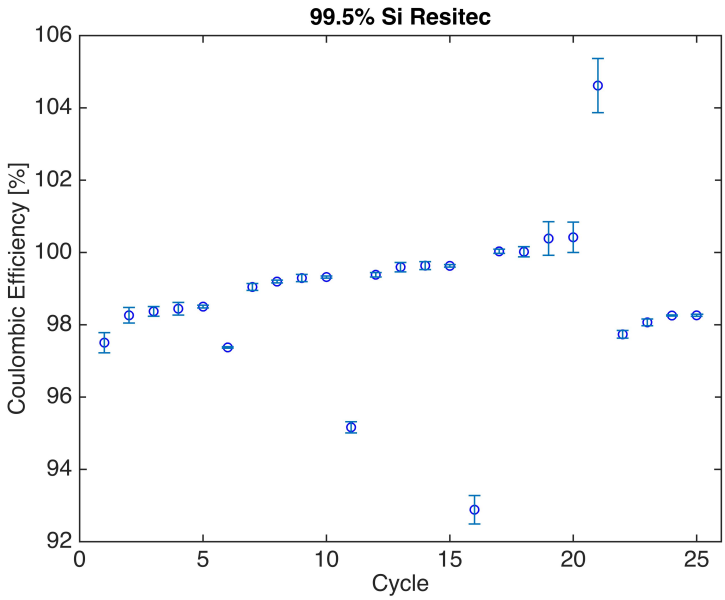

(b)

Figure 4.17: (a) Delithiation capacity versus cycle number for 99.5% Si Resitec and (b) shows the coulombic efficiency versus cycle number for 99.5% Si Resitec. The Si loading was 0.35 ± 0.01 mg/cm^2. Cycles 1 to 5 were cycled at 0.1C, cycles 6 to 10 at 0.2C, cycles 11 to 15 at 0.5C, cycles 16 to 20 at 1.0C and cycles 21 to 25 at 0.1C.

BEC 01

Three coin cells with BEC 01 electrodes were tested through the rate test program. The loading of these coin cells were 0.19 ± 0.01 mg/cm^2. Figure 4.18 shows the delithiation capacity and coulombic efficiency versus cycle number obtained through this test.

As seen in figure 4.18, the rate sections have a visibly different delithiation capacities. The delithiation capacities decrease with increasing C-rate. The delithiation capacity more than fully recovers when the C-rate is decreased back to 0.1C again. The first cycle of each rate section has a different coulombic efficiency compared to the following four cycles. The coulombic efficiency of the first cycle is lower compared to the four following cycles after an C-rate increase (cycles 1, 6 11 and 16). The coulombic efficiency of the first cycle is higher compared to the four following cycles after an C-rate decrease (cycles 21). Table 4.9 summarizes the delithiation capacities and coulombic efficiencies of the different rate sections.

Table 4.9: Summary of the rate test of BEC 01 electrodes. The table reports the delithiation capacities of all five cycles in each rate section ($\overline{Q_{del}}$) and the coulombic efficiencies of the four last cycles in each rate section (CE (FLC)). The coin cells had a Si loading of 0.19 ± 0.01 mg/cm^2.

Rate section	$\overline{Q_{del}}$ [mAh/g]	CE (FLC) [%]
0.1C (1)	1952 ± 143	99.1 ± 0.1
0.2C	1786 ± 58	99.5 ± 0.1
0.5C	1298 ± 62	99.8 ± 0.1
1.0C	839 ± 58	99.8 ± 0.2
0.1C (2)	2610 ± 15	98.8 ± 0.2

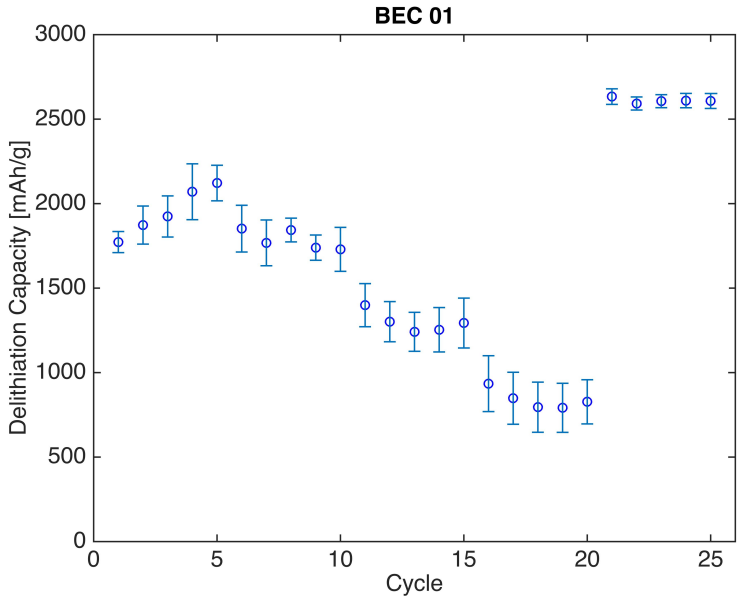

(a)

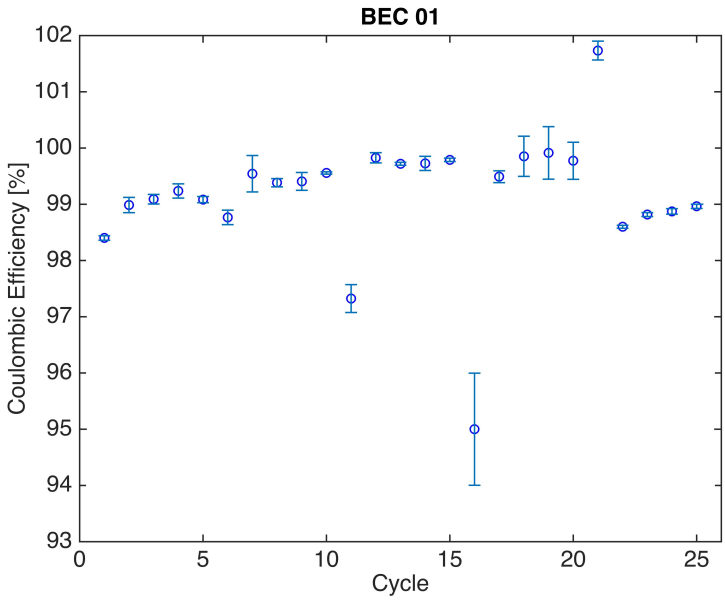

(b)

Figure 4.18: (a) Delithiation capacity versus cycle number for BEC 01 electrodes. (b) Coulombic efficiency versus cycle number for BEC 01 electrodes. The Si loading was 0.19 ± 0.01 mg/cm^2. Cycles 1 to 5 were cycled at 0.1C, cycles 6 to 10 at 0.2C, cycles 11 to 15 at 0.5C, cycles 16 to 20 at 1.0C and cycles 21 to 25 at 0.1C.

4.4 Electrochemical Impedance Spectroscopy

One PAT-cell for each of the three Si powders were tested. The Si loading of the cell with Silgrain® e-Si 400 was 0.48 mg/cm^2, the cell with Sigma-Aldrich nano-Si was 0.37 mg/cm^2 and with 99.5% Si Resitec was 0.36 mg/cm^2.

A few difficulties were encountered during the EIS tests. Due to technical issues, there were no potential steps in the precycling program. However, there were potential steps in the 50 cycle test program. Also due to technical issues, the electrodes did not lithiate entirely to 2000 mAh/g during the fourth step of the precycle program. No EIS measurements for Sigma-Aldrich nano-Si were obtained for the 50 cycle test due to technical issues as well. The EIS measurements were taken in between the lithiation process and the delithiation process of the same cycle, which in combination with the potential steps made it difficult to calculate the coulombic efficiencies for the cycles where the EIS measurements were taken.

The results from the EIS tests are given as Nyquist plots in figures 4.19 and 4.21. The axes have been scaled with respect to amount of Si, and the curves have been gathered by moving the curves along the $Re(Z)$-axis to intersect $Re(Z)$=0. This was done to make the results from the different Si powders more comparable with respect to the electrode resistance.

An estimate of the electrode resistance, R_1, was obtained by extrapolating the circular region of the Nyquist plot and finding the intersection with $-Im(Z) = 0$. This is illustrated in figures 4.19 and 4.21. The electrode resistance is equal to the diameter of the half circle measured along $-Im(Z) = 0$. The electrolyte resistances obtained were ∼1.3 ohm/mg(Si) for the cells with Sigma-Aldrich nano-Si and 99.5% Si Resitec, while ∼0.5 ohm/mg(Si) for the cells with Silgrain® e-Si 400.

The delithiation capacities, coulombic efficiencies and estimated electrode resistance values for the precycling steps are given in table 4.10. The lithiation capacities achieved before the EIS measurements and the estimated electrode resistances obtained from the 50 cycle test are given in this table 4.11. Delithiation capacities and coulombic efficiencies from the 50 cycle test, from which the EIS measurements were taken, are given in figure 4.21.

The cumulative irreversible capacity losses after the precycling program were 390 mAh/g for Silgrain® e-Si 400, 736 mAh/g for Sigma-Aldrich nano-Si and 401 mAh/g for 99.5% Si Resitec. The cumulative irreversible capacity losses after the both complete precycling and 50 cycle programs were 3531 mAh/g for Silgrain® e-Si 400 and 3120 mAh/g for 99.5% Si Resitec.

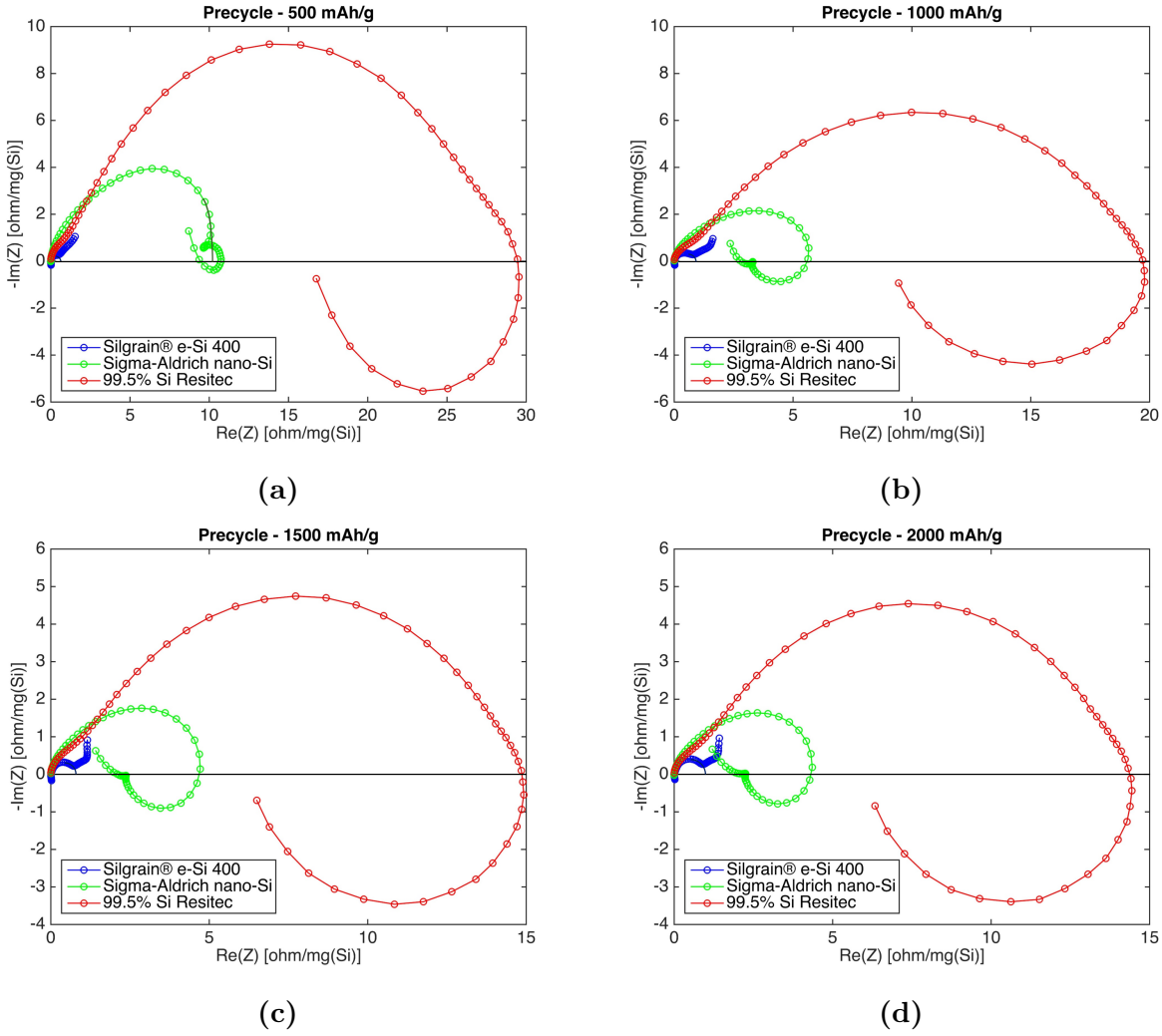

Figure 4.19: Nyquist plots with extrapolated curves from the precycling program. The measurements were taken after the lithiation processes in the precycling program, but no potential steps were done before the EIS measurements.

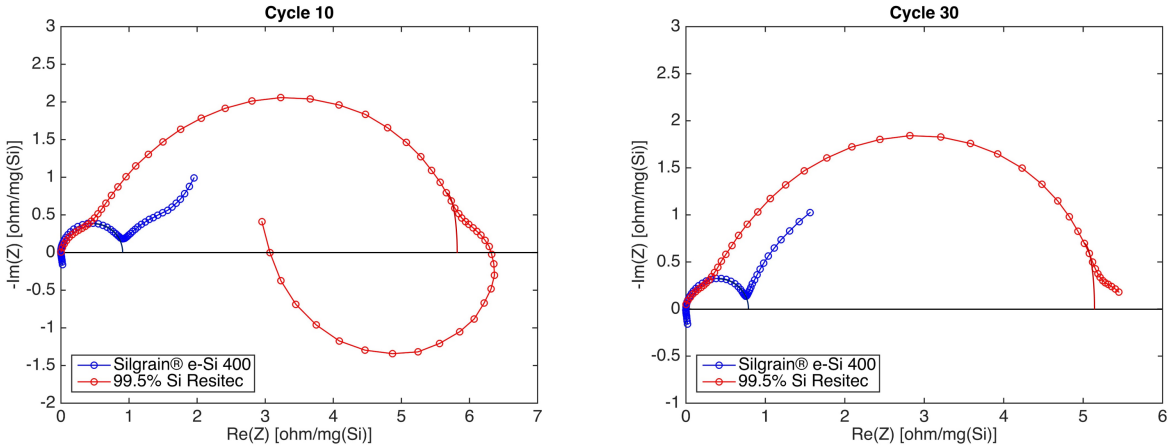

(a)

(b)

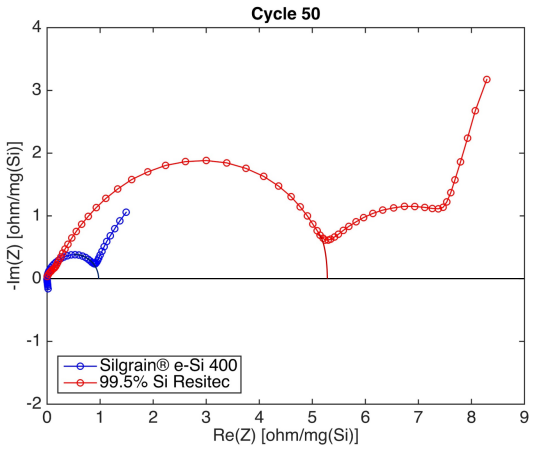

(c)

Figure 4.20: Nyquist plots with extrapolated curves from the 50 cycle test program. The measurements were taken after the lithiation processes. Potential steps were done before the EIS measurements.

Table 4.10: The delithiation capacities (Q_{del}), coulombic efficiencies (CE) and simplified electrode resistance (R_1) values for the precycling steps. No potential steps were done before in the precycling program.

	Type of Si powder	Q_{del} [mAh/g]	CE [%]	R_1 [ohm/mg(Si)]
Precycle - 500 mAh/g	Silgrain® e-Si 400	230.1	46.02	0.6
	Sigma-Aldrich nano-Si	86.6	17.56	10.2
	99.5% Si Resitec	170.9	34.65	29.4
Precycle - 1000 mAh/g	Silgrain® e-Si 400	910.7	91.07	0.9
	Sigma-Aldrich nano-Si	799.2	79.92	5.6
	99.5% Si Resitec	903.6	90.36	19.7
Precycle - 1500 mAh/g	Silgrain® e-Si 400	1492.9	98.84	0.8
	Sigma-Aldrich nano-Si	1415.2	94.77	4.7
	99.5% Si Resitec	1486.4	99.54	14.8
Precycle - 2000 mAh/g	Silgrain® e-Si 400	1746.4	99.25	1.0
	Sigma-Aldrich nano-Si	1722.4	97.14	5.7
	99.5% Si Resitec	1749.2	101.45	14.7

Table 4.11: The lithiation capacities (Q_{lit}) and simplified electrode resistance (R_1) values for the precycling steps. Potential steps were done before the EIS measurements, and the lithiation capacity values include the capacity obtained during the potential steps.

	Type of Si powder	Q_{lit} [mAh/g]	R_1 [ohm/mg(Si)]
Cycle 10	Silgrain® e-Si 400	2946.7	0.9
	99.5% Si Resitec	2918.1	5.9
Cycle 30	Silgrain® e-Si 400	1554.8	0.8
	99.5% Si Resitec	1807.1	5.1
Cycle 50	Silgrain® e-Si 400	857.4	1.0
	99.5% Si Resitec	1155.2	5.3

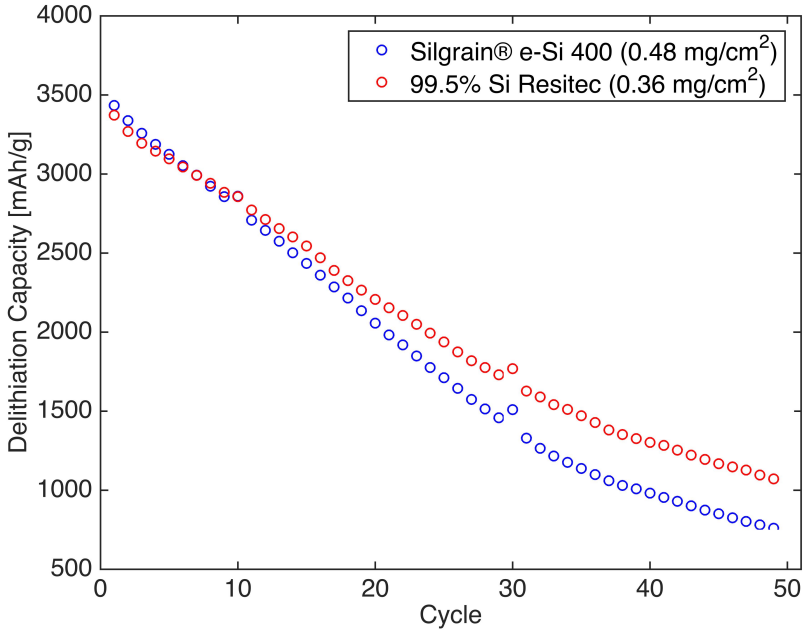

(a)

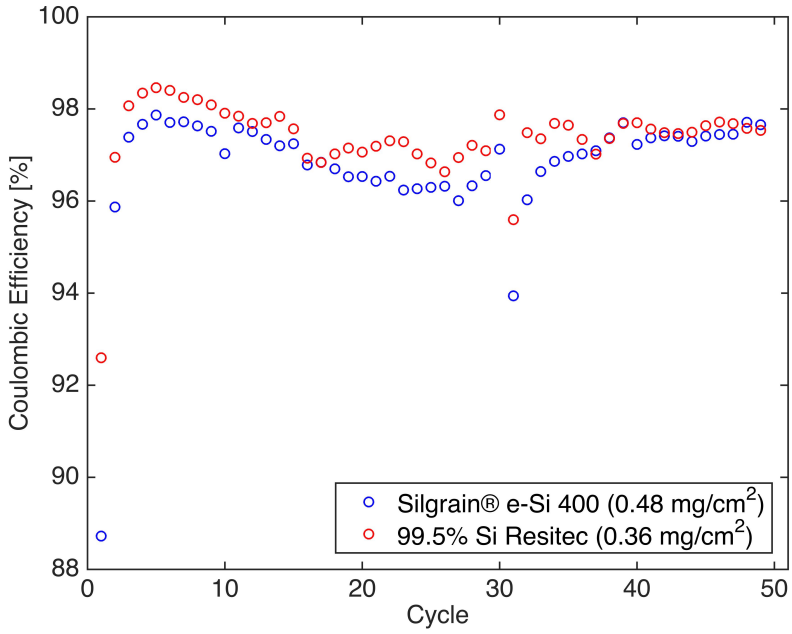

(b)

Figure 4.21: (a) Delithiation capacity versus cycle number and (b) coulombic efficiency versus cycle number obtained from the PAT-cells cycled through the 50 cycle test program. Potential steps were done in this test. The delithiation capacity and coulombic efficiency values in the figure include the capacity gained during the potential steps. EIS measurements were done in the delithiated states of cycles 10, 30 and 50.

Chapter 5

Discussion

5.1 Characterization of Si powders as received

The diffraction patterns for all four Si powders (figures 4.1 to 4.4) show distinct intensity peaks. Thus, all four Si powders have crystalline characteristics. Sigma-Aldrich nano-Si and Si kerf show a weak bump at low angles ($2\theta < 20°$), which could indicate some amorphous character as well. However, the crystalline character dominates. The positions of the intensity peaks in the diffraction patterns of Silgrain® e-Si 400, Sigma-Aldrich nano-Si and 99.5% Si Resitec correspond well to those of Si from the International Centre for Diffraction Data (ICDD) database. The positions of the intensity peaks in the diffraction pattern of Si kerf correspond well to those of Si and SiC from the same database. Only Silgrain® e-Si 400, Sigma-Aldrich nano-Si and 99.5% Si Resitec were further processed into Si electrodes since the Si kerf contained significant amounts of SiC, which is inactive to reactions with Li-ions.

The calculated crystallite sizes from Scherrer's formula (equation 2.20) show that the crystallite sizes for the four Si powders are different. However, all the calculations show large standard deviations, and will not be evaluated any further. There could be several reasons why the standard deviations are high. The crystallite size was calculated based on an average for all Si intensity peaks in a diffraction pattern. Since the intensity peaks represent different crystallographic planes, an average-based calculation would assume that the crystallites are equally sized in each of these directions. If this is not the real case, it could explain the large standard deviations. A second reason could be if the crystallite size range is broad. A third reason could be that the diffraction patterns are not refined enough to get precise results. The only refinement used in the diffraction patterns is $K_{\alpha 2}$ stripping. An additional

refinement to consider could be instrumental broadening. A fourth reason is that the XRD step size is too large for precise results as well.

Silgrain® e-Si 400, Sigma-Aldrich nano-Si and 99.5% Si Resitec are all crystalline Si powders, but with different particle sizes and different specific surface areas. Sigma-Aldrich nano-Si has a significantly higher specific surface area than both Silgrain® e-Si 400 and 99.5% Si Resitec. Furthermore, 99.5% Si Resitec has about twice the specific surface area of Silgrain® e-Si 400. The purities of the Silgrain® e-Si 400, Sigma-Aldrich nano-Si and 99.5% Si Resitec powders are similar, in addition to having many of the same impurity elements.

5.2 Electrochemical Characterization of Coin Cells

5.2.1 Precycling

As can be seen in tables 4.3, 4.4 and 4.5, the coin cells with Sigma-Aldrich nano-Si show the lowest coulombic efficiencies through the precycling steps, while coin cells with Silgrain® e-Si 400 show the highest coulombic efficiencies in all steps except for the last. There is a major difference between the coulombic efficiencies in the first step, but the difference is smaller in the following three steps. This difference, especially in the first step, can most likely be attributed to the difference of specific surface area of the three Si powders and SEI formation. As mentioned in section 2.6.1, the irreversible capacity loss increases with increasing specific surface area due to SEI formation on a larger surface area. Sigma-Aldrich nano-Si has a significantly higher surface area than Silgrain® e-Si 400 and 99.5% Si Resitec. It is therefore expected that the coin cells with Sigma-Aldrich nano-Si have the highest irreversible capacity loss and lowest coulombic efficiency. Furthermore, 99.5% Si Resitec has higher surface area than Silgrain® e-Si 400, which can explain why coin cells with 99.5% Si Resitec show a lower coulombic efficiency than coin cells with Silgrain® e-Si 400. It should, however, be mentioned that the relationship between the BET surface area and the coulombic efficiencies is not linear. The BET surface area of Sigma-Aldrich nano-Si is significantly higher than 99.5% Si Resitec, but only $\sim$5% lower coulombic efficiency. There is no linear relationship between the BET surface area and the irreversible capacity loss during the first precycle either.

The differential capacity plots as seen in figures 4.5, 4.6 and 4.7 show peaks at similar potentials. The dQ/dE values for the curves vary between the Si powders, which can be attributed to that the Si powder show different specific delithiation capacities and have

different Si loadings. Figure 5.1 suggests which reactions are associated with the different peaks with the basis of the conclusions of Ogata et al. (2014) in table 2.1 [19]. Only the differential capacity plot of Silgrain® e-Si 400 is illustrated because all three Si powders show similar peak positions.

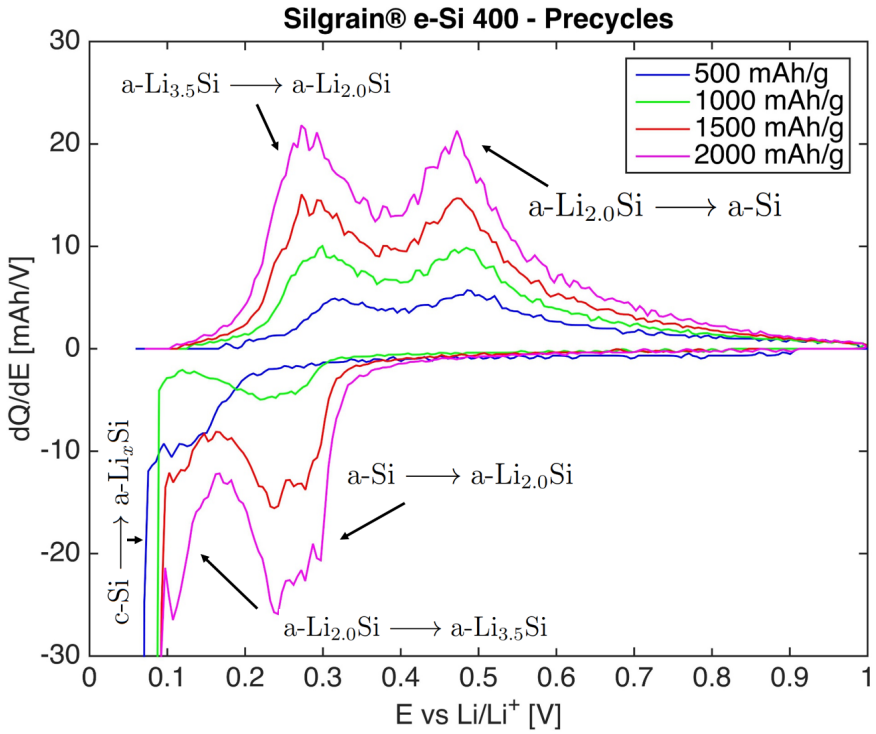

Figure 5.1: Differential capacity plot of the precycles for coin cell with Silgrain® e-Si 400. Suggested lithiation and delithiation reactions are also given based on [19]. This is an edited version of figure 4.5.

The same reactions happen at the same potentials during lithiation and delithiation of all three Si powders during the precycling program. However, the three Si powders have different irreversible capacity losses due to the difference in specific surface areas causing varying amounts of SEI formation.

5.2.2 Performance over 50 Cycles

Figure 5.2 summarizes figures 4.8, 4.10, 4.12 and 4.14 without the errorbars. This figure is meant to simplify comparisons of the different types of Si electrodes. The Sigma-Aldrich nano-Si series contains only the results of two coin cells.

The results from the 50 cycle test program show similar trends for coin cells with Silgrain® e-Si 400, Sigma-Aldrich nano-Si and 99.5% Si Resitec, both with respect to delithiation capacity and the coulombic efficiency. The delithiation capacity decreases the first few cycles, before increasing again and becoming stable. Although the results look relative similar in figure 5.2, there are some minor differences when looking at the numbers reported in section 4.3.2. The coin cells with 99.5% Si Resitec show the highest average delithiation capacity over all 50 cycles and the highest delithiation capacity in the stabilized region. However, the coin cells with 99.5% Si Resitec reach their stable region at a higher cycle number compared to Silgrain® e-Si 400 and Sigma-Aldrich nano-Si. The coin cells with Sigma-Aldrich nano-Si reach their stable region at a lower cycle number than Silgrain® e-Si 400 and 99.5% Si Resitec, but also show the lowest average delithiation capacity over all 50 cycles and the lowest average delithiation capacity in the stabilized region. On another note, none of the three Si powders show considerable capacity fade after 50 cycles. A longer cycle test is needed to study if there is a possible difference of cyclability between the Si electrodes.

The difference between the electrochemical performances of the three Si powders seems small in figure 5.2a. However, the Si loading should be taken into account when studying these results. The Si loadings of the Silgrain® e-Si 400 electrodes had a slightly higher loading than the aimed range of 0.4-0.5 mg/cm^2, while the electrodes with 99.5% Si Resitec had a slightly lower loading than the aimed range. Although these Si electrodes were not within the aimed Si loading range, it was determined that they would be used for electrochemical testing due to time restrictions. The Si loadings of the 99.5% Si Resitec electrodes were lower than Silgrain® e-Si 400, and slightly lower than Sigma-Aldrich nano-Si. Since a higher specific capacity can be expected from an electrode with lower loading, the 99.5% Si Resitec electrodes have an advantage compared to the two other Si powders. Silgrain® e-Si 400 and 99.5% Si Resitec seem to perform relatively similar and slightly better than Sigma-Aldrich nano-Si, when taking the Si loading into consideration.

The coin cells with Silgrain® e-Si 400 and 99.5% Si Resitec show similar coulombic efficiencies. Apart from the first cycle, both show coulombic efficiencies above 99% throughout the 50 cycles. Coin cells with Sigma-Aldrich nano-Si show lower coulombic efficiencies than Silgrain® e-Si 400 and 99.5% Si Resitec. The reason for this could be due to continuous irreversible capacity loss from SEI formation through the 50 cycles, and could be an explaination for the lower delithiation capacities compared to the two other Si powders.

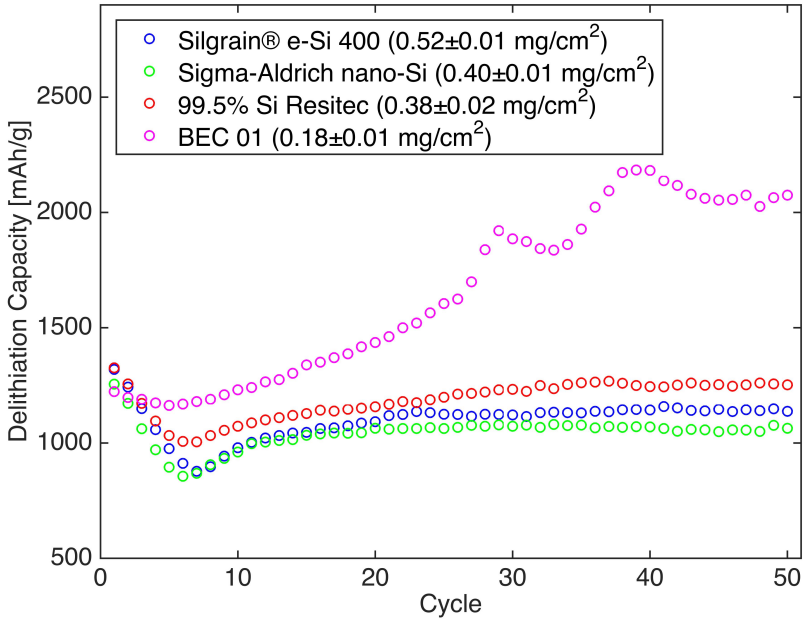

(a)

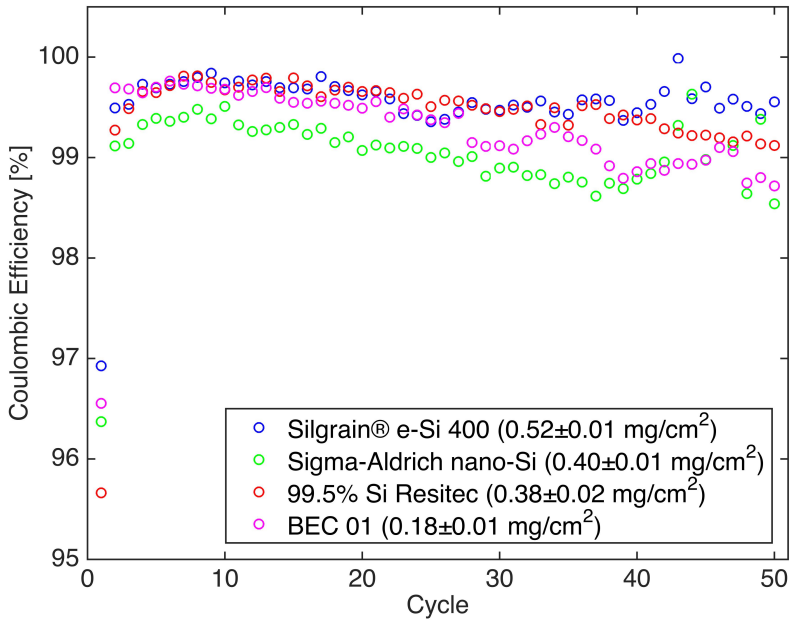

(b)

Figure 5.2: (a) Delithiation capacity versus cycle number and (b) coulombic efficiency versus cycle number for for all four types of Si electrodes tested through the 50 cycle test program. This is a replotted version of figures 4.8, 4.10 and 4.12.

The BEC 01 electrodes show a different delithiation capacity trend, and the delithiation capacities are higher compared to the three Si powders. The Si loadings of the BEC 01 electrodes are approximately half the loading of the other Si electrodes. It is therefore expected that the delithiation capacity is higher than the other Si electrodes. However, it is not certain if the Si loading causes the difference in the trend of the delithiaton capacity. The BEC 01 electrodes also differ from the tape casted electrodes because they are Si-graphite composite electrodes, and they fabricated differently: Si powder was ball milled; slurry was mixed by a using planetary centrifugal mixer; the electrodes were screen-printed. Thus, there can be several reasons why the performance of BEC 01 electrodes differ from the tape casted electrodes. The comparisons between the tape casted electrodes and the prefabricated electrodes are therefore limited.

It should be mentioned that the large deviations between parallel tests in the 50 cycle test of Sigma-Aldrich nano-Si and rate test of Silgrain® e-Si 400 could indicate that casts were not homogeneous and that the preparation procedures were not optimal. The performance deviations could have been caused by an inhomogeneous distribution of Si and CB, causing inactive areas in the Si electrode casts. Although the Si electrodes were proved homogeneous upon visual inspection, there exist more precise techniques for quality control. A suggestion for improvement is to check for material clusters in the slurry using a grindometer. On another note, the coin cell assembly process could also have caused these deviations. The coin cell assembly involves fine work by hand, such as aligning the coin cell parts. Some deviations between cells should be expected. Variation of Si loading was not considered to cause the deviations because the loadings of the tested cells were similar.

The preparation procedures for the Si electrodes of the three Si powders were different. One important difference between the preparation techniques was the amount of liquid used. The amount of liquid was adjusted mainly to be able to wet the Si powder surface and achieve homogeneous slurries, but also to adjust the Si loading. More buffer solution was needed to prepare the Sigma-Aldrich electrode casts due to the higher specific surface area compared to Silgrain® e-Si 400 and 99.5% Si Resitec. A consequence of this is that the amount of buffer components, $C_6H_8O_7$ and KOH, also increase. As seen in table 3.6, there is a $\sim$2 wt% higher amount of buffer components in the Sigma-Aldrich nano-Si electrodes than the two other electrode casts. The increase of buffer components was on behalf of Si and CB. How the increased percentage of buffer components affects the electrochemical performance is beyond the scope of this thesis.

5.2.3 Rate Performance

Figure 5.3 summarizes figures 4.15, 4.16, 4.17 and 4.18 without the errorbars. This figure is meant to simplify comparisons of the different types of Si electrodes. The Silgrain® e-Si 400 series contains only the results of two coin cells.

Which of the three Si powders show the highest delithiation capacity does vary between the different rate sections. Silgrain® e-Si 400 and 99.5% Si Resitec show the highest values in the 0.1C and 0.2C sections. The smallest differences between the three Si powders are found in the 0.5C section, but Silgrain® e-Si 400 has a slightly higher delithiation capacity than the two other powders. Sigma-Aldrich nano-Si shows the highest delithiation capacity in the 1.0C section, but the differences between the three Si powders are small. All the three Si powders show full recoveries of delithiation capacities when the rate is decreased back to 0.1C again. Silgrain® e-Si 400 and 99.5% Si Resitec seem to perform best in this rate section when considering the differences in Si loading.

There is no clear best performer among the three Si powders in the rate test, but the coin cells were not tested at too high rates. There could have been a clearer difference at higher C-rates than 1.0C. However, Sigma-Aldrich nano-Si shows the most stable profile within each rate section because it has the most consistent delithiation capacities within each rate sections.

A few comments can be made about the rate test. It could have been expected that Sigma-Aldrich nano-Si would perform better in a rate test compared to Silgrain® e-Si 400 and 99.5% Si Resitec, due to the smaller particle size and larger specific surface area. As mentioned in section 2.6.1, this allows for shorter diffusion lengths and higher rate capability. On the other hand, Sigma-Aldrich nano-Si shows the lowest coulombic efficiencies in all rate sections except for the 1.0C section, which could be due to continuous SEI formation. Also, it can be expected that Sigma-Aldrich nano-Si has small pores due to the small particle size. Both the SEI and small pores could affect the rate performance negatively.

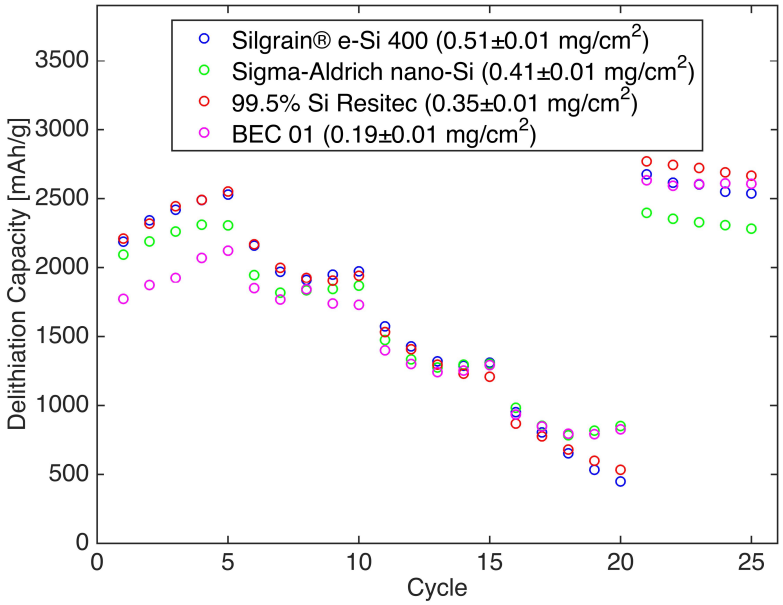

(a)

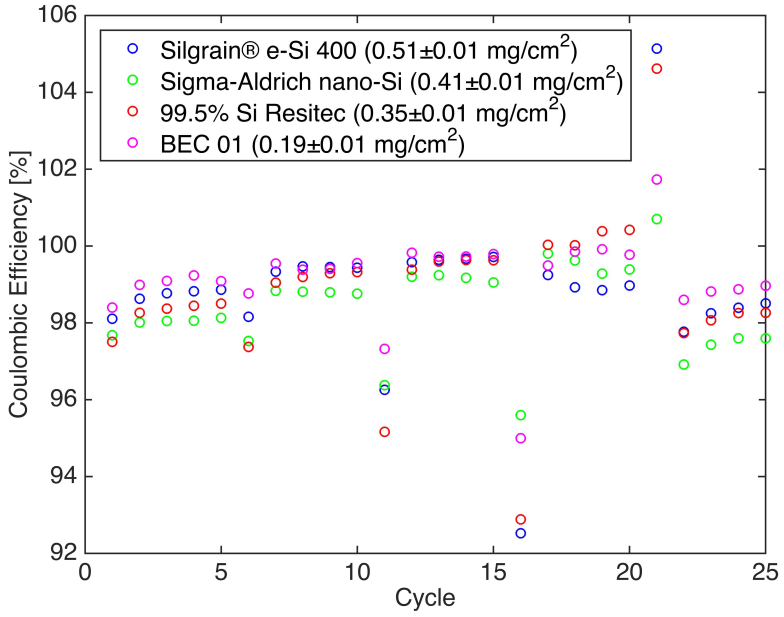

(b)

Figure 5.3: (a) Delithiation capacity versus cycle number and (b) coulombic efficiency versus cycle number for for all four types of Si electrodes tested through the rate test program. Cycles 1 to 5 were cycled at 0.1C, cycles 6 to 10 at 0.2C, cycles 11 to 15 at 0.5C, cycles 16 to 20 at 1.0C and cycles 21 to 25 at 0.1C. This is a replotted version of figures 4.15, 4.16 and 4.17.

Combining both the 50 cycle test and the rate test results of coin cells, it can be seen that neither Si powder performs significantly better than the others when measuring performance by delithiation capacity. The differences between the three Si powders were smallest at 0.5C of the rate test. With this in mind, the differences between the three Si powders could have been larger in a 50 cycle test at another rate. The BEC 01 electrodes in the 50 cycle test show a considerable higher delithiation capacities and a different trend compared to the tape casted electrodes of the three Si powder. The BEC 01 electrodes in the rate test show a similar performance compared to the tape casted electrodes of the three Si powders.

5.3 Electrochemical Impedance Spectroscopy Analysis

The EIS analysis done in this thesis is a simplified analysis. As mentioned in section 3.7 of the experimental chapter, the electrode resistance is calculated based on the diameter of the circular region of the Nyquist plots, figures 4.19 and 4.21. This is a simplification, and in reality, such curves can contain contributions from several resistances from different origins. As seen in figures 4.19, the circular region of the 99.5% Si Resitec curve shows bends in both ends of the region, indicating that the circular region could contain contributions from more than one resistance component. In the same figure, the curves of Silgrain® e-Si 400 show a second region which can be caused by diffusion. Lastly, the Sigma-Aldrich nano-Si curves show curls, which could be due to inductance. EIS modeling can be used to find the more specific contributions of these components, but this is beyond the scope of this thesis. The electrolyte resistance is not considered because all the tested cells contained the same type of electrolyte in equal amounts.

Several factors can contribute to the electrode resistance. The SEI layer, the degree of lithiation, the Si loading and the pathways for electrons through the electrode are among these factors. These factors will first be discussed with respect to what effect they are expected to have on the different Si electrodes based on the physical characteristics of the Si powders and electrochemical cycling data obtained during the EIS tests.

A thicker layer of the electrical insulting SEI can increase the electrode resistance. The cell with the Sigma-Aldrich nano-Si electrode have the lowest coulombic efficiency and the highest irreversible capacity losses compared to the two other cells in all steps of the precycling program. For this reason, the cell with Sigma-Aldrich nano-Si is expected to have accumulated more SEI during the precycling program compared to the two other cells. The cell with the Silgrain® e-Si 400 electrode and the cell with the 99.5% Si Resitec electrode do not

differ significantly with respect to cumulative irreversible capacity loss during the precycling program. However, the cell with the Silgrain® e-Si 400 electrode has a higher cumulative irreversible capacity loss than the cell with 99.5% Si Resitec after 50 cycles, and generally has lower coulombic efficiencies. The electrode with Silgrain® e-Si 400 is because of this expected to contain more SEI compared to the electrode with the 99.5% Si Resitec. This is interesting considering that 99.5% Si Resitec has twice the BET surface area of Silgrain® e-Si 400, and thereby having a larger surface where SEI can form. It is expected that the contribution from the SEI layer to the electrode resistance is higher for the cell with Sigma-Aldrich nano-Si compared to the two other cells during the precycling program. It is also expected that the contribution from the SEI layer to the electrode resistance is higher for the cell with Silgrain® e-Si 400 compared to the cell with 99.5% Si Resitec during the 50 cycle program.

A high degree of lithiation can cause an increased electrode resistance because it is expected to cause higher resistance towards further Li-ion diffusion. Discussing the degree of lithiation with respect to electrode resistance is only relevant for the EIS measurements taken during the 50 cycle test program. This is because all cells were lithiated equally during the precycling program. The cell with the 99.5% Si Resitec electrode achieved a higher degree of lithiation before the EIS measurements compared to the cell with Silgrain® e-Si 400. It is therefore expected that the contribution from the degree of lithiation with respect to the electrode resistance is higher for the cell 99.5% Si Resitec compared to the cell with Silgrain® e-Si 400 during the 50 cycle program.

The Si loading contributes to the electrode resistance due to Si being a semiconductor. A higher Si loading is expected to cause a higher contribution to the electrode resistance. The cell with Silgrain® e-Si 400 has a higher loading than the two other cells, and it is because of this expected that the contribution from the Si loading to the electrode resistance is higher for the cell with Silgrain® e-Si 400 compared to the two others.

The pathways in which the electrons to pass through also contributes to the electrode resistance. Disconnected pathways for electrons between particles or between particles and the current collector can also provide a negative contribution to the electrode resistance. Poor distribution of active material and conductive additive could cause an increased electrode resistance because of disconnected or complex pathways for electrons as well. Another point is that electrons are transferred between particles through a combination of binding material and conductive additive. Furthermore it is reasonable that binding material may have a lower electric conductivity. Electrodes consisting of smaller particles contain more of these pas-

sages, which could cause a higher electrode resistance. This point implies that the cell with Sigma-Aldrich nano-Si may have a negative contribution with respect to electrode resistance due to more transfers between particles.

The electrode resistance during all EIS measurements of the precycling program is in the following ascending order: Silgrain® e-Si 400, Sigma-Aldrich nano-Si, 99.5% Si Resitec. When comparing these results with the expectations discussed above, there is a reason to believe that these electrode resistances are a combination of several contributions. The SEI alone can be an explanation why the electrode resistance is larger for the Sigma-Aldrich nano-Si electrode than the Silgrain® e-Si 400 electrode. However, SEI alone does not explain why the 99.5% Si Resitec electrode has a larger electrode resistance than Sigma-Aldrich nano-Si electrodes. The same argument could be made for the aspect concerning electron transfer through binding material and Sigma-Aldrich nano-Si. The Si loading is highest in the cell with Silgrain® e-Si 400, but this cell shows the lowest electrode resistance. The degree of lithiation is similar for all three types of electrodes and does not explain the different electrode resistances either. The electrode resistance seems to be a combination of several contributing factors. How the different contributions scale is not known. EIS modeling could be used to investigate the specific contributions of the different electrode resistance components, but this is beyond the scope of this thesis.

All three EIS measurements taken during the 50 cycle test show that 99.5% Si Resitec has a higher electrode resistances than Silgrain® e-Si 400. The Silgrain® e-Si 400 electrode has more SEI than 99.5% Si Resitec electrode. The electrode resistance caused by SEI should, therefore, be larger in the Silgrain® e-Si 400 electrode. The degree of lithiation is higher for 99.5% Si Resitec electrode than Silgrain® e-Si 400 electrode. The electrode resistance caused by the degree of lithiation should, therefore, be larger in the 99.5% Si Resitec electrode. How the effect the SEI layer and the degree of lithiation compare with respect electrode resistances is not known, but might be revealed by EIS modeling. However, this is beyond the scope of this thesis.

As discussed earlier, it is not entirely clear if the Si electrode casts are completely homogeneous because the quality control was only done by visual inspection. Some degree of inhomogeneous Si electrodes should therefore be expected. Disconnected pathways for electrons due to poor distribution of active material and conductive additive can increase electrode resistances, and furthermore be a factor contributing the varying electrode resistances of the different types of Si electrodes.

It should be mentioned that the performance of an electrode in a PAT-cell was different from

the performance of the same type of electrode in a coin cell. The delithiation capacity steadily decreased upon cycling in PAT-cells, instead of stabilizing as for the coin cells. The coulombic efficiencies were lower in the PAT-cells compared to the coin cells. The performance difference between the coin cell and PAT-cell tests could be due to the cell setup. The PAT-cells have a thicker separator of a different material, in addition to a larger amount of electrolyte compared to the coin cells. Another reason could be that the PAT-cells went through potential steps during testing, while the coin cells did not.

It should be acknowledged that only one cell was tested for each of the Si powders during the EIS analysis. More parallel tests should be done in order to confirm if the results are repeatable. It should also be mentioned that results show that both cells achieve higher lithiation capacities than the theoretical capacity during the first cycle of the 50 cycle program. One explanation for this could be an error when weighing process of the Si electrodes, in such a way that there is in reality more Si on the electrodes than measured. Another reason could be the formation of SEI or lithiation of surface oxides, as mention in section 2.5.1. Nevertheless, this affects the reliability of the EIS results negatively.

To summarize, the EIS measurements indicate that there is a difference between the electrode resistances of the electrodes made from the different Si powders. Several factors raise concerns about the reliability of the results: Technical issues during testing; the simplified analysis; difficulties in identifying origins of the varying electrode resistances; measurements above theoretical values; only one test per Si powder. A reliable conclusion concerning the differences between the electrodes resistances of the different Si electrodes will therefore not be made. More tests should be done before any proper conclusion can be made. EIS modeling should be utilized as well to measure the different contributions.

Chapter 6

Conclusion

The main goal of this thesis was to compare Si anodes for lithium-ion batteries made from three different types of Si powders - a commercialized micron-sized powder (Silgrain® e-Si 400), a nano-sized powder (Sigma-Aldrich nano-Si), and a Si kerf (99.5% Si Resitec). The three Si powders were compared based on physical characteristics, medium-term cycling performance, rate performance and electrode resistance. Performance measures were based on delithiation capacities. The following conclusions were made:

- All three Si powders are crystalline powders with similar purities, but have different specific surface areas. The Sigma-Aldrich nano-Si powder shows a significantly higher surface area than the Silgrain® e-Si 400 and 99.5% Si Resitec powders, while the 99.5% Si Resitec powder has twice the surface area of the Silgrain® e-Si 400 powder.
- Si electrodes with Silgrain® e-Si 400 and 99.5% Si Resitec show a slightly better performance over 50 cycles compared to the Si electrodes with Sigma-Aldrich nano-Si when tested in a coin cell setup. None of the powders show capacity fade after 50 cycles. Tests with Sigma-Aldrich nano-Si show low coulombic efficiencies that are most likely attributed to continuous SEI formation on the large surface of the powder.
- All three Si powders show similar rate performance up to 1.0C.
- No reliable conclusion could be made concerning the electrode resistances of the Si electrodes made with the different powders. More parallel tests are needed for a reliable comparison.

Chapter 7

Further Work

A few suggestions for further work and reasons behind them are stated below.

- A couple of electrochemical tests showed deviations between parallel tests. It was discussed that inhomogeneous Si electrode casts could have caused these deviations. The only quality control technique used to ensure homogeneous casts was visual inspection. A suggestion for further work is to retry the slurry mixing procedures and control the homogeneity of the slurries using a more precise quality control technique than visual inspection. An example is to use a grindometer to check the slurries for larger agglomerates.
- The results from the rate test showed that the differences between the different electrodes were smallest when cycled at 0.5C. Repeating a 50 cycle test at a different rate might reveal larger differences between the performance of the Si electrodes.
- The rate performances of the three Si powders were evaluated by a rate test with rates up to 1.0C. This is not a very high rate. The rate performances should, therefore, be evaluated by a rate test with rates up to 3.0C or 5.0C.
- None of the Si powders tested showed significant capacity fade after 50 cycles. A longer cycling test could reveal if there is a difference between the cyclabilities of three Si powders.
- No reliable conclusion could be made based on the electrochemical impedance spectroscopy analysis. This analysis should be retried with more parallel tests to ensure repeatable results. Also, proper EIS modeling could be used to investigate the specific contributions of the different electrode resistance components.

Bibliography

[1] Harald Norrud Pollen. Silicon anodes for lithium ion batteries: Investigation of the change in crystallinity after electrochemical cycling, 2017.

[2] James Manyika, Michael Chui, Jacques Bughin, Richard Dobbs, Peter Bisson, and Alex Marrs. Disruptive technologies: Advances that will transform life, business, and the global economy, 2013.

[3] Naoki Nitta, Feixiang Wu, Jung Tae Lee, and Gleb Yushin. Li-ion battery materials: present and future. *Materials today*, 18(5):252–264, 2015.

[4] Richard JD Tilley. *Understanding Solids: The Science of Materials*. John Wiley & Sons, 2013.

[5] Delong Ma, Zhanyi Cao, and Anming Hu. Si-based anode materials for li-ion batteries: a mini review. *Nano-Micro Letters*, 6(4):347–358, 2014.

[6] Tzu-Yang Huang, Baskar Selvaraj, Hung-Yu Lin, Hwo-Shuenn Sheu, Yen-Fang Song, Chun-Chieh Wang, Bing Joe Hwang, and Nae-Lih Wu. Exploring an interesting si source from photovoltaic industry waste and engineering it as a li-ion battery high-capacity anode. *ACS Sustainable Chemistry & Engineering*, 4(10):5769–5775, 2016.

[7] John B Goodenough and Kyu-Sung Park. The li-ion rechargeable battery: a perspective. *Journal of the American Chemical Society*, 135(4):1167–1176, 2013.

[8] Keith Oldham, Jan Myland, and Alan Bond. *Electrochemical science and technology: fundamentals and applications*. John Wiley & Sons, 2011.

[9] Chao Xu. *Non-aqueous Electrolytes and Interfacial Chemistry in Lithium-ion Batteries*. PhD thesis, Acta Universitatis Upsaliensis, 2017.

[10] Brian J Landi, Matthew J Ganter, Cory D Cress, Roberta A DiLeo, and Ryne P Raffaelle. Carbon nanotubes for lithium ion batteries. *Energy & Environmental Science*, 2(6):638–654, 2009.

[11] Masaki Yoshio, Takaaki Tsumura, and Nikolay Dimov. Electrochemical behaviors of silicon based anode material. *Journal of Power Sources*, 146(1-2):10–14, 2005.

[12] Henning Kaland. On the cycling performance and stability of silicon-based anodes in lithium-ion batteries: Revealing challenges and failure mechanisms using post mortem analyses. mathesis, Norwegian University of Science and Technology, 2017.

[13] Cynthia A Lundgren, Kang Xu, T Richard Jow, Jan Allen, and Sheng S Zhang. Lithium-ion batteries and materials. In *Springer Handbook of Electrochemical Energy*, pages 449–494. Springer, 2017.

[14] D. A. J. Rand R. M. Dell. *Understanding Batteries: Rsc.* ROYAL SOCIETY OF CHEMISTRY, 2001.

[15] George E Blomgren. The development and future of lithium ion batteries. *Journal of The Electrochemical Society*, 164(1):A5019–A5025, 2017.

[16] Pankaj Arora and Zhengming Zhang. Battery separators. *Chemical reviews*, 104(10):4419–4462, 2004.

[17] Christian Julien, Alain Mauger, Ashok Vijh, and Karim Zaghib. Lithium batteries. In *Lithium Batteries*, pages 29–68. Springer, 2016.

[18] MN Obrovac and VL Chevrier. Alloy negative electrodes for li-ion batteries. *Chemical reviews*, 114(23):11444–11502, 2014.

[19] Ken Ogata, E Salager, CJ Kerr, AE Fraser, Caterina Ducati, Andrew James Morris, Stephan Hofmann, and Clare Philomena Grey. Revealing lithium–silicide phase transformations in nano-structured silicon-based lithium ion batteries via in situ nmr spectroscopy. *Nature communications*, 5:3217, 2014.

[20] Jing Li and JR Dahn. An in situ x-ray diffraction study of the reaction of li with crystalline si. *Journal of The Electrochemical Society*, 154(3):A156–A161, 2007.

[21] Kun Feng, Matthew Li, Wenwen Liu, Ali Ghorbani Kashkooli, Xingcheng Xiao, Mei Cai, and Zhongwei Chen. Silicon-based anodes for lithium-ion batteries: From fundamentals to practical applications. *Small*, 14(8):1702737, 2018.

[22] Candace K Chan, Hailin Peng, Gao Liu, Kevin McIlwrath, Xiao Feng Zhang, Robert A Huggins, and Yi Cui. High-performance lithium battery anodes using silicon nanowires. *Nature nanotechnology*, 3(1):31–35, 2008.

[23] Hui Wu, Gerentt Chan, Jang Wook Choi, Ill Ryu, Yan Yao, Matthew T McDowell, Seok Woo Lee, Ariel Jackson, Yuan Yang, Liangbing Hu, et al. Stable cycling of double-walled silicon nanotube battery anodes through solid-electrolyte interphase control. *Nature nanotechnology*, 7(5):310–315, 2012.

[24] Jeannine R Szczech and Song Jin. Nanostructured silicon for high capacity lithium battery anodes. *Energy & Environmental Science*, 4(1):56–72, 2011.

[25] Emil Roduner. Size matters: why nanomaterials are different. *Chemical Society Reviews*, 35(7):583–592, 2006.

[26] Xiao Hua Liu, Li Zhong, Shan Huang, Scott X Mao, Ting Zhu, and Jian Yu Huang. Size-dependent fracture of silicon nanoparticles during lithiation. *Acs Nano*, 6(2):1522–1531, 2012.

[27] Hans Joachim Moeller. Wafering of silicon. In *Semiconductors and Semimetals*, volume 92, pages 63–109. Elsevier, 2015.

[28] In Hyuk Son, Jong Hwan Park, Soonchul Kwon, Seongyong Park, Mark H Rümmeli, Alicja Bachmatiuk, Hyun Jae Song, Junhwan Ku, Jang Wook Choi, Jae-man Choi, et al. Silicon carbide-free graphene growth on silicon for lithium-ion battery with high volumetric energy density. *Nature communications*, 6:7393, 2015.

[29] M. Mansfield and C. O'Sullivan. *Understanding Physics*. Wiley, 2011.

[30] Kristin Høydalsvik. *Nanostructure of dip-coated Yttria-doped Zirconia Sol-Gel coatings studied by grazing-incidence small-angle x-ray scattering*. PhD thesis, 2010.

[31] Mark Weller, Tina Overton, Jonathan Rourke, and Fraser Armstrong. *Inorganic Chemistry*. Oxford University Press, 6 edition, 2014.

[32] Ashish Chauhan and Priyanka Chauhan. Powder xrd technique and its applications in science and technology. *Journal of Analytical & Bioanalytical Techniques*, 5(5):1, 2014.

[33] B.D. Cullity and S.R. Stock. *Elements of X-Ray Diffraction*. Prentice Hall, 3rd edition edition, 2001.

[34] William D. Callister and David G. Rethwisch. *Materials Science and Engineering*. John Wiley & Sons Ltd, 8 edition, 2011.

[35] Erik Unosson. *Antibacterial Strategies for Titanium Biomaterials*. PhD thesis, Acta Universitatis Upsaliensis, 2015.

[36] Charles Kittel. *Introduction to Solid State Physics 8E*. John Wiley and Sons Ltd, 8 edition, 2005.

[37] Sverre Magnus Selbach and Kristin Høydalsvik. Tmt4166 powder x-ray diffraction. University Lecture, 2016.

[38] S.E. Dann. *Reactions and Characterization of Solids*. Tutorial Chemistry Texts. Royal Society of Chemistry, 2000.

[39] Nina Hwang and Andrew R Barron. Bet surface area analysis of nanoparticles. *The Connexions project*, pages 1–11, 2011.

[40] I. Chorkendorff and J.W. Niemantsverdriet. *Concepts of Modern Catalysis and Kinetics*. Wiley, 2003.

[41] H. Berg. *Batteries for Electric Vehicles*. Cambridge University Press, 2015.

[42] Roberto Scipioni. *Performance and Lifetime Limiting Effects in Li-ion Batteries*. PhD thesis, Department of Energy Conversion and Storage, Technical University of Denmark, 2016.

[43] Evgenij Barsoukov and J Ross Macdonald. *Impedance spectroscopy: theory, experiment, and applications*. John Wiley & Sons, 2018.

[44] Tony Jaumann, Juan Balach, Ulrike Langklotz, Viktar Sauchuk, Marco Fritsch, Alexander Michaelis, Valerij Teltevskij, Daria Mikhailova, Steffen Oswald, Markus Klose, et al. Lifetime vs. rate capability: Understanding the role of fec and vc in high-energy li-ion batteries with nano-silicon anodes. *Energy Storage Materials*, 6:26–35, 2017.

[45] Elkem. Silgrain(r) e-si. https://www.elkem.com/no/elkem-silicon-materials/batteries/silgrain-e-si/, 2018. Accessed 2018-04-23.

[46] Jorunn Voje. E-mail correspondence, 2018.

[47] Sebastiano Rupiani. E-mail correspondence, 2018.

[48] Manali Kumari. E-mail correspondence, 2018.

[49] Alexander Ulyashin. E-mail correspondence, 2018.

[50] Magali Gauthier, Driss Mazouzi, David Reyter, Bernard Lestriez, Philippe Moreau, Dominique Guyomard, and Lionel Roue. A low-cost and high performance ball-milled si-based negative electrode for high-energy li-ion batteries. *Energy & Environmental Science*, 6(7):2145–2155, 2013.

[51] Arinne Lyman, Anita Zarebi, Becky Koszalinski, and Michael Alexander. Ophthalmic dose compliance monitor. *BME*, 200:300, 2005.

[52] EL-CELL GmbH. *User Manual PAT-Cell – Release 2.2*, 2018.

[53] EL-CELL GmbH. *User Manual PAT-Core - Release 1.01*, 2018.

[54] International Centre for Diffraction Data (ICDD). Powder diffraction file (pdf-4+2016 rdb), 2016.

Appendices

Appendix A

Developing Procedures for Preparing Silicon Electrodes

The coin cells made during the project by the author in the autumn of 2017 showed rapid capacity fade [1]. There was a suspicion that inhomogeneous Si electrode casts could have caused the rapid capacity fade because of nonuniform distribution of active material and conductive additives causing inactive areas in the casts. It was determined to focus on achieving homogeneous casts in this thesis work. The development of the procedures for making Si electrodes of the three Si powders was done using a trial-and-error strategy. Adjustments were made to an initial preparation procedure, with the aim of getting homogeneous Si electrodes with a Si loading of 0.4-0.5 mg/cm^2. This section describes some of the iterations and failed attempts encountered through the experimental work of making Si electrodes of Silgrain® e-Si 400 and 99.5% Si Resitec. The aim of this appendix chapter is to describe the development process, and to describe some experiences gained through the development process.

It should be mentioned that the Si electrode casts are named by a numbering system using six digits. The first and second numbers states the batch of buffer solution used. The third and fourth numbers state the batch of binder solution used. The fifth and sixth numbers state the slurry batch number. As an example, cast 030824 is made with buffer solution from the third batch of buffer solution, the eighth batch of binder solution and is the 24th batch of slurry.

A.1 Initial Slurry Mixing Procedure

The initial slurry mixing procedure for both Silgrain® e-Si 400 and 99.5% Si Resitec was done by the following procedure: 0.300 g of Si powder and 0.125 g of CB were added to a steel jar and mixed in a shaker mill for 5 minutes at 25 Hz. Binder solution equivalent to 0.075 g of Na-CMC, 1.725 g binder solution, was added to the steel jar before being further mixed in a shaker mill for 60 minutes at 25 Hz. The total weight ratio between Na-CMC and buffer solution was 1:23.

The slurries were distributed and tape casted onto wrinkle free Cu foil using a tape caster (RK K Control Coater) with speed setting "1" and a meterbar with tread depth "4" (RK Print Coat Instruments U.K.; K bar). The Cu foil was held in place by a layer of ethanol underneath the foil and by sticky tape. The tape casts were dried on the tape caster platform for a short time before being transferred to an oven (Termaks). The tape casts were then dried at least overnight at 70°C, followed by at least 5 hours at 120 °C in a vacuum oven (Binder, VD 23).

Further in this appendix chapter, the procedure adjustments will be commented. If nothing else is stated, the procedure followed the instructions given in this section.

A.2 Silgrain® e-Si 400

Figure A.1 summarizes the adjustments made with respect to the preparation procedure described in section A.1 in order to achieve good Si electrodes with Silgrain® e-Si 400.

The first iteration of making Si electrodes with Silgrain® e-Si 400 was cast 020513, and the slurry was made using the procedure described in section A.1. The slurry was inhomogeneous upon visual inspection. A few clusters of wet powder materials were visible on the walls of the steel jar after mixing. The slurry was further mixed for another 15 minutes at 25 Hz. Still, a few clusters of wet powder materials were visible on the inner walls of the steel jar. These clusters were tried to be excluded in the further tape casting procedure. A spatula was needed to distribute the slurry onto the Cu foil due to the thickness of the slurry. The slurry was tape casted onto Cu foil using a meterbar with tread depth "4". After the cast had dried, three Si electrode discs were cut out from one side of the cast and weighed. They had a Si loading of 0.78 ± 0.02 mg/cm^2.

The second iteration at making Si electrodes with Silgrain® e-Si 400 was cast 030717. The

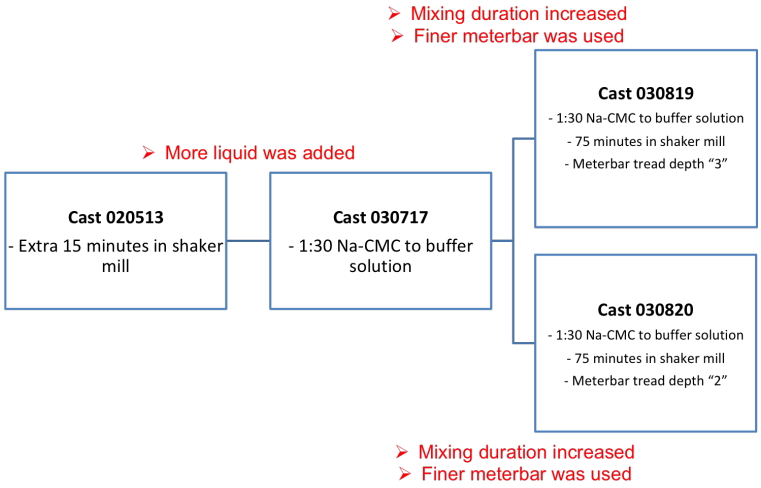

Figure A.1: Summarizes the adjustments made with respect to the preparation procedure for Silgrain® e-Si 400 electrodes described in section A.1. The first iteration is to the left, while the last iteration is to the right. Attempts tested simultaneously are placed above each other. The red text describes the adjustments made between each iteration.

total amount of liquid was increased in this iteration by adding excess buffer solution. The total weight ratio between Na-CMC and buffer solution then became 1:30. The slurry was thin enough to be poured onto the Cu foil. The slurry was tape casted onto Cu foil using a meterbar with tread depth "4". The Cu foil was folded by the meterbar at the start of the tape casting process. The tape casting was immediately stopped and the Cu foil was straightened out again before resuming the process. After the cast had dried, three Si electrode discs were cut out from one side of the cast and weighed. They had a Si loading of 0.52 ± 0.01 mg/cm^2.

The third iteration of making Si electrodes with Silgrain® e-Si 400 was cast 030819. In this iteration, the mixing duration was increased and a finer meterbar was used for tape casting. The total weight ratio between Na-CMC and buffer solution was 1:30. The steel jar was mixed in a shaker mill for 75 minutes instead of 60 minutes. The slurry was homogeneous upon visual inspection and thin enough to be poured onto the Cu foil. The slurry was tape casted onto Cu foil using a meterbar with tread depth "3" instead of "4". The cast dried unevenly, from one side to the other. After the cast had dried, three Si electrode discs were cut out from one side of the cast and weighed. They had a Si loading of 1.10 ± 0.08 mg/cm^2.

The fourth iteration of making Si electrodes with Silgrain® e-Si 400 was cast 030820. Both the third and fourth iterations were done simultaneously. In this iteration, an even finer

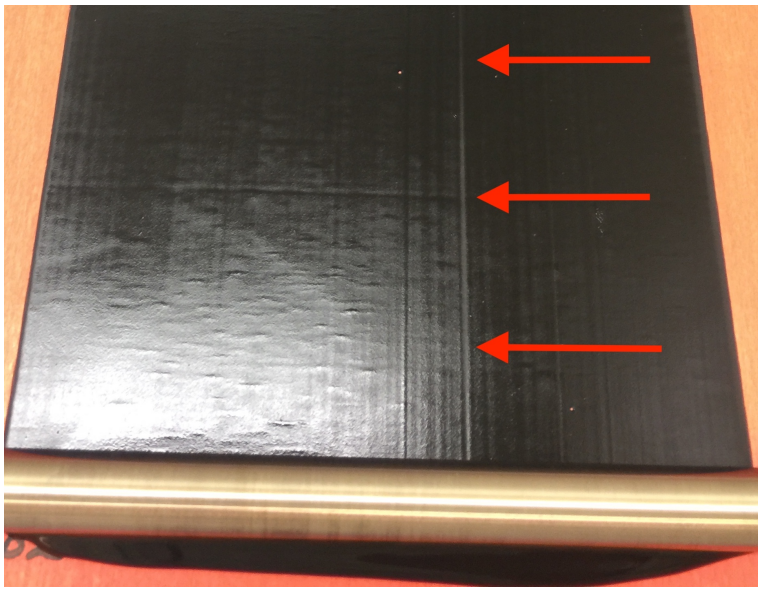

Figure A.2: Stripe in tape casted slurry of cast 030820. A fin meterbar with tread depth "2" was used in this tape casting process.

meterbar was used for tape casting. The total weight ratio between Na-CMC and buffer solution was 1:30. The steel jar was mixed in a shaker mill for 75 minutes. The slurry was homogeneous upon visual inspection and thin enough to be poured onto the Cu foil. The slurry was tape casted onto Cu foil using a meterbar with tread depth "2". The cast dried fast and evenly on the tape caster platform. A few stripes in the active material were visible after tape casting, as seen in figure A.2. After the cast had dried, three Si electrode discs were cut out from visually good areas on one side of the cast and weighed. They had a Si loading of 0.24 ± 0.01 mg/cm^2.

It was determined that visually homogenous and flat areas of cast 030717 would be used for electrochemical testing due to time restrictions.

A.3 99.5% Si Resitec

Figure A.3 summarizes the adjustments made with respect to the preparation procedure described in section A.1 in order to achieve good Si electrodes with 99.5% Si Resitec.

The first iteration of making Si electrodes with 99.5% Si Resitec was cast 020616. In the first attempt, the total weight ratio between Na-CMC and buffer solution was 1:32, instead of 1:23. The steel jar was mixed in a shaker mill for 75 minutes. The slurry was thin enough

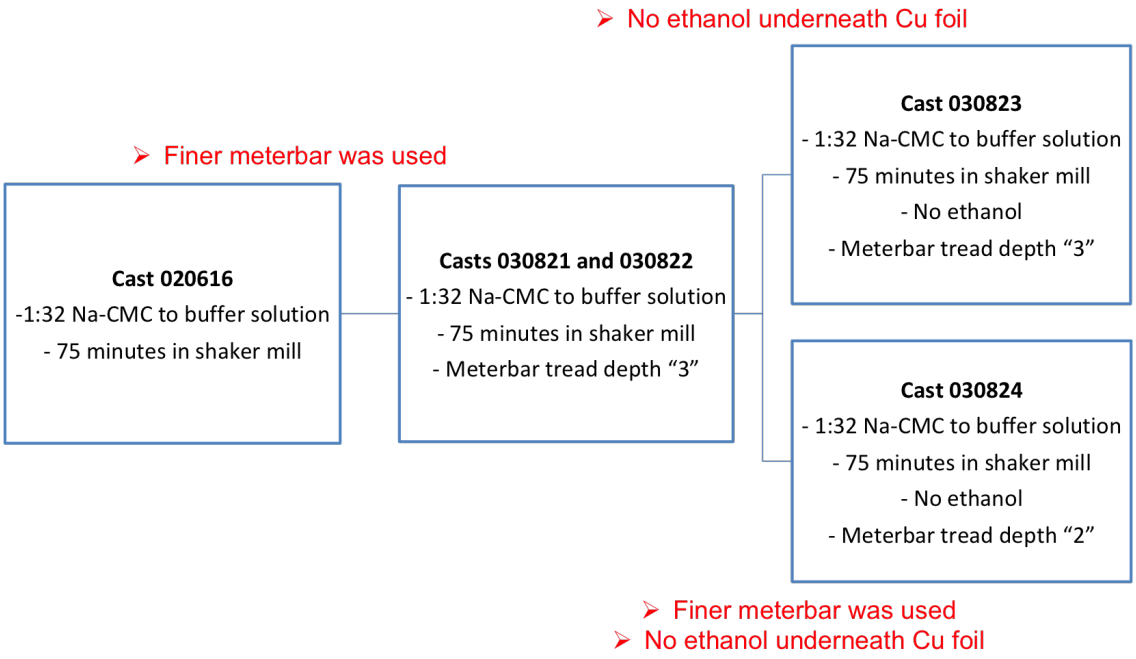

Figure A.3: Summarizes the adjustments made with respect to the preparation procedures for 99.5% Si Resitec electrodes described in section A.1. The first iteration is to the left, while the last iteration is to the right. Attempts tested simultaneously are placed above each other. The red text describes the adjustments made between each iteration.

to be poured onto the Cu foil. The slurry was tape casted onto Cu foil using a meterbar with tread depth "4". The meterbar ripped one of the edges of the Cu foil during tape casting. The cast dried unevenly on the tape casting platform. After the cast had dried, one side of the cast was brittle, and pieces of powder broke off. This can be seen in figure A.4. Three Si electrode discs from the visually good side of the cast were cut out and weighed. They had a Si loading of 0.97 ± 0.10 mg/cm^2.

The first attempt at the second iteration of making Si electrodes with 99.5% Si Resitec was cast 030821. In this iteration, a finer meterbar was used for tape casting. The total weight ratio between Na-CMC and buffer solution was 1:32. The steel jar was mixed in a shaker mill for 75 minutes. The slurry was thin enough to be poured onto the Cu foil. The slurry seemed to have a homogeneous texture, but with visual grey streamlines. The slurry was tape casted onto Cu foil using a meterbar with tread depth "3". After tape casting, clear clusters were visible in the slurry. The meterbar had also ripped a small hole in the Cu foil during tape casting. After the cast had dried, three Si electrode discs from a visually good

Figure A.4: Brittle part of cast 020616. The dried powder material flaked off.

section of the cast were cut out and weighed. They had a Si loading of 1.43 ± 0.04 mg/cm^2.

The second attempt at the second iteration of making Si electrodes with 99.5% Si Resitec was cast 030822. Both attempts used the same mixing procedures and tape casting setup. A wave in the Cu foil was visible in front of the meterbar during the tape casting. The slurry had been distributed unevenly, and there were clear height differences in the tape casted slurry, which could be seen by light reflections in the wet slurry. Figure A.5 shows cast 030822 while drying on the tape casting platform. This cast was not examined further.

The third iteration of making Si electrodes with 99.5% Si Resitec was cast 030823. This iteration also had the same setup as the second iteration, except for that the Cu foil was only held in place by sticky tape, and no ethanol was used underneath. The dendritic Cu foil was not completely flat on the tape casting platform, but rather had a wavy surface. The slurry was thin enough to be poured onto the Cu foil. The slurry was tape casted onto Cu foil using a meterbar with tread depth "3". There was a visible stripe in the slurry after tape casting, but the slurry dried evenly. After the cast had dried, three Si electrode discs were cut out from visually good areas of the cast and weighed. They had a Si loading of 0.35 ± 0.01 mg/cm^2.

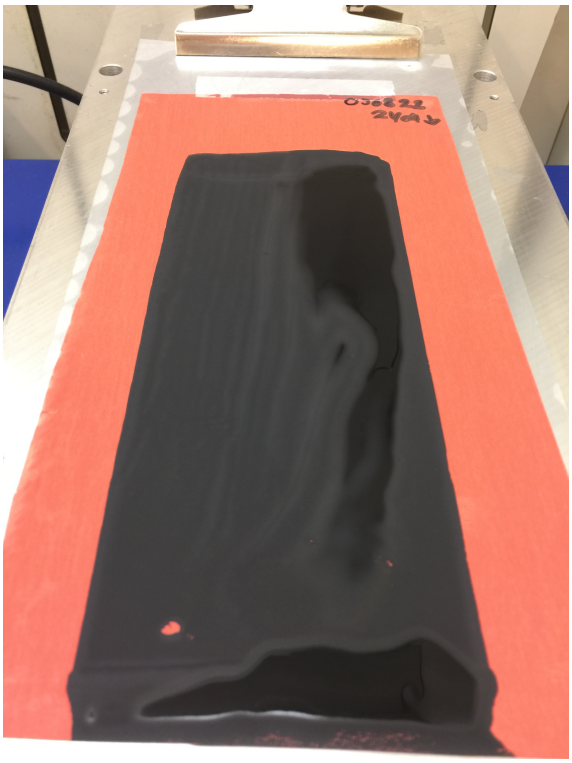

Figure A.5: Uneven drying of cast 030822.

The fourth iteration of making Si electrodes with 99.5% Si Resitec was cast 030824. Both the third and fourth iterations were tested simultaneously. In this iteration, a finer meterbar was used for tape casting. The total weight ratio between Na-CMC and buffer solution was 1:32. The steel jar was mixed in a shaker mill set to 25 Hz for 75 minutes. The slurry was thin enough to be poured onto the Cu foil. The dendritic Cu foil was held in place just by sticky tape, and no ethanol was used. The dendritic foil was not completely flat on the tape caster platform, but rather had a wavy surface. The slurry was tape casted onto Cu foil using a meterbar with tread depth "2". There was a visible stripe in the slurry after tape casting, but the slurry dried evenly. After the cast had dried, three Si electrode discs were cut out from visually good areas of the cast and weighed. They had a Si loading of 0.23 ± 0.04 mg/cm^2.

It was determined that visually homogenous and flat areas of cast 030823 would be used for electrochemical testing due to time restrictions.

A.4 Experiences from the Procedure Developement

Several tread depths were tried when developing of the preparation procedures. The main reason was to alter the Si loading without adding more buffer solution, containing $C_6H_8O_7$ and KOH, to the electrodes. The ability of doing this was, on the other hand, limited because there were only three meterbars with applicable tread depths. The meterbar with the finest tread depth gave stripes in the electrode sheets, as seen in figure A.2.

Tape casting onto a flat piece of Cu foil turned out to be important. The Cu foil was not completely flat but had shallow waves. It was difficult to straighten the foil by hand without ruining the dendritic surface. In a few of the trials with ethanol underneath the foil, waves occurred in the foil in front of the meterbar. The ethanol seemed to hinder the foil from straightening itself. Trials without ethanol underneath the foil were therefore tried and seemed to allow the foil to straight out with less resistance.

It should be mentioned that the mixing sequence and batch size for slurries with Sigma-Aldrich nano-Si were different compared to the sequence used for Silgrain® e-Si 400 and 99.5% Si Resitec. In the mixing procedure for Sigma-Aldrich nano-Si, the excess buffer solution and Si powder were mixed first. This was thought to be better with respect to soaking the Si particles in liquid because the binder solution was more viscous than the buffer solution. The slurry batches for slurries with Sigma-Aldrich nano-Si were sized up to triple portion compared to Silgrain® e-Si 400 and 99.5% Si Resitec in order to achieve proper mixing with the Ultra Turrax. The mixing was ineffective using too small portions.

Appendix B

XRD Results of Silicon Powders as Received

The tables below contain information about the intensity peaks of the Si powders obtained through XRD analysis in this project.

Table B.1: Table of the intensity peaks in the diffraction pattern of the Silgrain® e-Si 400 as received. The table shows the diffraction angle and intensity value of the peaks. $K_{\alpha 2}$ has been stripped, but the background has not been subtracted. The background intensity is approximately 225.

2θ [°]	Intensity
28.4471	490.4533
47.3057	357.6286
56.1241	289.5078
69.1689	237.2682

Table B.2: Table of the intensity peaks in the diffraction pattern of the Sigma-Aldrich nano-Si as received. The table shows the diffraction angle and intensity value of the peaks. $K_{\alpha 2}$ has been stripped, but the background has not been subtracted. The background intensity is approximately 75.

2θ [°]	Intensity
28.4996	169.5575
47.3741	119.967
56.1885	99.0808
69.1689	76.6547

Table B.3: Table of the intensity peaks in the diffraction pattern of the 99.5% Si Resitec as received. The table shows the diffraction angle and intensity value of the peaks. $K_{\alpha 2}$ has been stripped, but the background has not been subtracted. The background intensity is approximately 150.

2θ [°]	Intensity
28.4728	445.828
47.3339	296.9075
56.1483	219.9626
69.1421	162.0262

Table B.4: Table of the intensity peaks in the diffraction pattern of the Si kerf as received. The table shows the diffraction angle and intensity value of the peaks. $K_{\alpha 2}$ has been stripped, but the background has not been subtracted. The background intensity is approximately 1.

2θ [°]	Intensity
28.4594	95.0307
34.1124	11.6769
35.6261	25.301
38.1579	8.7457
41.413	3.411
47.3339	42.1809
56.1349	20.7381
60.0197	9.6934
65.6191	3.1266
69.1287	4.6788
71.7677	5.8264

Appendix C

Diffraction Patterns of Silicon and Silicon Carbide

The tables below contain information about the intensity peaks in the diffraction patterns of Si and SiC. This information has been gathered from the PDF-4+2016 RDB database from the International Centre for Diffraction Data (ICDD) [54].

Table C.1: Table of the intensity peaks in diffraction pattern of silicon (Si) for diffraction angles 0-80°. Values retrieved from [54].

2θ [°]	hkl	Intensity
28.452795	111	7336
47.320737	220	4296
56.144038	311	2328
58.879283	222	7
69.158240	400	543
76.408331	331	756

It should be noted that the structure factor of Si (equation 2.19) predicts 222 to not show because it falls into the category ${F_{hkl}}^2 = 0$ for $h + k + l = 2 * \text{odd number}$. The 222 intensity peak is 0.1% of the most intense peak 111 according to the intensity values in table C.1.

Table C.2: Table of the intensity peaks in diffraction pattern of silicon carbide (SiC) for diffraction angles 0-80°. Values retrieved from [54].

2θ [°]	hkl	Intensity
34.182573	101	2934
35.729331	102	7336
38.235177	103	1467
41.503945	104	734
60.154913	110	2568
65.807452	109	1100
71.968923	116	116
73.594922	203	1100
75.656292	0012	514

Appendix D

BET Plots of the Silicon Powders

This section contains the results from the BET plots of Silgrain® e-Si 400, Sigma-Aldrich nano-Si, 99.5% Si Resitec and Si kerf obtained from the BET analysis.

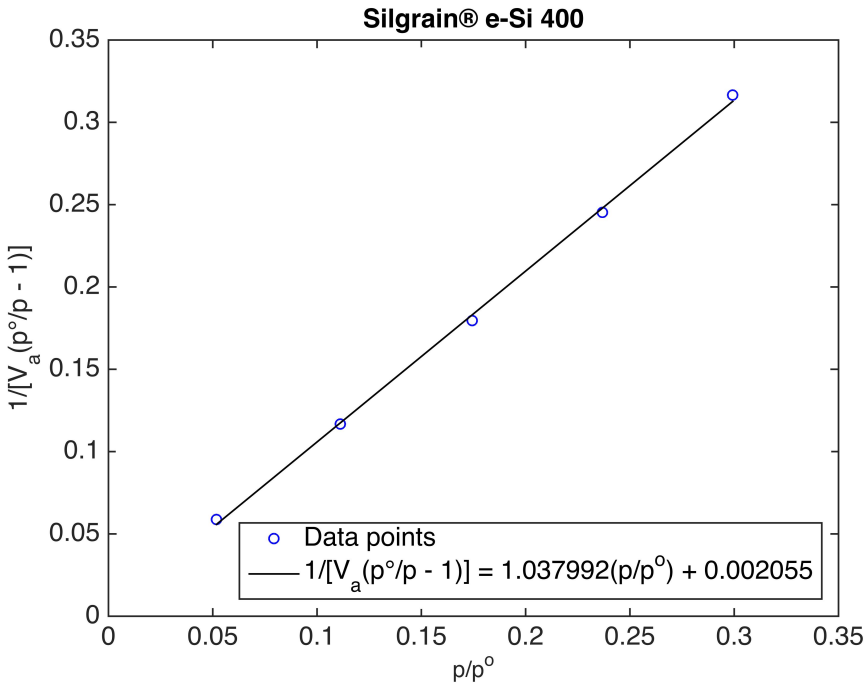

Figure D.1: BET plot of the Silgrain® e-Si 400 powder. The BET surface area is 4.1856 ± 0.0802 m^2/g and the correlation coefficient is 0.9994684.

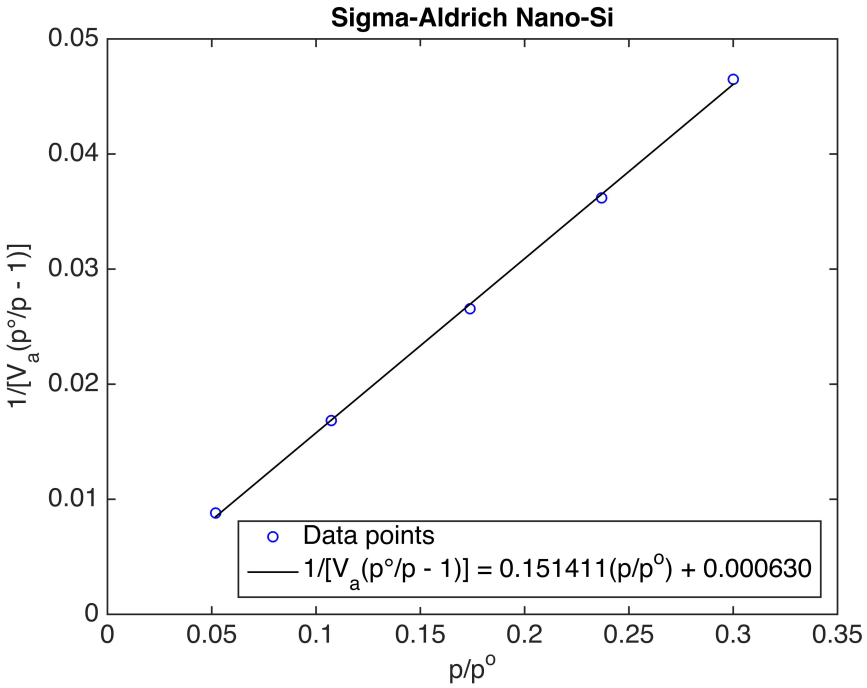

Figure D.2: BET plot of the Sigma-Aldrich nano-Si powder. The BET surface area is 28.6317 ± 0.4169 m^2/g and the correlation coefficient is 0.9996912.

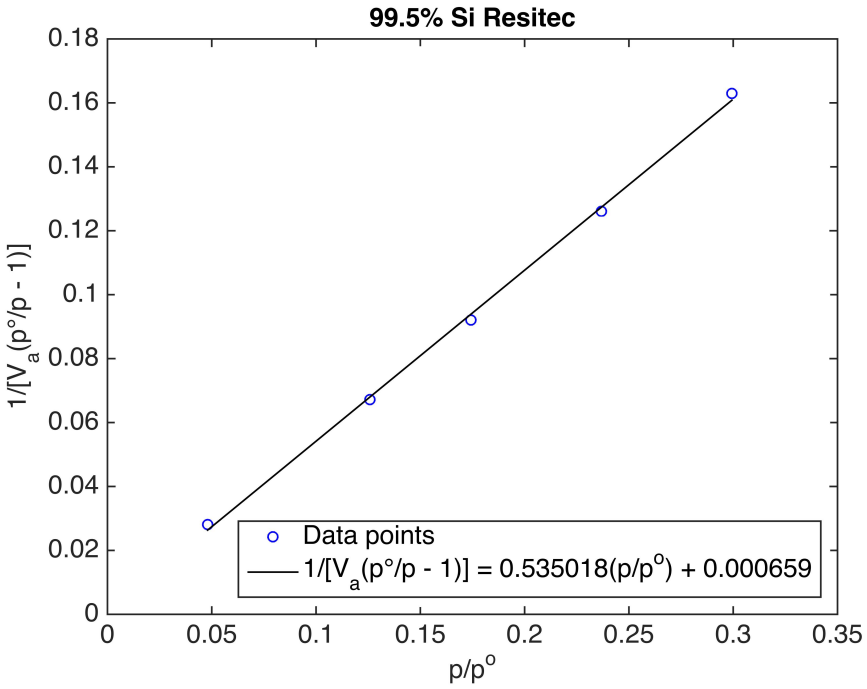

Figure D.3: BET plot of the 99.5% Si Resitec powder. The BET surface area is 8.1265 ± 0.1663 m^2/g and the correlation coefficient is 0.9993946.

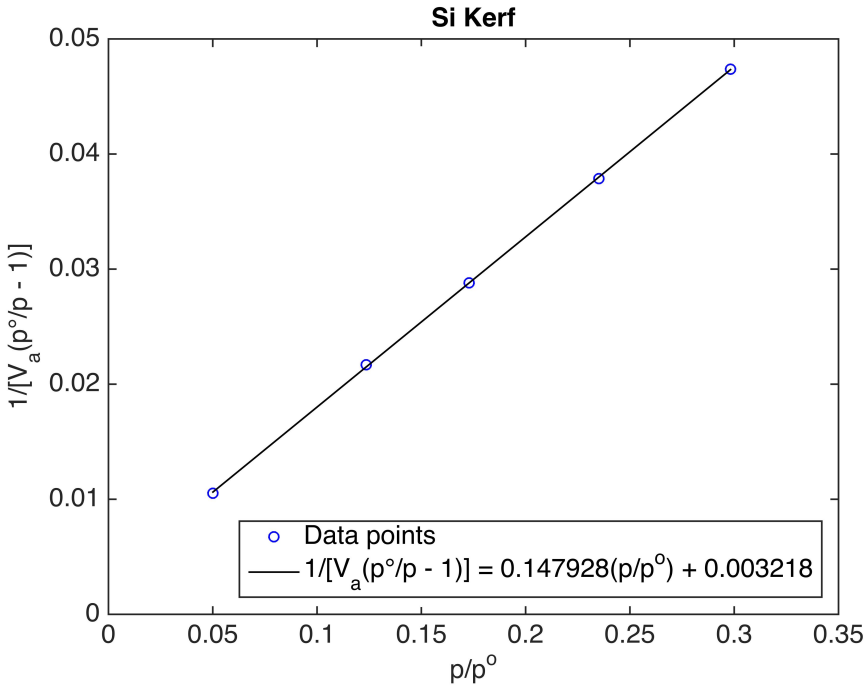

Figure D.4: BET plot of the Si kerf powder. The BET surface area is 28.8013 ± 0.1639 m^2/g and the correlation coefficient is 0.9999512.